Draft version August 14, 2021
Typeset using LaTeX **preprint** style in AASTeX61

THE STRUCTURE OF LARGE-SCALE STELLAR DISKS IN CLUSTER LENTICULAR GALAXIES.[a]

Olga K. Sil'chenko,[1,2] Alexei Yu. Kniazev,[3,4,1] and Ekaterina M. Chudakova[1]

[1] *Sternberg Astronomical Institute, M.V. Lomonosov Moscow State University, Universitetsky pr., 13, Moscow, 119991 Russia*
[2] *Isaac Newton Institute, Chile, Moscow Branch*
[3] *South African Astronomical Observatory, PO Box 9, 7935 Observatory, Cape Town, South Africa*
[4] *Southern African Large Telescope Foundation, PO Box 9, 7935 Observatory, Cape Town, South Africa*

Submitted to AJ

ABSTRACT

By obtaining imaging data in two photometric bands for 60 lenticular galaxies – members of 8 southern clusters – with the Las Cumbres Observatory one-meter telescope network, we have analyzed the structure of their large-scale stellar disks. The parameters of radial surface-brightness profiles have been determined (including also disk thickness), and all the galaxies have been classified into pure exponential (Type I) disk surface-brightness profiles, truncated (Type II) and antitruncated (Type III) piecewise exponential disk surface-brightness profiles. We confirm the previous results of some other authors that the proportion of surface-brightness profile types is very different in environments of different density: in the clusters the Type-II profiles are almost absent while according to the literature data, in the field they constitute about one quarter of all lenticular galaxies. The Type-III profiles are equally presented in the clusters and in the field, while following similar scaling relations; but by undertaking an additional structural analysis including the disk thickness determination we note that some Type-III disks may be a combination of a rather thick exponential pseudobulge and an outer Type-I disk. Marginally we detect a shift of the scaling relation toward higher central surface brightnesses for the outer segments of Type-III disks and smaller thickness of the Type-I disks in the clusters. Both effects may be explained by enhanced radial stellar migration during disk galaxy infall into a cluster that in particular represents an additional channel for Type-I disk shaping in dense environments.

Corresponding author: Olga Sil'chenko
olga@sai.msu.su,olgasil.astro@gmail.com
olga@sai.msu.su
akniazev@saao.ac.za
artenik@gmail.com

Keywords: galaxies: elliptical and lenticular - galaxies: evolution - galaxies: formation - galaxies: structure.

1. INTRODUCTION

The origin of S0 galaxies – which is the second, after spirals, most frequent morphological type in the nearby Universe constituting about 15% of all galaxies (Naim et al. 1995; Baillard et al. 2011; Buta et al. 2015) – remains unclear and controversial. Their global structure – a presence of two main large-scale components, a bulge and a disk, with various contribution of each into the total luminosity, – resembles the structure of early-type spirals very much; however, their disks lack spiral arms, and low-level star formation in S0s, if present, is usually organized in ring-like structures. The resemblance of the lenticular and spiral scaling relations (see e.g. Laurikainen et al. 2010; Eliche-Moral et al. 2015) and the absence of intense star formation in the formers provoke numerous scenaria of S0 (trans-)formation from spirals by removing the gas from the disks and by quenching star formation in the disks. The dominance of S0 population in clusters at $z = 0$ (Dressler 1980; Fasano et al. 2015) implies dynamical mechanisms related to dense environments and massive host dark-matter halos as probable ways to transform a spiral galaxy into a lenticular one. However, despite the dominance of S0s in clusters, the majority of them inhabit loose groups and even very rarified fields being completely isolated (Katkov, Kniazev, and Sil'chenko 2015); their origin cannot be related to ram-pressure gas removal from spiral disks or tidal disk transformation in dense environments. There are some evidences that S0s in clusters and in the field may have different channels to form (e.g. Wilman & Erwin 2012). If it is true, and the dynamical mechanisms shaping large-scale stellar disks of S0s in clusters and S0s in the field are different, one can expect the quiescent stellar disks of nearby S0s to have different structure characteristics in environments of different density. When referring to the 'structure characteristics', we mean both radial structure and vertical structure of the disks.

As for the radial structure of galactic stellar disks, it is now well known that the shape of stellar surface-brightness (density) profiles in disk galaxies is piecewise exponential. They can be fitted by a single-scale exponential law up to the border of a stellar disk (Freeman 1970), or by an exponential law with truncation at some radius as the Type II disks in Freeman (1970) or disks with breaks noted by Van der Kruit & Searle (1981), or by two exponential profiles suitable within different radius ranges, with the outer exponential law having a larger scalelength – so called antitruncated disks (Sil'chenko, Burenkov, and Vlasyuk 1998; Sil'chenko et al. 2003; Erwin, Beckman, and Pohlen 2005). Presently, after Pohlen & Trujillo (2006), these three types of surface-brightness profiles are numbered as follows: pure exponential disks are Type I, truncated disks are Type II, and antitruncated disks are Type III. It is not clear yet, if the shape of a stellar surface-brightness (density) profile is an initial condition of the disk formation, or there are some ways of dynamical transition between the types. Recently Erwin, Gutiérrez, and Beckman (2012) and Pranger et al. (2017) have reported a discovery of environment effect on the profile-shape statistics for disk galaxies: in clusters there is a deficit of Type II profiles and an excess of Type I profiles. Consequently, Clarke et al. (2017) have proposed a dynamical mechanism to transform truncated disks into pure exponential ones when entering into cluster environment: a combination of gas stripping by ram pressure and of enhanced stellar radial migration in the disks provides necessary changes in the stellar disk structure. Earlier, there were also works with some dynamical simulations transforming pure exponential disks into antitruncated ones (e.g. Younger et al. 2007; Borlaff et al. 2014). Cosmological simulations reveal advanced dynamical evolution just of the Type-III disks: they suffer strong radial migration as well as concentration of newly accreted stars in the outermost parts (Ruiz-Lara et al. 2017). However, here we must note that not all observational studies of the disk-type proportion dependence on the environment density

find any difference between clusters and field for S0s: for example, in the STAGES survey results (Maltby et al. 2015) the absence of the Type-II disks in S0 galaxies has been claimed both for the cluster and for the field. So probably the question remains open.

Another important property of the galactic stellar disks is their thickness. It is crucial to have statistics on the thickness of S0 disks because it would allow to restrict strongly a choice of dynamical mechanisms shaping the large-scale components of lenticular galaxies. For example, dry minor mergers which have been proposed by Younger et al. (2007) to form an antitruncated surface-density profile, would thicken stellar disks strongly by increasing their stellar velocity dispersion (Walker, Mihos, and Hernquist 1996). Observational data on the galactic disk thicknesses were rather sparse; and up to now individual estimates of stellar disk thickness were made directly only for galaxies seen edge-on (e.g. Mosenkov, Sotnikova, and Reshetnikov 2010). Though some interesting statistics has been derived from these decompositions – for example, Mosenkov et al. (2015) have reported very weak dependence of the disk thickness on the morphological type, large scatter of the disk thicknesses in intermediate-type spirals, thicker disks in barred galaxies etc. – however, on our opinion, it is rather difficult to discuss radial and especially azimuthal structure of the galaxies seen strictly edge-on. Chudakova & Sil'chenko (2014) have proposed recently a quite novel method allowing to estimate the thickness of an exponential (or piecewise exponential) stellar disk seen under arbitrary inclination, if only it is not strictly edge-on or strictly face-on (with our method we explore the disk inclinations between 10° and 75°). We have already begun to study galactic disk thicknesses and to compare the statistics of disk thickness among the samples with various types of radial surface-brightness profiles for early-type disk galaxies in the field (Chudakova & Sil'chenko 2014; Sil'chenko, Kniazev, and Chudakova 2016). In the present paper we continue to apply our method of measuring thicknesses of individual galactic disks to a sample of S0 galaxies which are members of several southern clusters of galaxies. In Section 2 we describe the sample, in Section 3 we give details of our approach to the stellar disk structure characterization, in Section 4 we present our quantitative results, in Section 5 we discuss the consequences of our findings, and in Section 6 we conclude.

2. THE SAMPLE

For our photometric study we have selected 60 S0 galaxies in several southern clusters of galaxies, spanning a range of masses (X-ray luminosities) but all being not too far from us. The southern sky offers a rich choice of nearby clusters of galaxies, unlike the northern sky where only the Virgo cluster is closer to us than 70 Mpc. The list of clusters considered here is presented in the Table 1.

It is in the clusters listed in the Table 1 that we have selected galaxies classified as S0 or S0/a in the NASA/IPAC Extragalactic Database (NED). Some of the galaxies which we have taken to study are assigned the classification type of E or E+ in the NED; but our visual inspection of their images has revealed clear disk signatures – such as bars or blue rings, and we have recognized them as S0s. After deriving the surface brightness profiles (by the method described in the next Section) we have additionally checked the presence of large-scale stellar disks in the galaxies selected for the analysis – since the only distinctive attribute (definition) of the S0 morphological type is the presence of a large-scale disk without spiral arms. We have fitted the outer parts of the surface-brightness profiles by an exponential law and have assured that there exists at least one segment of the profile which lacks any systematic deviations from the exponential law within two exponential scalelengths. Just this criterion – the exponential law validity within two-scalelength radial range – was proposed by

Table 1. Clusters which host the studied S0s

The cluster name	D[1], Mpc	Scale[1], kpc per $''$	L_X[2], in 10^{44} erg/s	Number of S0s studied here
Abell 194	71	0.331	0.070	8
NGC 1550 group	49.6	0.238	0.153	4
Fornax	18.2	0.088	0.012	3
Centaurus	37.5	0.212	0.721	11
Hydra	54	0.272	0.297	13
Antlia	35	0.205	0.034	8
Abell 3565	55	0.262	0.008	4
Abell S0805	61	0.292	0.029	9

[1]NASA/IPAC Extragalactic Database

[2]Panagoulia, Fabian, and Sanders (2014)

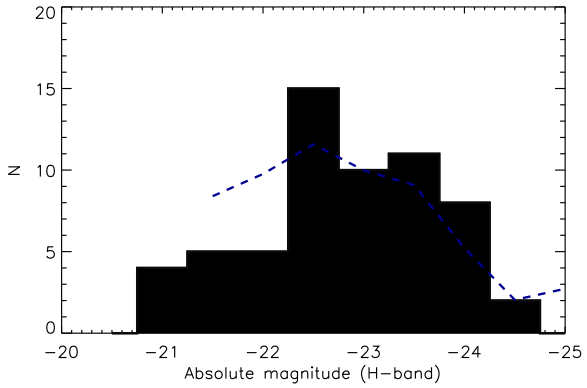

Figure 1. The distribution of the galaxy absolute magnitudes in the H-band for our sample; the M_H are taken from NED. The dashed line overposed represents the luminosity function of the volume-limited sample of early-type galaxies from Cappellari et al. (2011).

Freeman (1970) in his classical work as a feature of exponential stellar disks. The range of luminosities of the S0s selected for our study is from $M_H = -21$ to $M_H = -24.5$ – in any case, our galaxies are not dwarfs. Moreover, if one compare the distribution of the NIR absolute magnitudes of our galaxies (Fig. 1) with the luminosity function of the volume-limited sample of nearby early-type galaxies from Cappellari et al. (2011), one can see that we have a well-presented sample at $L \geq L_*$ and an underpresented sample at lower luminosities. However, we have covered all the luminosity range of non-dwarf S0 galaxies. The galaxies are selected to be not strictly edge-on; curiously, in some clusters (e.g. in Abell 194 or in Abell S0805) there is unexpectedly large fraction of edge-on S0s, and our choice has not been easy. In general, the sample is not full, but rather representative; for example, in the Antlia cluster, among 25 S0s brighter than $m_b = 15.7$ (Ferguson & Sandage 1990) we have taken 8 galaxies for our photometric study.

3. OBSERVATIONS AND DATA ANALYSIS

The observations have been fulfiled by the Las Cumbres Observatory (LCO) robotic telescope network (Brown et al. 2013) between May 2015 and February 2016. Currently, the LCO consists of two 2-m optical telescopes, of ten 1-m telescopes, of eight 40-cm telescopes, and one 83-cm telescope located at six observatories, three in the Northern and three in the Southern hemisphere. Such distribution of telescopes makes it possible to carry out photometric and spectral observations of objects regardless of their declinations, create continuous time series of observations, operatively acquire spectra of recently discovered supernovae, and much more (Brown et al. 2013). All our observations were done with LCO meter-class telescopes with standard Sinistro cameras for the acquisition of direct frames. This camera consists of a 4000×4000 CCD. With the physical pixel size of this CCD, 15μm, and standard 1×1 binning, the angular size of each pixel is 0.389 arcsec, and each frame covers an area 26.5×26.5 arcmin in size. Each Sinistro camera can obtain images in 21 different bandpasses, of which we used the g and r filters of the Sloan survey photometric system. Our observations have been made mostly in Cerro Tololo with standard exposures of 900s × 2 in g and 600s × 2 in r. The seeing quality estimates made over the primarily reduced images ranged from 1.2 arcsec to 2.5 arcsec: due to the robotic regime of the observations, the focussing and guiding were not always good. During the observations, photometric standard stars were not exposed, so we calibrated our images by using the HyperLEDA[1] aperture photometry collections: the Johnson-Cousins BVR aperture data for every galaxy, mostly based on the compilations of the photometric survey of the southern sky (Lauberts & Valentijn 1989), were transformed into the gr-system with the interrelations found by Jordi, Grebel, and Ammon (2006). The cluster Abell 194 is in the zone covered by the SDSS survey while the aperture photometric data are absent in the HyperLEDA for the galaxies – members of this cluster; so for the members of Abell 194 we have used the gr-photometry of nearby stars from the SDSS/DR9 public data archive as standards. Also we have used gr-photometry of stars from the Pan-STARRS1 public data archive as standards for the galaxies in the NGC 1550 group and for the field of NGC 3307 (the Hydra cluster) since they lack aperture photometry in the HyperLEDA database too. Figure 2 shows comparison of the azimuthally averaged surface-brightness profiles in the r-band calculated for UGC 1030 and UGC 1043 by exploring our data and by exploring the calibrated SDSS/DR9 frames. One can see that in general the agreement is good. In the very center the SDSS profiles rise sharper than ours because of the better spatial resolution. At the edges of the disks the SDSS profiles go slightly above the LCO profiles, while the latters continue the exponential shape of the disks till fainter surface brightnesses. The cause of this discrepance is not clear; perhaps we deal with a different level of scattered light in the SDSS and LCO images.

The primary reduction provided by the LCO pipeline included bias subtraction and flatfielding of individual frames. We then extracted smaller pieces of images including the galaxies selected, co-added two g-band images and two r-band images proceeding cosmic hit cleaning, and subtracted the sky background from the combined g- and r-images. The sky background levels were estimated over large, by 51 × 51 pixels, empty square areas, beyond the galaxies, in several, from 4 to 8, directions from the galaxy centers. These estimates were averaged before subtraction, or, in the cases of noticeable sky background gradients, interpolated linearly onto the galaxy position.

[1] http://leda.univ-lyon1.fr

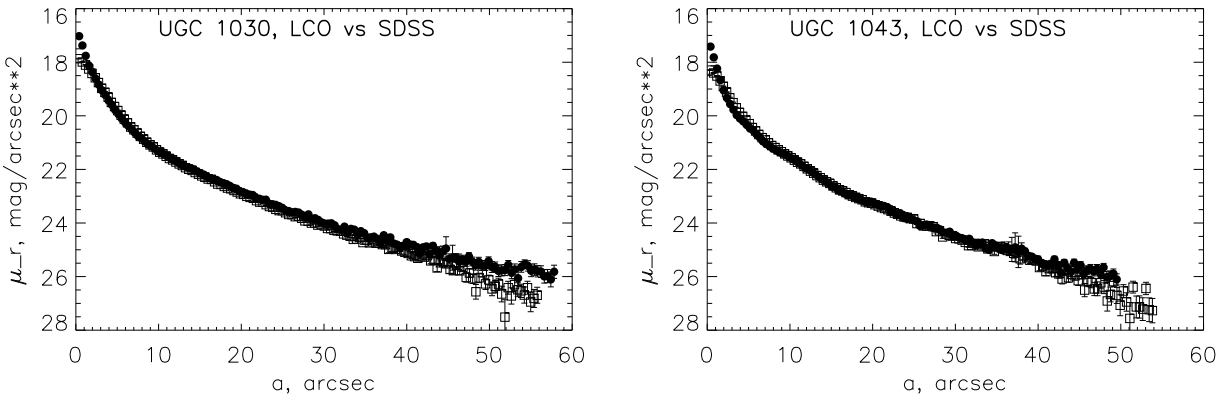

Figure 2. The comparison of the azimuthally averaged surface brightness profiles calculated from the SDSS/DR9 r-images (black points) and from the LCO r-images (open squares) for the Abell 194 members UGC 1030 and UGC 1043.

With flat-fielded and sky-subtracted images in hands, we have undertaken isophotal analysis for every galaxy and have derived radial variations of the isophote ellipticities and major-axis position angle. By assuming that large-scale stellar disks of our S0 galaxies are flat and have no warps, for every galaxy we have found a radius where the isophote ellipticity stops to rise; we then suggest that the flat disks dominate in the total surface brightness of the outer regions of the galaxies, starting from these radii outward. To calculate the azimuthally averaged surface-brightness profiles of the disks, we fixed the shape of the ellipses characterizing the round disk projection onto the sky plane, by taking the isophote ellipticity and major-axis position angle just at these radii, and by moving outward we averaged the surface brightnesses in the elliptical rings at every value of the radius. So the azimuthally averaged surface-brightness profiles of the disks have been derived. Then we fitted these disk surface-brightness profiles by an exponential law starting from the outermost point exceeding the sky level by an rms sky-level scatter value. The quality of the fit was recognized to be good if the rms scatter of the points around the fitting line was within typical errors of the individual points. If we find an inner radius where the azimuthally averaged surface-brightness profile starts to deviate systematically up or down from the fitted exponential law and if this radius is still within the disk-dominated radial range, we concluded that the profile is not of the Type I, and fitted another exponential segment into the inner part of the disk azimuthally averaged surface-brightness profile. As a result of this procedure, we have divided the total sample into three subsamples: the S0s with Type-I profiles, the S0s with Type-II profiles, and the S0s with Type-III profiles. Figures 3, 4, and 5 demonstrate typical examples of all three types of the disk surface-brightness profiles.

The relative disk thicknesses have been calculated by our original method described in details by Chudakova & Sil'chenko (2014); the careful testing of the method and determining the boundaries of its application will be presented later by Chudakova & Katkov (2019). Briefly, we followed the consideration of the projection effects on an ellipsoid with the axes $a_1 = a_2 > a_3$ made by Hubble (1926). If we observe an intrinsically round, infinitely thin disk projected onto the sky plane under the inclination i, we see an ellipse with the axis ratio of $b/a = \cos i$. If the disk is not infinitely thin and can be imagined as an oblate ellisoid with the vertical-to-radial axis ratio of q, then $\cos^2 i = \frac{(b/a)^2 - q^2}{1-q^2}$. The latter equation allows us to calculate the relative thickness q, if we have the possibility to determine independently the inclination i and the isophote axis ratio b/a. The latter parameter is provided by the isophote analysis. The former parameter can be obtained directly from the 2D surface photometry

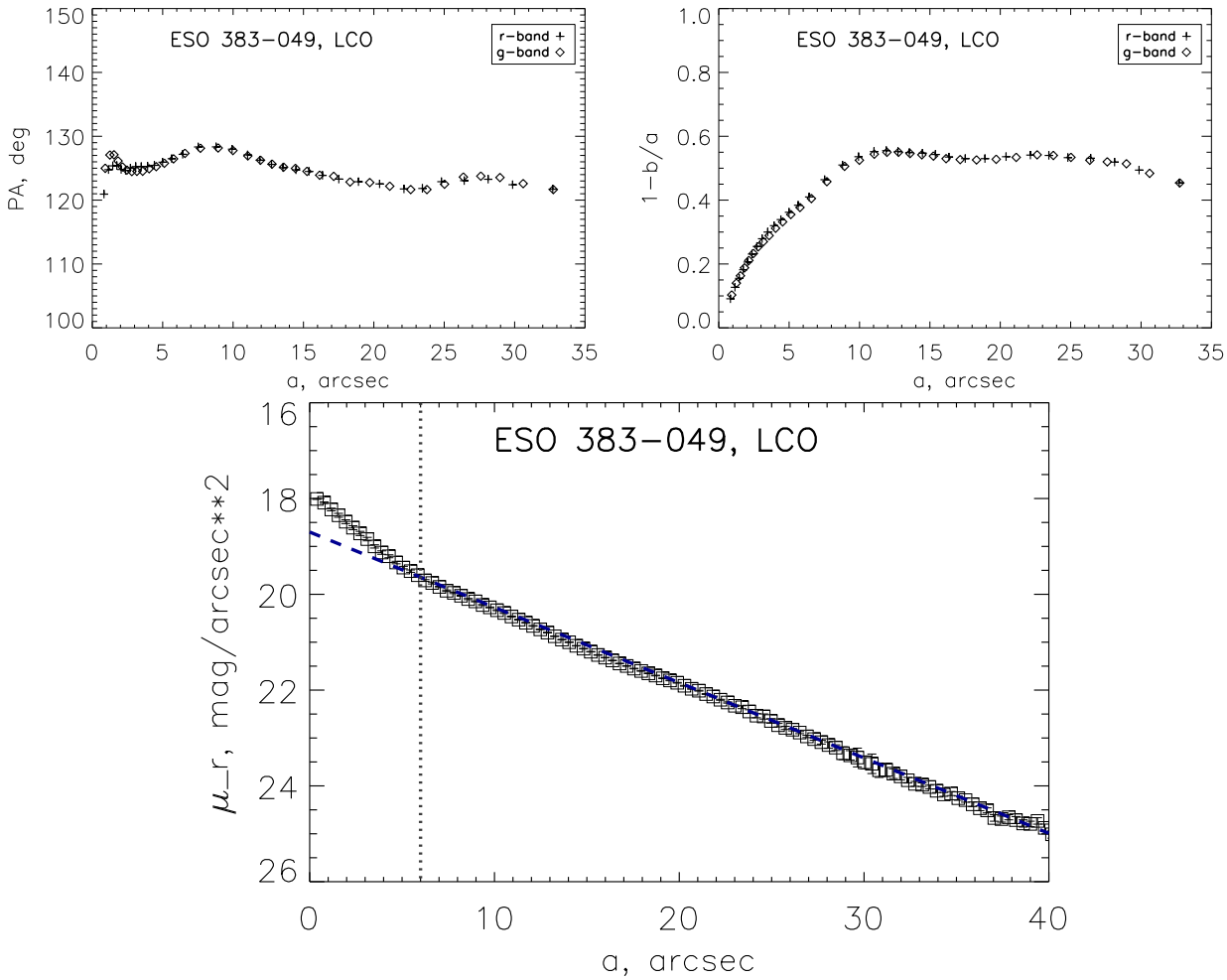

Figure 3. An example of a single-scale exponential surface-brightness profile (Type I): ESO 383-049. The isophote ellipticity stops to rise at $\sim 10''$, and from this radius to the optical border of the galaxy at $35''$ the surface-brightness profile is well fitted by an exponential law with unique scalelength. We show the boundary between the bulge and the disk by a vertical dotted line.

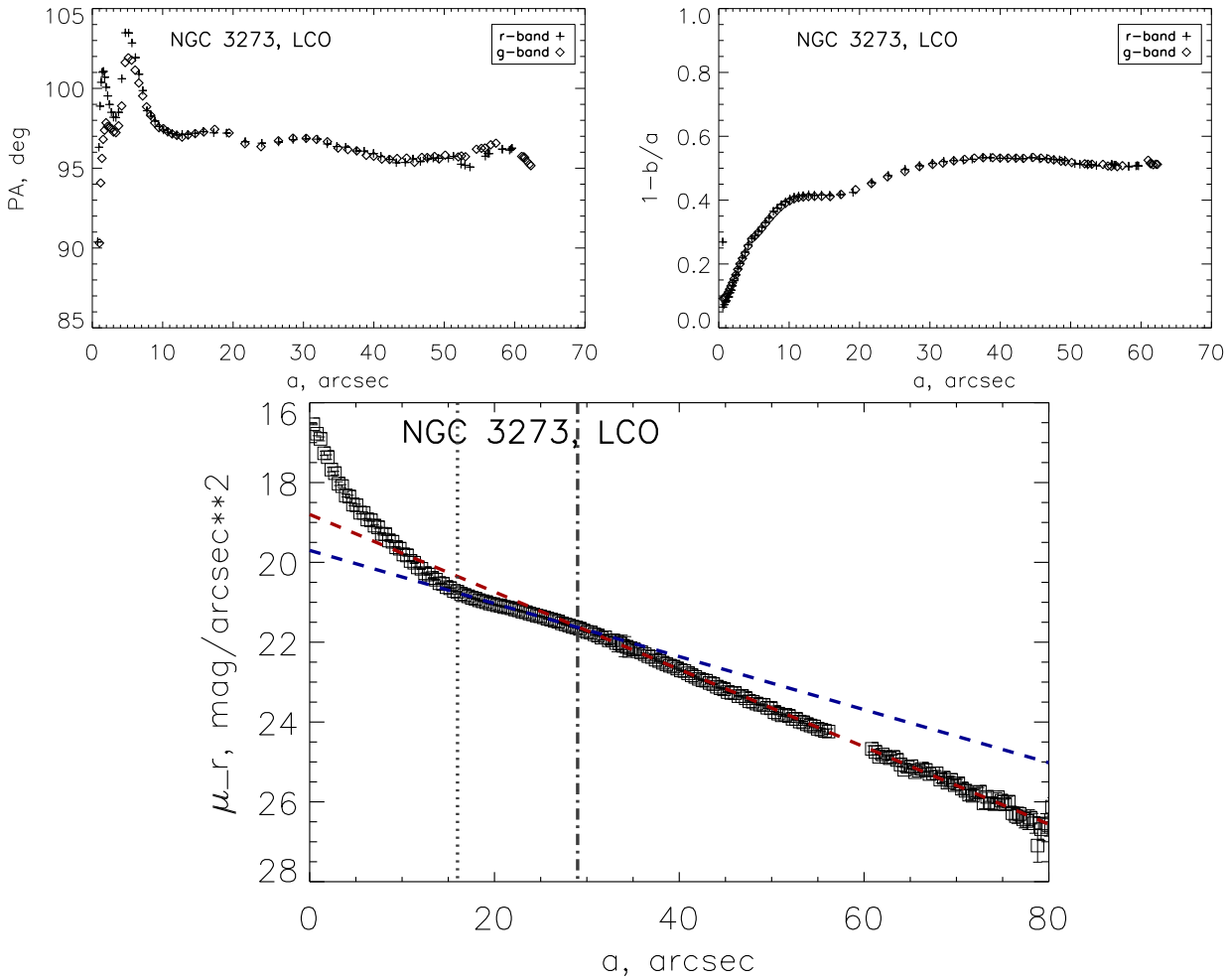

Figure 4. An example of a truncated exponential surface-brightness profile (Type II): NGC 3273. In the central part of the galaxy there is a rather shallow segment of the surface-brightness profile – a so called lens. The isophote ellipticity profile has two plateau: in the range of $10'' - 20''$ at the level of 0.4 and at $R > 30''$ – at the level of 0.5. The outer exponential law being extrapolated to the center goes above the lens surface-brightness profile – a certain signature of the truncated surface-brightness profile. We show the boundary between the bulge and the disk by a vertical dotted line; another vertical, dashed-dotted line marks the break radius.

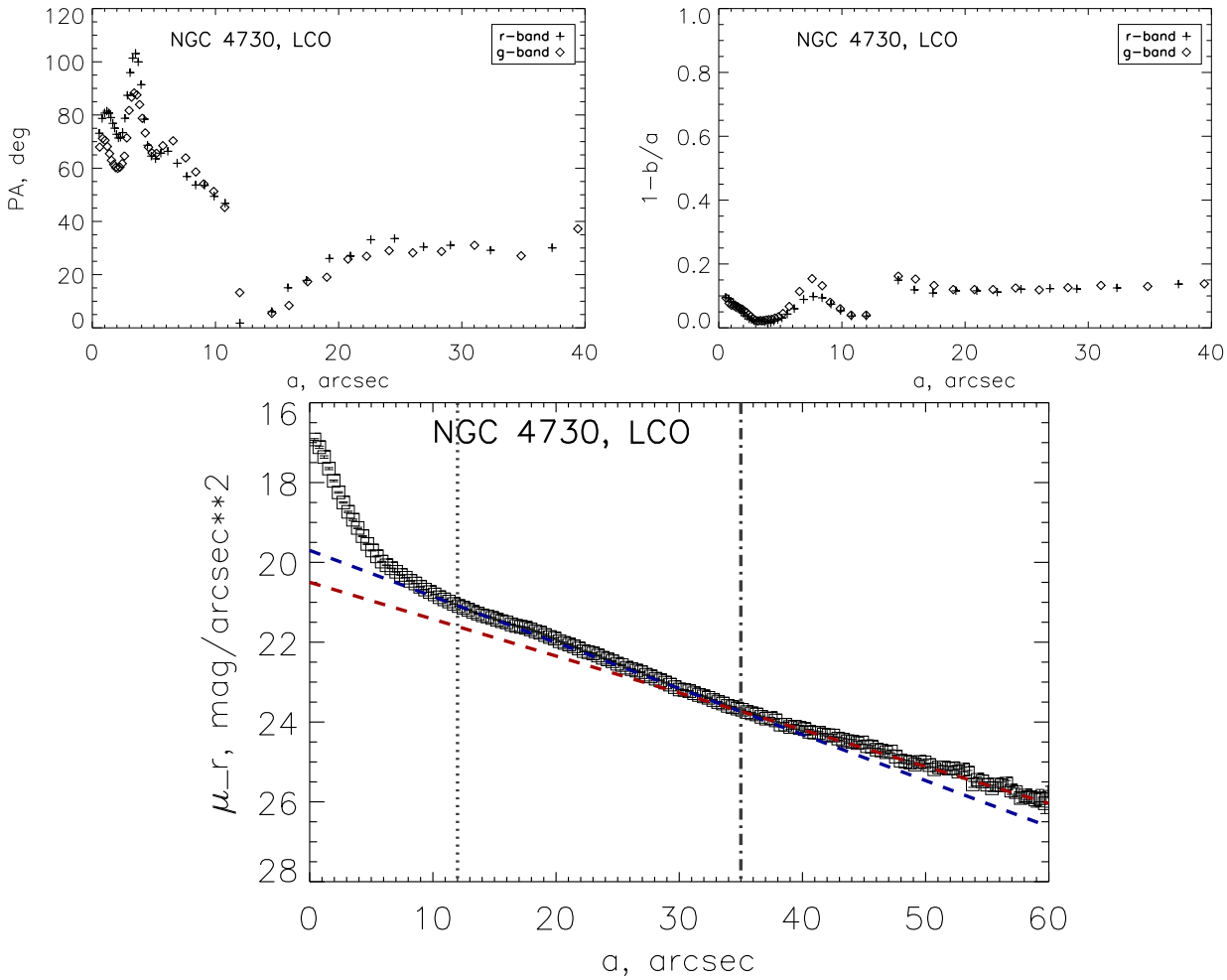

Figure 5. An example of a two-tiered (antitruncated) exponential surface-brightness profile (Type III): NGC 4730. The galaxy is seen nearly face-on, and in the center the isophotes are quite round. However, starting from $R \approx 15''$ the ellipticity stays at $\epsilon \sim 0.15$, and it is a disk-dominated area. The disk surface-brightness profile can be fitted by two exponential laws with different scalelengths, the outer scalelength being larger. Two exponential laws meet at $\sim 35''$ – it is a so called break radius, R_{brk}. We show the boundary between the bulge and the disk by a vertical dotted line; another vertical, dashed-dotted line marks the break radius.

if we deal with exponential-profile disks. The exponential scalelength for a given galactic disk can be used as a standard rule, and its visible variations with the azimuth, from h along the major axis to $h\cos i$ along the minor axis, follow a pure cosine law and provide an independent estimate of the inclination i. We divide the whole galaxy image into 18 sectors, with 20-degree opening angle each, and calculate surface-brightness profiles within all of them. These surface-brightness profiles are fitted by exponential laws, and the on-plane azimuthal distribution of the 18 (projected) scalelengths obtained in such a way is approximated by an ellipse. Just this ellipse has an axis ratio equal to $\cos i$ so giving us a possibility to determine the disk inclination.

4. THE RESULTS

Table 2 lists all 60 galaxies which have been analyzed, with mentioning the type of the disk surface-brightness profile derived and also containing notes about some structure details and color features which have been seen in the color maps. The presence of a bar was recognized if the isophote ellipticity profile had a distinct local maximum exceeding the outer ellipticity level prescribed by the disk orientation. The existence of a ring is derived from the visual inspection of the surface-brightness profiles; the rings can be or not be distinguished by the color. The color distributions demonstrate mostly red centers and smoothly reddish stellar bodies, but the low-luminosity S0s can instead possess blue nuclei. Sometimes distinct color features such as blue rings of various sizes or circumnuclear red (dust) rings can also be noted (Fig. 6).

Table 2. The galaxies studied photometrically with the LCO network.

Galaxy	Type[a]	M_H[a]	R_{25},″[b]	Type of disk profile	Bar/ring?	Color features
Abell 194						
NGC 541	S0-?	–24.3	66	I	minibar	···
NGC 557	$SB0^+$(rs)pec	–23.9	43	III	ring	a blue filament
PGC 5216	S0:	–22.35	25	III	···	···
PGC 5313	E3:	–22.3	16.5	III	ring	···
PGC 5314	S0/a	–22.4	18	III	bar	···
UGC 1003	S0	–22.9	24	III	···	···
UGC 1030	E	–23.2	31	I	···	blue disk
UGC 1043	E	–22.8	26	III	ring	blue ring
NGC 1550 group						
IC 366	E? (LEDA)	–22.15	10	III	···	···
UGC 3006	SAO^0:	–23.7	52	I	···	···
UGC 3008	$(R)SB(rs))^+$	–23.3	49	III	Bar, ring	···

Table 2 continued on next page

Table 2 *(continued)*

Galaxy	Type[a]	M_H[a]	R_{25},″[b]	Type of disk profile	Bar/ring?	Color features
UGC 3011	SA(rs)0^0:	–22.64	32	I	ring	···
Fornax						
NGC 1351	SA0^-pec:	–22.5	102	III	···	···
NGC 1380B	SAB(s)0^-:	–21.1	60	III	bar	···
NGC 1387	SAB(s)0^-	–23.44	91	II	bar	···
Centaurus						
ESO 323-012	SB0	–22.86	27	I	bar, ring	···
ESO 323-019	E+	–23.2	45	III	bar, ring	blue nuclear ring
NGC 4677	SB(s)0^+	–23.5	44	III	ring	···
NGC 4683	SB(s)0^-	–23.4	43	I	bar	···
NGC 4696B	SA0^-	–24.1	39.5	I	···	···
NGC 4730	SA(r)0^-	–23.8	38	III	···	red nuclear ring
NGC 4743	SA0^+	–23.0	52	I	ring	···
NGC 4744	SB(s)0/a	–24.1	74	I	bar, ring	dust lanes
PGC 43572	S0	–22.06	25.5	I	···	blue nuclear polar ring
PGC 43604	SB0	–22.8	27	I	Boxy bar	blue nuclear ring
PGC 43652	S0	–21.4	19	III	···	···
Hydra						
ESO 501-035	SB(r)0^0	–23.36	42	I	ring	···
ESO 501-047	SB0^0	–22.7	30	I	···	···
ESO 501-049	SB(s)0	–22.6	26	I	ring	···
ESO 501-052	(R)S0^+	–22.2	37	II	ring	blue ring
LEDA 87329	S0	–21.04	< 14	III	···	red nucleus
LEDA 141477	E/S0	–21.5	16.5	III	···	···
NGC 3307	SB(r)0/a pec	–22.6	29	I	···	···
NGC 3308	SAB(s)0^-	–24.2	36	III	···	···
NGC 3316	SB(rs)0^0	–23.96	29	III	···	···
PGC 31418	S0	–22.16	26(K)	I	···	···
PGC 31447	S0	–22.85	14	I	···	···

Table 2 continued on next page

Table 2 *(continued)*

Galaxy	Type[a]	M_H[a]	R_{25},″[b]	Type of disk profile	Bar/ring?	Color features
PGC 31450	SB(rs)0^0	–22.3	20	III	···	···
PGC 31464	S(rs)0	–22.04	17	I	ring	···
Antlia						
FS 72[c]	S0	–21.2	27	III	bar, ring	red bar, blue disk
FS 80[c]	dS0	–21.6	24	I	···	···
LEDA 83014	S0	–22.34	27	III	bar	red bar, blue disk
NGC 3257	SAB(s)0^-:	–22.5	32	III	bar	a blue filament
NGC 3258A	SAB0^+:	–22.5	37	I	ring	···
NGC 3258B	SAB(r)0:	–20.85	32	III	bar	blue semi-ring
NGC 3273	SA(r)0^0	–23.6	57	II	···	···
NGC 3289	SB(rs)0	–23.35	60	I	ring	reddish nuclear ring
Abell 3565						
ESO 383-030	SAB(rs)0^+	–23.0	42	III	rings	blue ring, red lanes
ESO 383-045	S0?	–23.9	39	III	···	···
ESO 383-049	E+?	–22.94	34.5	I	···	···
LEDA 183938	SB(rl)0^+	–22.4	31	I	bar, ring	···
Abell S0805						
ESO 104-002	S0	–22.5	32	III	···	blue disk
IC 4749	S0?	–23.94	36	I	···	···
IC 4750	SAB(r)0^+	–23.3	34.5	III	ring	···
IC 4766	SA(r)0^+	–23.54	37	III	···	red semi-ring
IC 4784	S0?	–24.7	45	III	···	···
LEDA 93525	E?(LEDA)	–23.56	35.5(K)	I	···	···
PGC 62384	SB0	–22.45	20	I	bars	blue nucleus
PGC 62436	S0	–21.65	21	III	···	···
PGC 62437	S0	–21.36	16	I	···	blue nucleus

[a]Mostly from NED; but some data taken from HyperLEDA (Makarov et al. 2014) are marked by '(LEDA)'.

[b]Mostly the optical radii are taken from HyperLEDA (Makarov et al. 2014); but some NIR radii taken from NED are marked by '(K)'.

[c]The designation of the galaxy is from the study of the Antlia cluster by Ferguson & Sandage (1990).

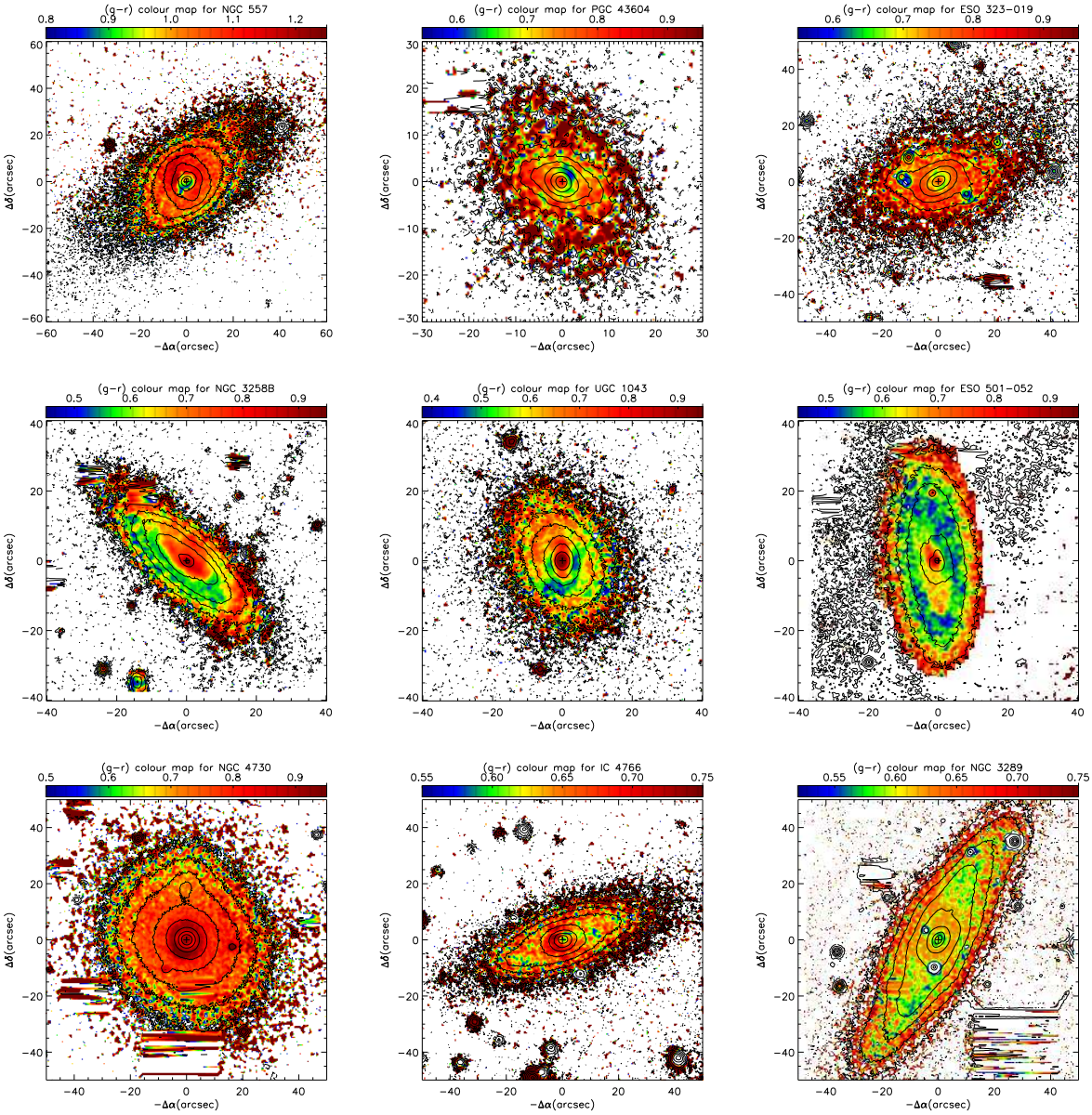

Figure 6. Some examples of the color structures: *upper row* – circumnuclear blue rings, *middle row* – large-scale blue rings, *bottom row, two left plots* – circumnuclear red rings. NGC 3289 (*the right plot in the bottom row*) demonstrates a rather complex system of blue and reddish rings.

The results of our analysis of the radial and vertical structures of the r-band images of the galactic disks are presented in the Table 3 for the radial profiles of Type I, in the Table 4 for the radial profiles of Type II, and in the Table 5 for the radial profiles of Type III, correspondingly. The radial surface-brightness profile parameters, namely, the central surface brightnesses μ_0 and the exponential scalelengths h, are obtained by fitting the profiles by exponential laws in the radius ranges noted in the Tables – following Freeman (1970), we have tried to explore the radius ranges which are at least twice larger than the exponential scalelengths; in these Tables the μ_0's are not corrected for the extinction. The relative thicknesses of some disks, q, are also presented in the Tables; they have been obtained only for the high signal-to-noise images of the disks which are far from edge-on or face-on orientation – so minus 20 galaxies of our sample. The relative thicknesses q of the S0 galactic disks, characterizing the ratio of the vertical and radial scalelengths, are presented in the Table 3 for the single-scaled exponential disks, in the Table 4 for the inner part of the truncated disk in NGC 3273, and in the Table 5 for the inner segments of the two-tiered antitruncated disks. Only one galaxy with a Type-II disk is suitable for disk thickness determination – it is NGC 3273. As for other two, NGC 1387 is too round (face-on), and ESO 501-052 is too inclined (almost edge-on).

5. DISCUSSION

5.1. *Radial structure of the S0 disks in the clusters and beyond*

Erwin et al. (2012), by analyzing radial structure of 24 S0 galaxies – members of the Virgo cluster, have concluded that the statistics of the surface-brightness profile types in the cluster differs significantly from that in the field: they have not found Type-II profiles in the Virgo S0s at all while in the field a quarter of all S0s demonstrate truncated stellar disks (Erwin et al. 2008; Gutiérrez et al. 2011). They reported the following fractions of the profile types in the Virgo: 46%±10% of the Type I, 0%±4% of the Type II, and the remaining 54% of the Type III. Our results on 60 S0 galaxies in 8 southern clusters are: 27 S0s have the profiles of Type I – 45%±6%, 3 S0s have the profiles of Type II – 5%±3% (the errors indicated correspond to the root square of the binomial distribution variance). We conclude that our results are completely consistent with the statistics of the Virgo S0s reported by Erwin et al. (2012) and also differ from the field statistics where 26%±6% of Type I and 28%±6% of Type II are reported by Erwin et al. (2012). The larger statistics of the field S0 galaxies by Laine et al. (2014) obtained through the photometry in the NIR bands gives around 40 percent both for the Type I and Type II. So we confirm the probable deficit of the Type-II surface-brightness profiles in the lenticulars in clusters with respect to the field. If to compare our results with the results of the STAGES survey (Maltby et al. 2015) where the difference of the disk profile types between the cluster A901/902 and the field projected onto the cluster at lower photometric redshifts has not been found, we must recognize disagreement concerning the proportion of the Type I first of all: in our sample about half of all cluster S0s have one-scaled exponential disks while in the A901/902 cluster only 25 percent S0s with Type I disks are detected by Maltby et al. (2015). Interestingly, all other profile types demonstrate consistency of their fraction in dense environment including the absence of the Type II. The explanation of the disagreement concerning the Type I may be the note of Maltby et al. (2015) that 20 percent of their cluster S0s have no any exponential parts in their profiles al all. Since we have selected our S0 sample just by checking if they have exponential pieces in their outer surface-brightness profiles, there is an evident difference in our and STAGES approaches to the S0 sample selection.

Table 3. Parameters of the Type-I disks

Galaxy	Radius range, $''$	$\mu_{0,r}$, mag/$\square''$	h_r, $''$	h_r, kpc	q
NGC 541	20–80	20.2	21.21 ± 0.01	7.020 ± 0.003	
UGC 1030	15–35	20.4	8.78 ± 0.13	2.91 ± 0.04	0.375
UGC 3006	25–58	19.5	14.01 ± 0.01	3.334 ± 0.002	0.22
UGC 3011	17–42	19.1	9.49 ± 0.09	2.26 ± 0.02	0.42
ESO 323-012	13–30	19.0	9.29 ± 0.14	1.97 ± 0.03	
NGC 4683	23–44	20.9	14.41 ± 0.19	3.05 ± 0.04	0.35
NGC 4696B	18–50	19.7	11.84 ± 0.01	2.510 ± 0.002	0.46
NGC 4743	16–35	19.1	9.94 ± 0.11	2.11 ± 0.02	0.34
NGC 4744	45–85	20.9	24.90 ± 0.03	5.279 ± 0.006	0.28
PGC 43572	12–24	20.0	6.42 ± 0.32	1.36 ± 0.07	
PGC 43604	11–24	20.7	8.99 ± 0.35	1.91 ± 0.07	
ESO 501-035	25–50	20.8	15.27 ± 0.32	4.15 ± 0.09	
ESO 501-047	8–25	19.3	6.64 ± 0.04	1.806 ± 0.011	0.36
ESO 501-049	11–31	20.1	8.38 ± 0.08	2.28 ± 0.02	0.31
NGC 3307	8–24	19.1	5.93 ± 0.06	1.61 ± 0.02	0.31
PGC 31418	12–24	19.6	5.25 ± 0.16	1.43 ± 0.04	0.31
PGC 31447	10–25	19.1	5.84 ± 0.11	1.59 ± 0.03	0.31
PGC 31464	5–16	19.7	4.94 ± 0.05	1.34 ± 0.01	0.45
NGC 3258A	9–32	18.9	7.19 ± 0.01	1.474 ± 0.002	0.27
NGC 3289	30–55	18.8	13.40 ± 0.01	2.747 ± 0.002	0.16
Antlia: FS80	10–28	18.8	6.22 ± 0.04	1.275 ± 0.008	0.25
ESO 383-049	6–37	18.7	6.910 ± 0.003	1.810 ± 0.001	0.13
LEDA 183938	22–32	20.9	8.15 ± 0.42	2.14 ± 0.11	0.27
LEDA 93525	12–24	19.9	7.63 ± 0.11	2.23 ± 0.03	
PGC 62384	9–22	20.2	5.83 ± 0.08	1.70 ± 0.02	
PGC 62437	4–12	20.5	4.64 ± 0.04	1.355 ± 0.012	
IC 4749	9–37	21.5^a	11.77 ± 0.37^a	3.44 ± 0.11^a	

[a]The r-image was badly guided so here we use the g-band image.

Table 4. Parameters of the Type-II disks

Galaxy	Inner disk							Outer disk			
	Range, $''$	$\mu_{0,r}$, mag/□$''$	h_r, $''$	h_r, kpc	q	μ_{brk}, mag/□$''$	R_{brk}, $''$	Range, $''$	$\mu_{0,r}$, mag/□$''$	h_r, $''$	h_r, kpc
NGC 3273	16–30	19.7	16.33 ± 0.01	3.35 ± 0.00	0.13	21.7	29.1 ± 0.1	35–70	18.8	11.15 ± 0.01	2.29 ± 0.00
ESO 501-052	10–18	21.1	30.38 ± 1.19	8.26 ± 0.32		21.8	17.9 ± 0.5	20–33	20.1	11.84 ± 0.01	3.22 ± 0.00
NGC 1387	30–85	19.9	24.74 ± 0.00	2.18 ± 0.00		24.2	99.8 ± 1.7	102–114	13.5	10.05 ± 0.10	0.88 ± 0.01

As for the Type III, it seems probable that the environment does not affect the occurence of the antitruncated profiles. The fraction of Type-III profiles in S0s remains almost the same, half of all, in the field and in the clusters according to our results as well as to the results by Erwin et al. (2012) and by Maltby et al. (2015). With the profile parameters derived by us for our cluster sample S0s, presented in the Table 5, we can compare the scaling relations for the Type-III S0s in the clusters and in the field; we do it in Fig. 7. The linear dependencies between the characteristics of the inner-disk exponential fit, $\mu_{0,i}$ vs h_i, and between the characteristics of the outer-disk exponential fits, $\mu_{0,o}$ vs h_o, as well as between $\mu_{0,o} - \mu_{0,i}$ and h_i/h_o, were found by Borlaff et al. (2014) for the field sample compiled over the works by Erwin et al. (2008) and by Gutiérrez et al. (2011). To compare their scaling relations with our data, we shift their linear dependencies by +0.22 mag, to transform the R-band into the r-band (Jordi et al. 2006); and the individual disk central surface brightnesses for the comparison sample of the field S0s (crosses in Fig. 7) are transformed into the r-band by using the formula (1) from Gutiérrez et al. (2011) giving the similar shift. After that, one can see that the inner disks look almost the same in the clusters and in the field (Fig. 7, upper plot). The outer segments of the Type-III profiles of the S0s in the clusters demonstrate the correlation between μ_0, o and h_o with the same slope as the S0s in the field but are slightly shifted to higher central surface brightnesses (Fig. 7, middle plot). And the best correlation among all found by Borlaff et al. (2014), $\mu_0, o - \mu_0, i$ vs h_i/h_o, is strictly the same in the field and in the clusters (Fig. 7, bottom plot).

5.2. *Vertical structure of the S0 disks in clusters and in the field*

The novel point of our photometric analysis is individual estimates of the stellar disk relative thicknesses expressed in the terms of Hubble (1926)'s q – see the Table 3, the Table 4, and the Table 5.

Figure 8 presents the distributions of the relative disk thicknesses for the Type-I disks (*left*) and for the inner segments of the Type-III disks (*right*). The Type-I distribution looks like a regular normal law, rather narrow one. The distribution for the inner disks of Type-III profiles is obviously bimodal, with two distinct maxima near $q = 0.3$ and $q = 0.6$. Indeed, we can easily mess the inner segments of the Type-III disks with *pseudobulges*: the latters have also exponential surface brightness profiles but must be *much thicker* than the disks – because they are *bulges*. We have calculated the mean thicknesses of the Type-I disks and of the *true* inner disks of Type-III – those with $q < 0.5$. We have obtained: $\langle q \rangle = 0.31 \pm 0.02$ for the Type I disks and $\langle q \rangle = 0.25 \pm 0.02$ for the inner disks of the Type-III profiles. Let us compare these estimates with similar estimates for the field sample which we have presented in our first paper exploring our method of disk thickness measurement

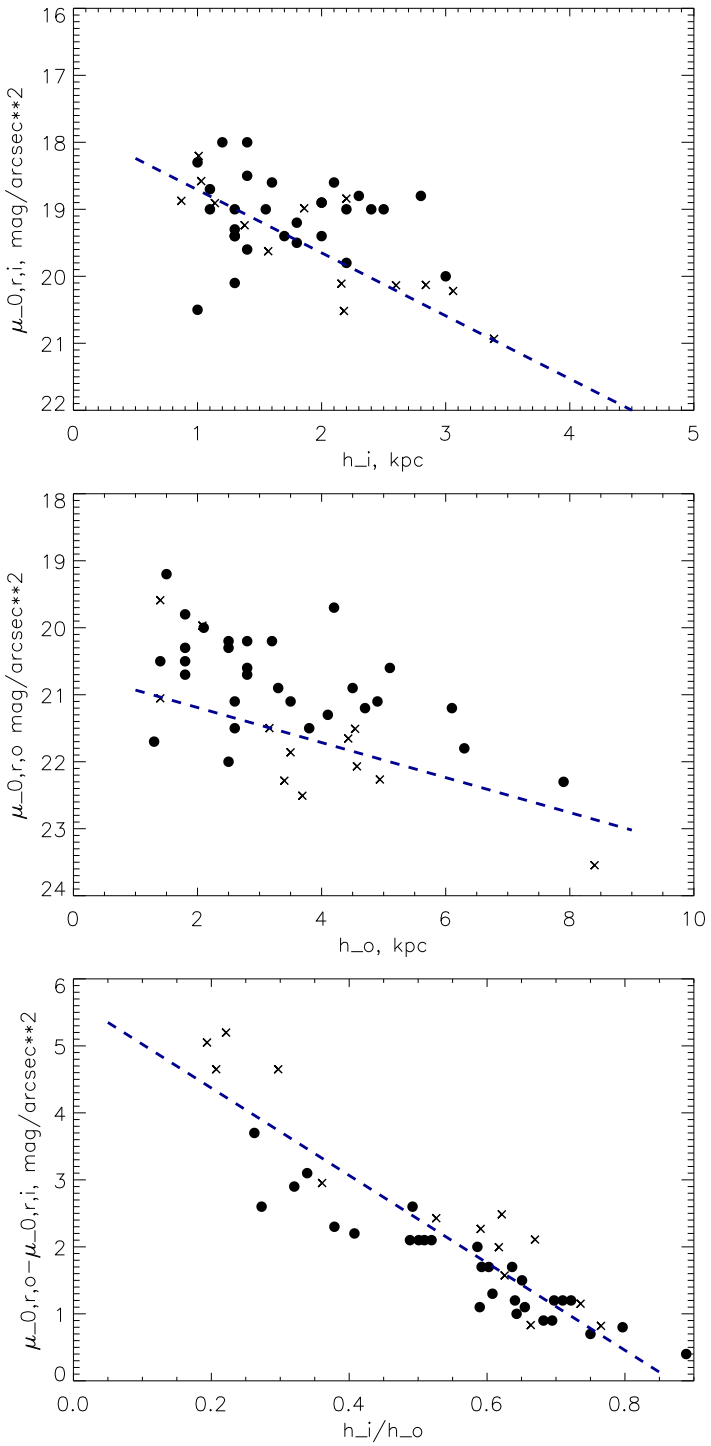

Figure 7. Scaling relations for the two-tiered (antitruncated) exponential surface-brightness profiles (Type III) in our sample galaxies (black points): *upper plot* – the central surface brightness corrected for the Galactic extinction according to NED vs exponential scalelength for the inner disks, $\mu_{0,i}$ vs h_i; *middle plot* – the central surface brightness corrected for the Galactic extinction according to NED vs exponential scalelength for the outer disks, $\mu_{0,o}$ vs h_o; *bottom plot* – the combined relation, $\mu_{0,o} - \mu_{0,i}$ versus h_i/h_o. By dashed blue straight lines we plot the scaling relations found by Borlaff et al. (2014) for the field S0 sample compiled over the works by Erwin et al. (2008) and by Gutiérrez et al. (2011), the crosses are individual galaxies from Erwin et al. (2008) and Gutiérrez et al. (2011) representing the field S0 population.

Table 5. Parameters of the Type-III disks

Galaxy	Inner disk					Outer disk					
	Range, $''$	$\mu_{0,r}$, mag/□$''$	h_r, $''$	h_r, kpc	q	μ_{brk} mag/□$''$	R_{brk} $''$	Range, $''$	$\mu_{0,r}$, mag/□$''$	h_r, $''$	h_r, kpc
NGC 557	12–24	19.1	7.55 ± 0.08	2.50 ± 0.03	0.54	22.8	25.9 ± 1.4	30–47	21.3	18.42 ± 0.69	6.1 ± 0.2
PGC 5216	7–14	19.3	5.42 ± 0.00	1.79 ± 0.00	0.155	21.8	14.1 ± 1.8	14–22	20.3	8.38 ± 0.12	2.77 ± 0.04
PGC 5313	8–15	18.1	3.56 ± 0.03	1.18 ± 0.01		22.8	15.4 ± 0.7	18–35	21.2	10.5 ± 0.5	3.48 ± 0.16
PGC 5314	9–15	19.9	6.75 ± 0.12	2.23 ± 0.04		24.1	25.9 ± 1.7	21–44	21.6	11.4 ± 0.4	3.77 ± 0.13
UGC 1003	10–20	18.7	4.89 ± 0.04	1.62 ± 0.01	0.30	23.4	21.2 ± 2.2	21–35	20.4	7.66 ± 0.30	2.54 ± 0.10
UGC 1043	7–18	19.5	5.46 ± 0.04	1.81 ± 0.01	0.54	23.5	17.4 ± 2.1	20–32	20.7	8.37 ± 0.25	2.77 ± 0.08
IC 366	10–21	19.7	5.64 ± 0.08	1.34 ± 0.02	0.31	24.0	22.3 ± 2.4	23–37	21.8	11.02 ± 0.91	2.62 ± 0.22
UGC 3008	5–12	18.3	5.80 ± 0.11	1.38 ± 0.03	0.27	21.9	19.1 ± 0.4	40–60	20.9	21.25 ± 0.58	5.06 ± 0.14
NGC 1351	15–30	18.7	12.24 ± 0.01	1.08 ± 0.00	0.42	21.4	30.4 ± 2.7	40–78	19.8	20.68 ± 0.02	1.82 ± 0.00
NGC 1380B	15–45	20.5	10.90 ± 0.00	0.96 ± 0.00	0.69	25.0	43.2 ± 7.6	45–65	21.7	15.12 ± 0.55	1.33 ± 0.05
ESO 323-019	13–28	19.2	8.62 ± 0.20	1.83 ± 0.04		23.0	30.0 ± 2.8	35–55	21.2	18.3 ± 1.8	3.88 ± 0.38
NGC 4677	30–45	19.3	11.46 ± 0.01	2.43 ± 0.00		23.5	44.2 ± 4.4	50–80	21.4	22.96 ± 1.21	4.87 ± 0.26
NGC 4730	12–36	19.7	9.41 ± 0.00	2.00 ± 0.00		23.6	34.6 ± 9.8	40–60	20.5	11.77 ± 0.47	2.50 ± 0.10
PGC 43652	7–18	20.4	5.97 ± 0.07	1.27 ± 0.02	0.71	23.6	19.0 ± 10.4	21–40	20.8	6.75 ± 0.35	1.43 ± 0.07
LEDA 87329	6–16	19.2	3.94 ± 0.03	1.07 ± 0.01		23.4	15.2 ± 1.3	19–25	20.9	6.64 ± 0.22	1.81 ± 0.06
LEDA 141477	8–16	19.8	5.15 ± 0.10	1.40 ± 0.03	0.20	22.7	13.8 ± 1.1	16–26	20.5	6.78 ± 0.04	1.84 ± 0.01
NGC 3308	8–28	19.0	10.45 ± 0.01	2.84 ± 0.00	0.61	22.0	27.0 ± 3.0	30–62	19.9	15.40 ± 0.01	4.19 ± 0.00
NGC 3316	10–22	19.1	7.43 ± 0.01	2.02 ± 0.00	0.56	23.4	29.2 ± 1.7	40–60	22.0	23.13 ± 1.28	6.29 ± 0.35
PGC 31450	9–18	19.6	6.2 ± 0.1	1.69 ± 0.03	0.20	22.9	18.9 ± 1.8	20–35	20.9	10.2 ± 0.4	2.77 ± 0.11
Antlia: FS 72	2–13	18.5	5.04 ± 0.04	1.03 ± 0.01	0.13	21.5	13.9 ± 1.8	15–30	19.4	7.20 ± 0.14	1.48 ± 0.03
LEDA 83014	16–28	19.6	6.14 ± 0.14	1.26 ± 0.03	0.28	24.7	29.1 ± 0.4	30–45	22.2	12.41 ± 0.24	2.54 ± 0.05
NGC 3257	7–18	19.2	6.28 ± 0.04	1.29 ± 0.01	0.56	23.5	23.9 ± 1.5	29–54	21.3	12.75 ± 0.35	2.61 ± 0.07
NGC 3258B	12–28	18.7	6.79 ± 0.06	1.39 ± 0.01		23.3	26.8 ± 4.9	30–50	20.2	10.45 ± 0.80	2.14 ± 0.16
ESO 383-030	10–35	20.1	11.42 ± 0.01	2.99 ± 0.00	0.13	23.4	35.2 ± 4.7	35–50	21.3	17.80 ± 0.52	4.66 ± 0.14
ESO 383-045	8–28	18.7	7.93 ± 0.15	2.08 ± 0.04	0.27	23.9	37.7 ± 0.6	45–80	22.5	30.1 ± 1.3	7.89 ± 0.34
ESO 104-002	6–17	19.2	5.33 ± 0.04	1.56 ± 0.01	0.26	22.8	18.2 ± 0.9	18–50	21.5	14.0 ± 0.4	4.09 ± 0.12
IC 4750	16–30	19.3	7.63 ± 0.08	2.23 ± 0.02	0.30	23.6	28.1 ± 5.6	32–48	20.5	10.9 ± 0.7	3.18 ± 0.20
IC 4766	18–32	19.0	8.03 ± 0.08	2.34 ± 0.02		23.3	32.5 ± 1.8	32–54	21.1	15.4 ± 0.4	4.50 ± 0.12
PGC 62436	6–16	19.5	4.36 ± 0.04	1.27 ± 0.01	0.28	23.7	16.0 ± 2.7	18–26	20.7	6.24 ± 0.32	1.82 ± 0.09
IC 4784	12–26	20.3[a]	9.67 ± 0.01	2.82 ± 0.00		23.3[a]	24.1 ± 2.2	28–48	21.4[a]	16.28 ± 0.02	4.75 ± 0.01

[a]The r-image was badly guided so here we use the g-band image.

(Chudakova & Sil'chenko 2014): $\langle q \rangle = 0.46 \pm 0.05$ for the Type-I disks and $\langle q \rangle = 0.22 \pm 0.045$ for the inner disks of the Type-III profiles. We see again that the Type-III disks, in particular their inner segments, are *the same* in the field and in the clusters while the Type-I disks look *thinner* in dense environments. Intuitively, one could expect the opposite trend: in dense environments the stellar disks had to be more dynamically heated due to frequent tidal interactions. However, it is not the first detected signature of more common accretion events in rarified environments (Katkov, Sil'chenko, and Afanasiev 2014).

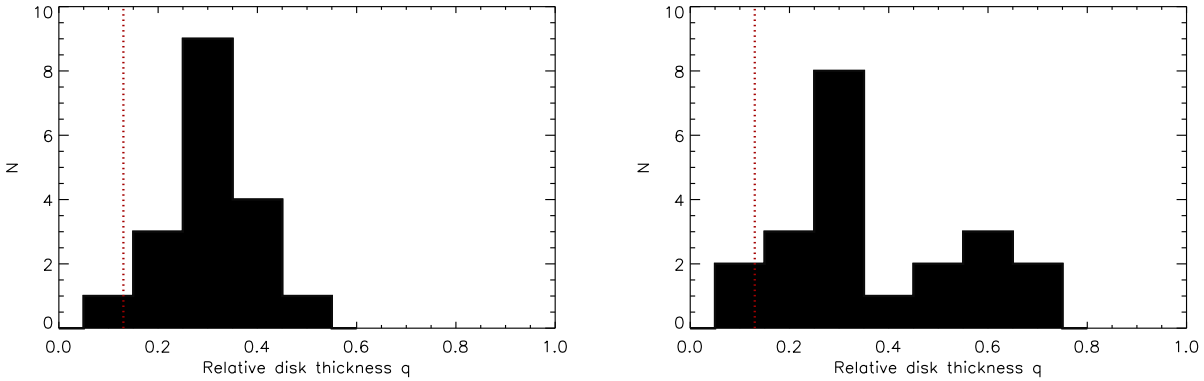

Figure 8. The distributions of the disk relative thickness for the Type-I disks (*left*) and for the inner segments of the Type-III disks (*right*). The red vertical dotted line shows the only available thickness of the inner Type-II disk segment for NGC 3273.

Here we must note that after removing false Type-III disks where the inner segments are in fact pseudobulges, the fraction of Type-III disks in the whole sample is diminished and the fraction of Type-I disks is probably increased. But to compare the proportions of various disk types in the clusters and in the field, we must use initial results because during the previous field S0 sample investigations there were no checking inner disk thickness.

5.3. *Environment-driven evolution?*

Recently the first theoretical interpretation of the absence of Type-II profiles and prevalence of Type-I profiles in cluster disk galaxies has been proposed. Clarke et al. (2017) have simulated the process of stellar disk growth in an isolated spiral galaxy and in the same galaxy after its infall into a cluster with the Fornax-like parameters. They have found that when the infalling galaxy comes close to the cluster center, at a distance of 20% of the cluster virial radius, its Type-II surface density profile transforms into a pure single-scale exponential one – or becomes a Type-I profile. The physical mechanism of this transformation may be the effect of tidally driven transient spirals in the outer parts of the disk. Effective migration of disk stars into its outermost parts under the spiral density wave pressure removes any break of the surface density distribution at intermediate radii and produces purely exponential form of the disk profile in its final state. Interestingly, the galaxies suffer only radial-profile transformation, without significant disk thickening and/or dynamical heating. If really the cluster gravitational potential impact provides so effective stellar radial migration in the galactic disks, it may explain not only the absence/rarity of the Type-II disks in clusters, but also the brighter outer parts in the Type-III disks of the cluster S0s (Fig. 7). Indeed, the effect of stellar migration outward must act not only on Type-II disks; it must affect all infalling disk galaxies including Type-III ones. In the Type-III disks the effective stellar migration outward would strengthen the outer parts of the disks, and just this effect is found by us for the cluster S0s with the Type-III surface-brightness profiles in Fig. 7.

6. CONCLUSIONS

We have analyzed the structure of the large-scale stellar disks in 60 lenticular galaxies – members of 8 southern clusters. The parameters of the radial surface-brightness profiles have been determined, and all the galaxies have been classified according to three types proposed by Pohlen & Trujillo (2006).

We confirm the result by Erwin et al. (2012) that the proportion of surface-brightness profile types is significantly different in clusters and in the field: in the clusters the Type-II profiles are almost absent while according to the literature data, in the field they constitute about one quarter of all lenticular galaxies. The Type-III profiles are equally represented in the clusters and in the field, and they follow similar scaling relations; marginally we detect higher surface brightnesses for the outer segments of the Type-III disks in the clusters. Also by applying our novel method (Chudakova & Sil'chenko 2014) we have determined the relative thicknesses (the vertical-to-radial scale ratios) for the stellar disks in 18 Type-I galaxies and for 21 inner segments of the Type-III disks. The relative thicknesses of the Type-I disks seem to be in average smaller in our galaxies belonging to the clusters than it has been found by us earlier for the field Type-I S0s (Chudakova & Sil'chenko 2014); perhaps it is due to the pollution of the subsample of the cluster Type-I disks by former Type-II disks which may be re-structured during the galaxy infall into clusters (Clarke et al. 2017). Among the inner segments of the Type-III disks we have found 7 pseudobulges, with the average relative thickness of $q = 0.6$; since it is a third of our Type-III disk thicknesses determined, we note that a real fraction of Type-III disks must be lower than it is thought up to now: some of the disks classified as Type-III ones may represent a combination of a pseudobulge and a Type-I disk. The remaining 14 inner segments of our Type-III disks have on average the same relative thickness, $q = 0.25 \pm 0.02$, as the Type-III S0 galaxies in the field.

This work is based on the imaging data obtained with the LCO robotic telescope network. We acknowledge the usage of the HyperLEDA database (http://leda.univ-lyon1.fr). This research has made use of the NASA/IPAC Extragalactic Database (NED) which is operated by the Jet Propulsion Laboratory, California Institute of Technology, under contract with the National Aeronautics and Space Administration. For the purpose of our photometric calibration we have used SDSS/DR9 (Ahn et al. 2012) and Pan-STARRS1 data (Chambers et al. 2016; Flewelling et al. 2016). Funding for the SDSS-III has been provided by the Alfred P. Sloan Foundation, the Participating Institutions, the National Science Foundation, and the U.S. Department of Energy Office of Science. The SDSS-III Web site is http://www.sdss3.org/. SDSS-III is managed by the Astrophysical Research Consortium for the Participating Institutions of the SDSS-III Collaboration including the University of Arizona, the Brazilian Participation Group, Brookhaven National Laboratory, Carnegie Mellon University, University of Florida, the French Participation Group, the German Participation Group, Harvard University, the Instituto de Astrofisica de Canarias, the Michigan State/Notre Dame/JINA Participation Group, Johns Hopkins University, Lawrence Berkeley National Laboratory, Max Planck Institute for Astrophysics, Max Planck Institute for Extraterrestrial Physics, New Mexico State University, New York University, Ohio State University, Pennsylvania State University, University of Portsmouth, Princeton University, the Spanish Participation Group, University of Tokyo, University of Utah, Vanderbilt University, University of Virginia, University of Washington, and Yale University. The Pan-STARRS1 Surveys (PS1) and the PS1 public science archive have been made possible through contributions by the Institute for Astronomy, the University of Hawaii, the Pan-STARRS Project Office, the Max-Planck Society and its participating institutes, the Max Planck Institute for Astronomy, Heidelberg and the Max Planck Institute for Extraterrestrial Physics, Garching, The Johns Hopkins University, Durham University, the University of Edinburgh, the Queen's University Belfast, the Harvard-Smithsonian Center for Astrophysics, the Las Cumbres Observatory Global

Telescope Network Incorporated, the National Central University of Taiwan, the Space Telescope Science Institute, the National Aeronautics and Space Administration under Grant No. NNX08AR22G issued through the Planetary Science Division of the NASA Science Mission Directorate, the National Science Foundation Grant No. AST-1238877, the University of Maryland, Eotvos Lorand University (ELTE), the Los Alamos National Laboratory, and the Gordon and Betty Moore Foundation.

REFERENCES

Ahn, C. P., Alexandroff, R., Allende Prieto, C., Anderson, S. F., Anderton, T., et al., 2012, ApJS, 203, Aid.21

Baillard, A., Bertin, E., de Lapparent, V., Fouqué, P., Arnouts, S., et al., 2011, A&A, 532, Aid. 74

Borlaff, A., Eliche-Moral, M. C., Rodr´Iguez-Pérez, C., Querejeta, M., Tapia, T., et al. 2014, A&A, 570, Aid.103

Brown, T. M., Baliber, N., Bianco, F. B., Bowman, M., Burleson, B., et al. 2013, PASP, 125, 1031

Buta, R. J., Sheth, K., Athanassoula, E., Bosma, A., Knapen, J. H., et al., 2015, ApJS, 217, Aid. 32

Cappellari, M., Emsellem, E., Krajnovic, D., et al., 2011, MNRAS, 413, 813

Chambers, K. C., Magnier, E. A., Metcalfe, N., Flewelling, H. A., Huber, M. E., et al., 2016, ArXiv: 1612.05560

Chudakova, E. M., Sil'chenko, O. K. 2014, Astron. Reports, 58, 281; ArXiv: 1410.6713

Chudakova, E. M., Katkov, I. Yu., 2019, in preparation

Clarke, A. J., Debattista, V. P., Roskar, R., Quinn, T. 2017, MNRAS, 465, L79

Dressler, A. 1980, ApJ, 236, 351

Eliche-Moral, M. C., Borlaff, A., Beckman, J. E., Gutiérrez, L. 2015, A&A, 580, Aid.33

Erwin, P., Beckman, J. E., Pohlen, M. 2005, ApJL, 626, L81

Erwin, P., Pohlen, M., Beckman, J. E. 2008, AJ, 135, 20

Erwin, P., Gutiérrez, L., Beckman, J. E. 2012, ApJL, 744, L11

Fasano, G., Poggianti, B.M., Bettoni, D., D'Onofrio, M., Dressler, A., et al., 2015, MNRAS, 449, 3927

Ferguson, H. C., Sandage, A. 1990, AJ, 100, 1

Flewelling, H. A., Magnier, E. A., Chambers, K. C., Heasley, J. N., Holmberg, C., et al., 2016, ArXiv: 1612.05243

Freeman, K. C. 1970, ApJ, 160, 767

Gutiérrez, L., Erwin, P., Aladro, R., Beckman, J. E. 2011, AJ, 142, Aid.145

Hubble, E. 1926, ApJ, 64, 321

Jordi, K., Grebel, E. K., Ammon, K. 2006, A&A, 460, 339

Katkov, I. Yu., Sil'chenko, O. K., Afanasiev, V. L., 2014, MNRAS, 438, 2798

Katkov, I. Yu., Kniazev, A. Yu., Sil'chenko, O.K. 2015, AJ, 150, Aid.24

Laine, J., Laurikainen, E., Salo, H., Comerón, S., Buta, R. J., et al., 2014, MNRAS, 441, 1992

Laurikainen, E., Salo, H., Buta, R., Knapen, J. H., Comerón, S. 2010, MNRAS, 405, 1089

Lauberts, A., Valentijn, E. A., 1989, The Messenger, 56, 31

Makarov, D., Prugniel, P., Terekhova, N., Courtois, H., Vauglin, I., 2014, A&A, 570, Aid. 13

Maltby, D. T., Aragón-Salamanca, A., Gray, M. E., Hoyos, C., Wolf, Ch., et al., 2015, MNRAS, 447, 1506

Mosenkov, A. V., Sotnikova, N. Ya., Reshetnikov, V. P. 2010, MNRAS, 401, 559

Mosenkov, A. V., Sotnikova, N. Ya., Reshetnikov, V. P., Bizyaev, D. V., Kautsch, S. J. 2015, MNRAS, 451, 2376

Naim, A., Lahav, O., Buta, R. J., et al. 1995, MNRAS, 274, 1107

Panagoulia, E. K., Fabian, A. C., Sanders, J. S. 2014, MNRAS, 438, 2341

Pohlen, M., Trujillo, I. 2006, A&A, 454, 759

Pranger, F., Trujillo, I., Kelvin, L. S., Cebrián, M. 2017, MNRAS, 467, 2127

Ruiz-Lara, T., Few, C.G., Florido, E., Gibson, B.K., Pérez, I., Sánchez-Blázquez, P., 2017, A&A, 608, Aid. 126

Sil'chenko, O. K., Burenkov, A. N., Vlasyuk, V. V. 1998, New Astron., 3, 15

Sil'chenko, O. K., Koposov, S. E., Vlasyuk, V. V., Spiridonova, O.I. 2003, Astron. Reports, 47, 88

Sil'chenko, O. K., Kniazev, A. Yu., Chudakova, E. M. 2016, Astron. Reports, 60, 73

Van der Kruit, P. C., Searle, L. 1981, A&A, 95, 105

Walker, I. R., Mihos, J. Ch., Hernquist, L., 1996, ApJ, 460, 121

Wilman, D. J., Erwin, P. 2012, ApJ, 746, Aid.160

Younger, J. D., Cox, T. J., Seth, A. C., Hernquist, L. 2007, ApJ, 670, 269

APPENDIX

A. ATLAS OF THE S0 GALAXIES STUDIED PHOTOMETRICALLY

1 Abell 194

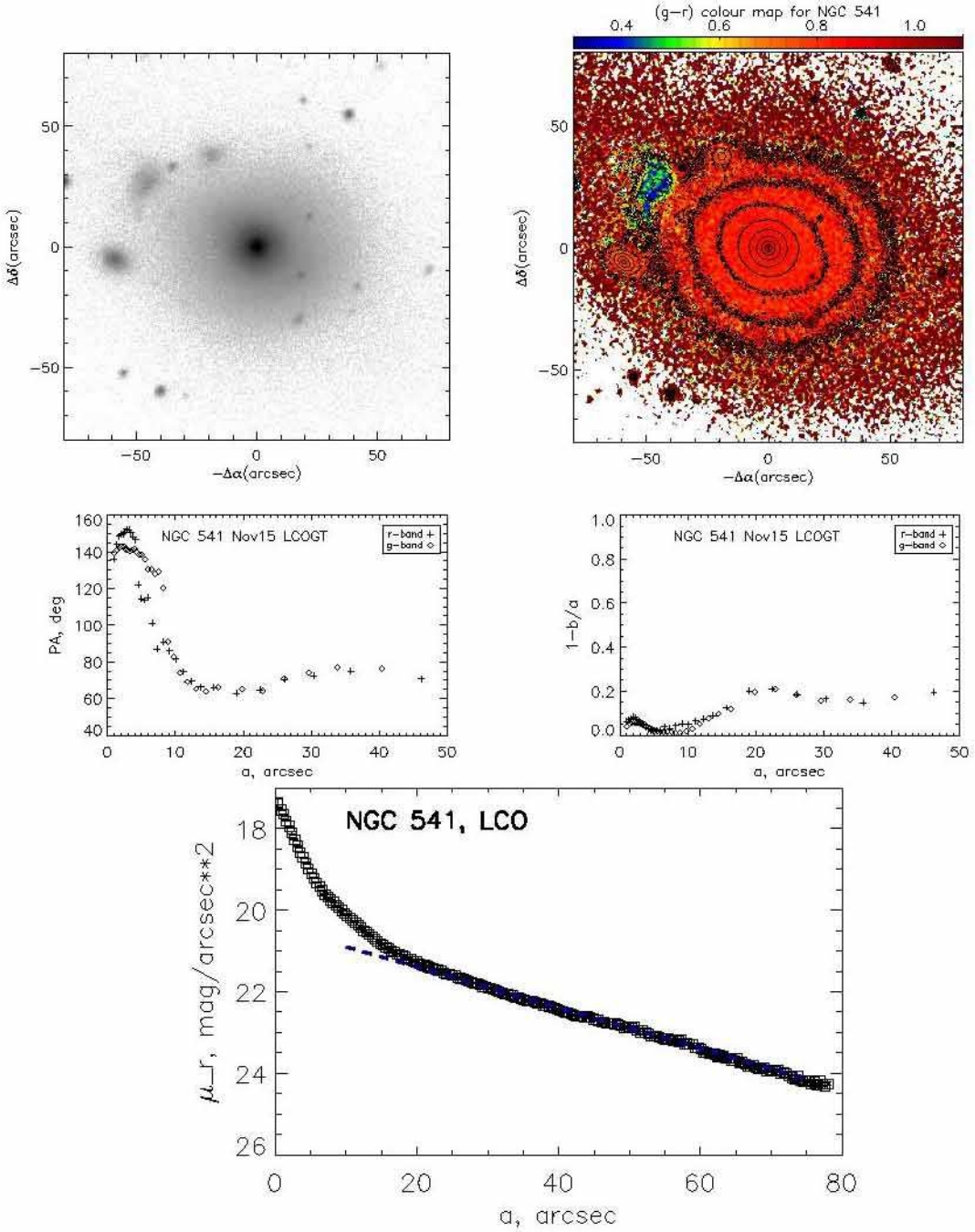

Figure 1: The LCO results for NGC 541: *the upper row:* the r-band image, logarithmically scaled, to the left, and the color $(g-r)$ map to the right; *the middle row:* the results of isophote analysis – radial profile of the major axis position angle to the left and that of the isophote ellipticity to the right; *the bottom plot:* azimuthally averaged r-band surface brightness profile, with the exponential fit for the disk-dominated radius range overplotted by the blue dashed line.

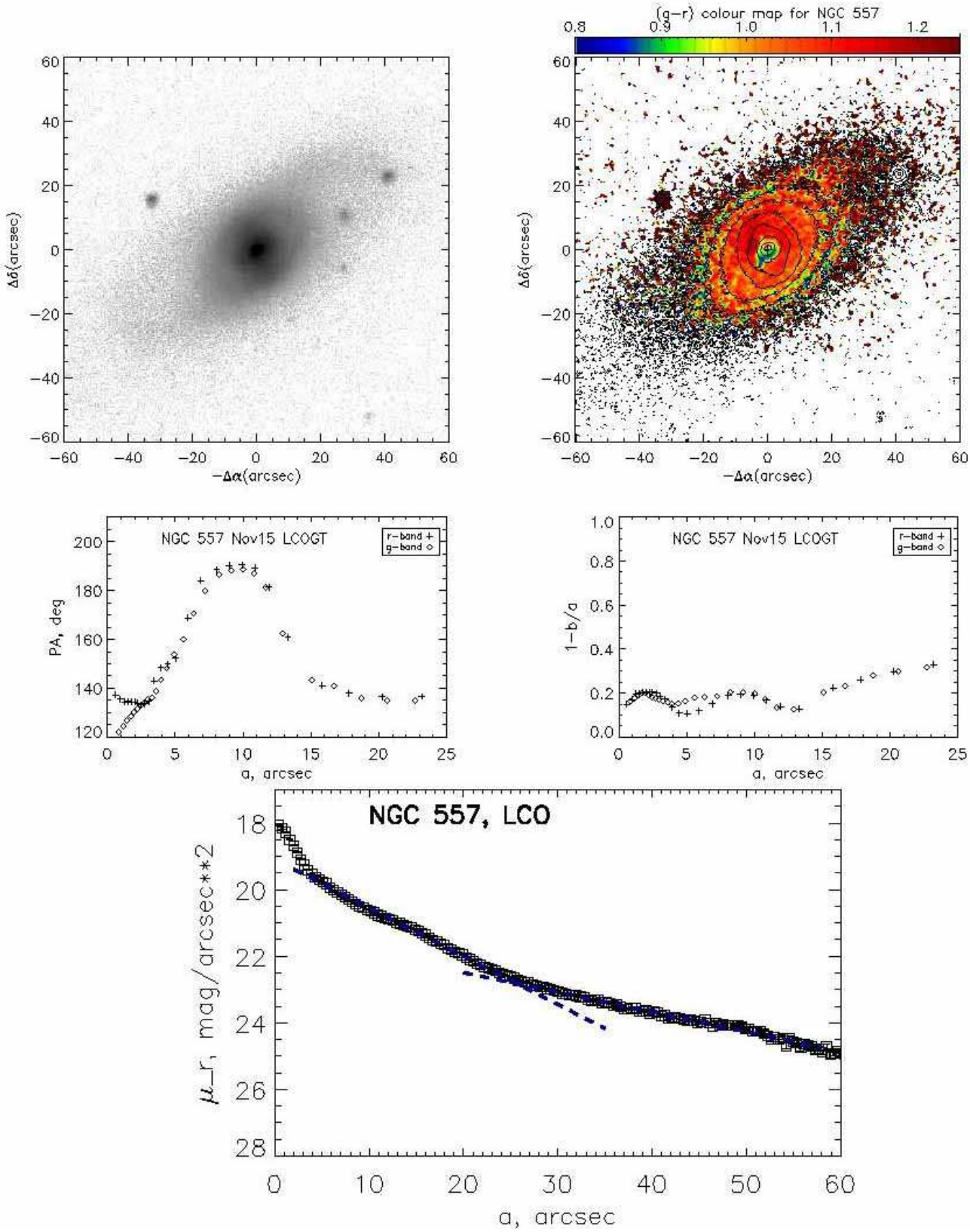
(g−r) colour map for NGC 557
0.8
0.9
1.0
1.1
1.2
Δδ(arcsec)
−Δα(arcsec)
NGC 557 Nov15 LCOGT
r−band +
g−band ◇
PA, deg
a, arcsec
1−b/a
NGC 557, LCO
μ_r, mag/arcsec**2
a, arcsec

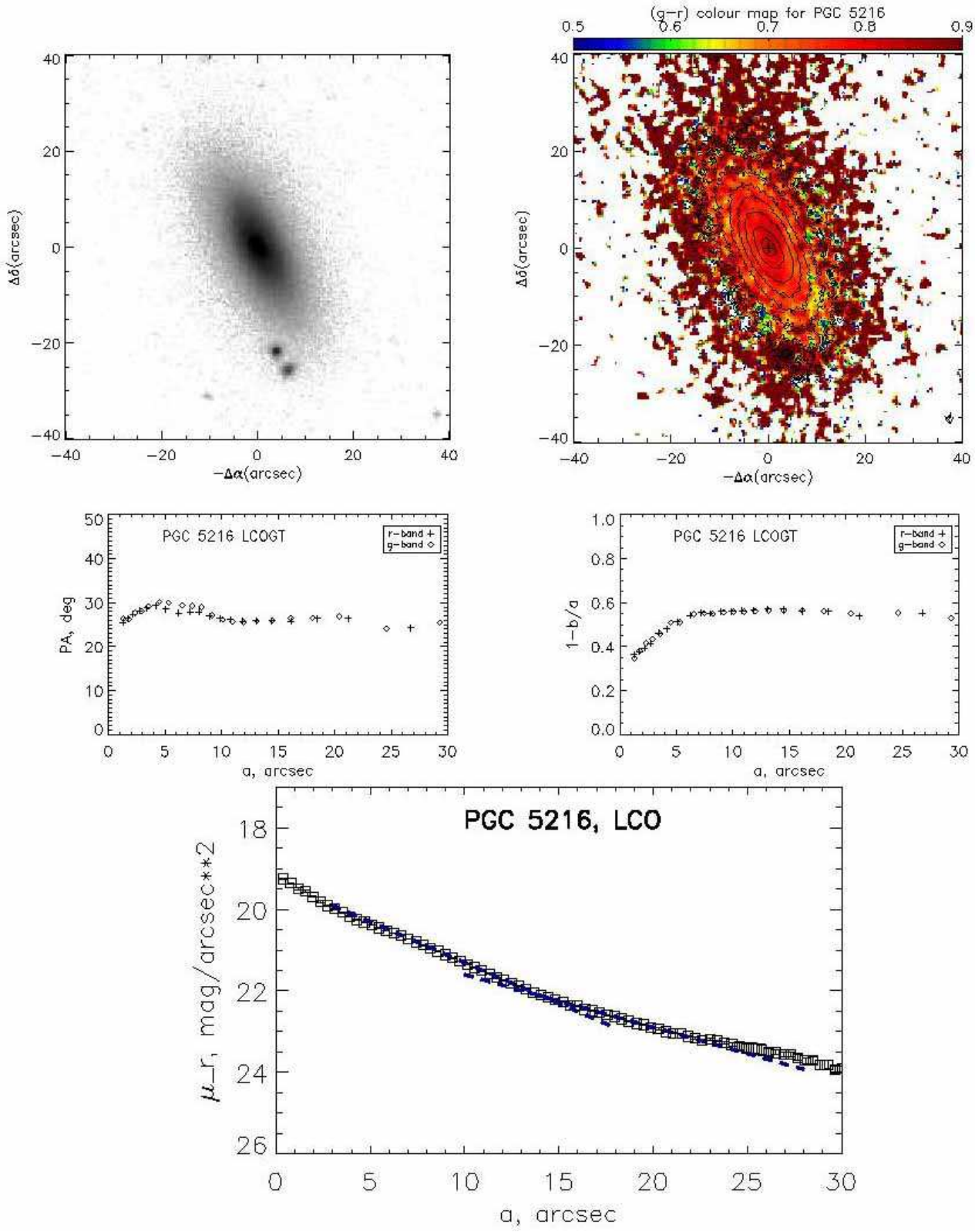
(g−r) colour map for PGC 5216
0.5
0.6
0.7
0.8
0.9
Δδ(arcsec)
−Δα(arcsec)
PGC 5216 LCOGT
r−band +
g−band ◇
PA, deg
a, arcsec
1−b/a
PGC 5216, LCO
μ_r, mag/arcsec**2

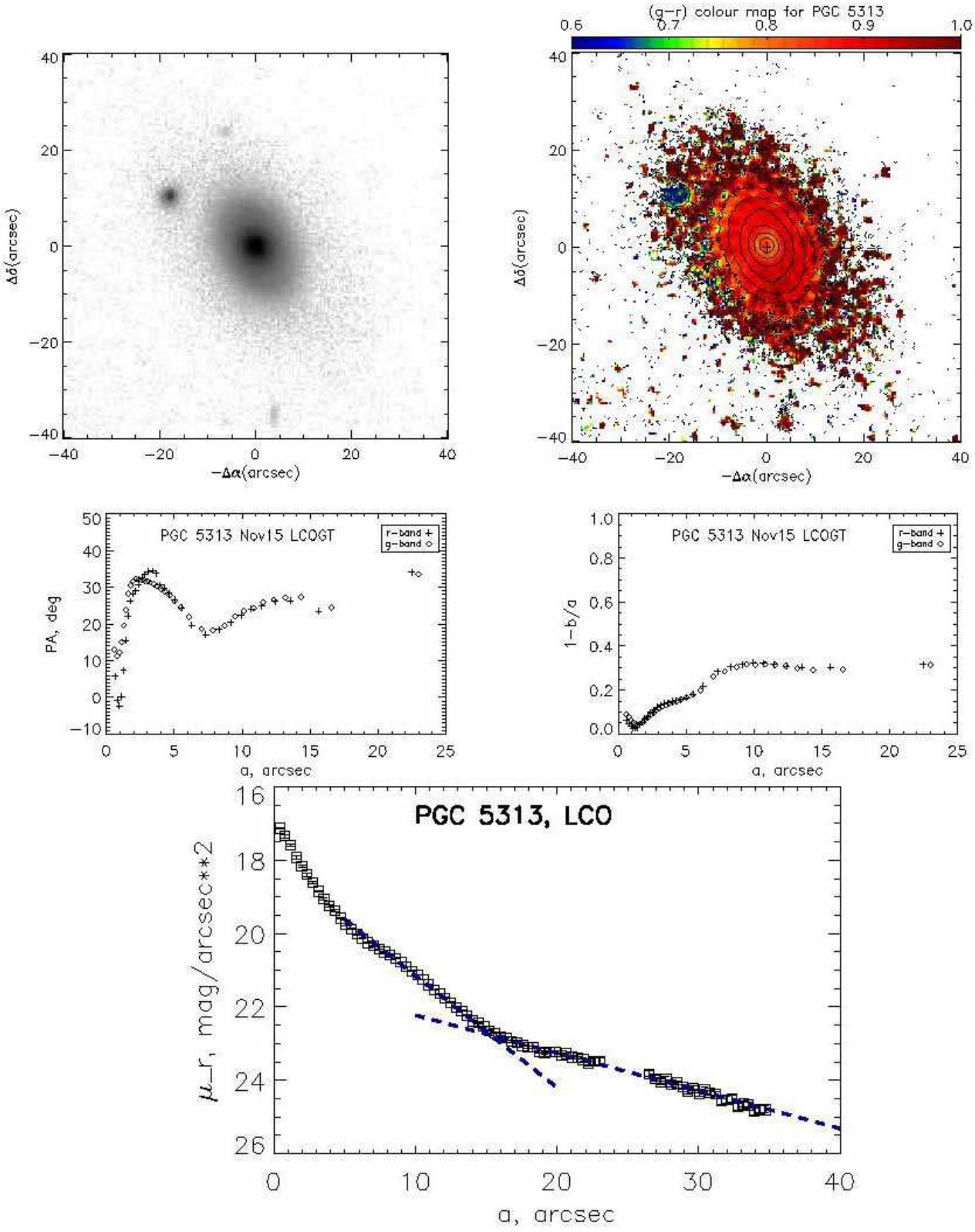
(g−r) colour map for PGC 5313
0.6
0.7
0.8
0.9
1.0
Δδ(arcsec)
−Δα(arcsec)
PGC 5313 Nov15 LCOGT
r−band +
g−band ◇
PA, deg
a, arcsec
1−b/a
PGC 5313, LCO
μ_r, mag/arcsec**2
a, arcsec

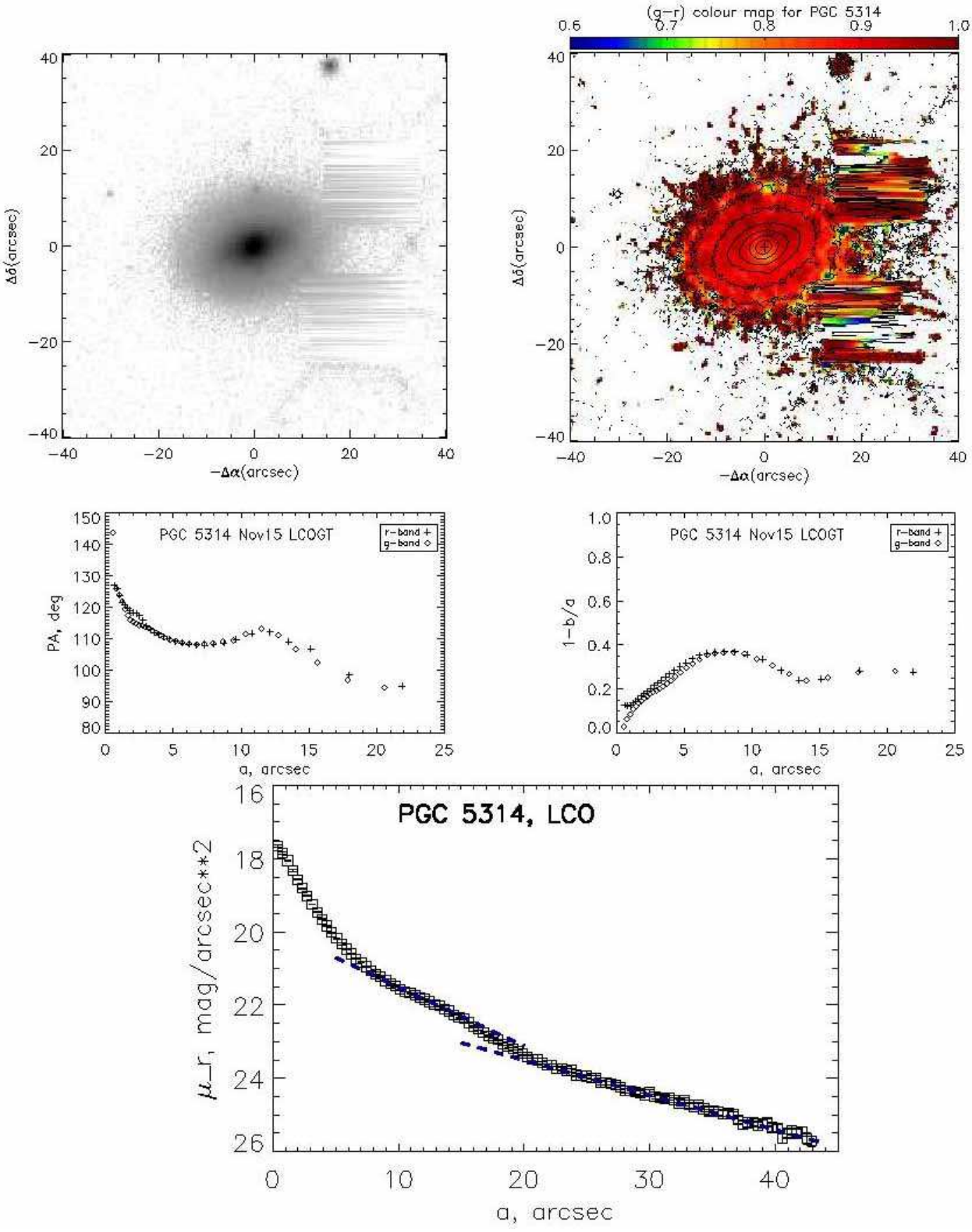
(g−r) colour map for PGC 5314
0.6
0.7
0.8
0.9
1.0
Δδ(arcsec)
−Δα(arcsec)
PGC 5314 Nov15 LCOGT
r−band +
g−band ◇
PA, deg
a, arcsec
1−b/a
PGC 5314, LCO
μ_r, mag/arcsec**2

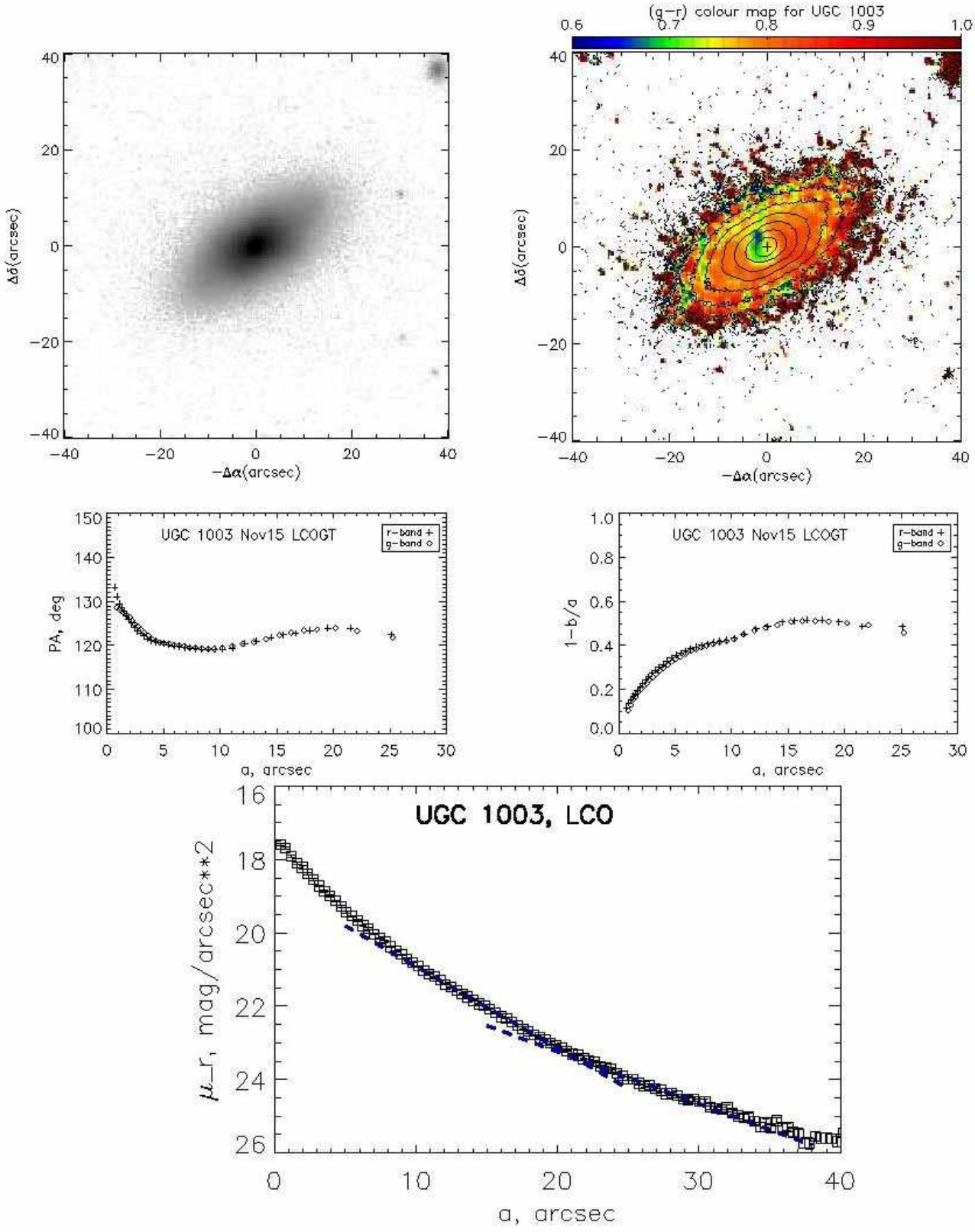
(g−r) colour map for UGC 1003
0.6
0.7
0.8
0.9
1.0
Δδ(arcsec)
−Δα(arcsec)
UGC 1003 Nov15 LCOGT
r−band +
g−band ◇
PA, deg
a, arcsec
1−b/a
UGC 1003, LCO
μ_r, mag/arcsec**2

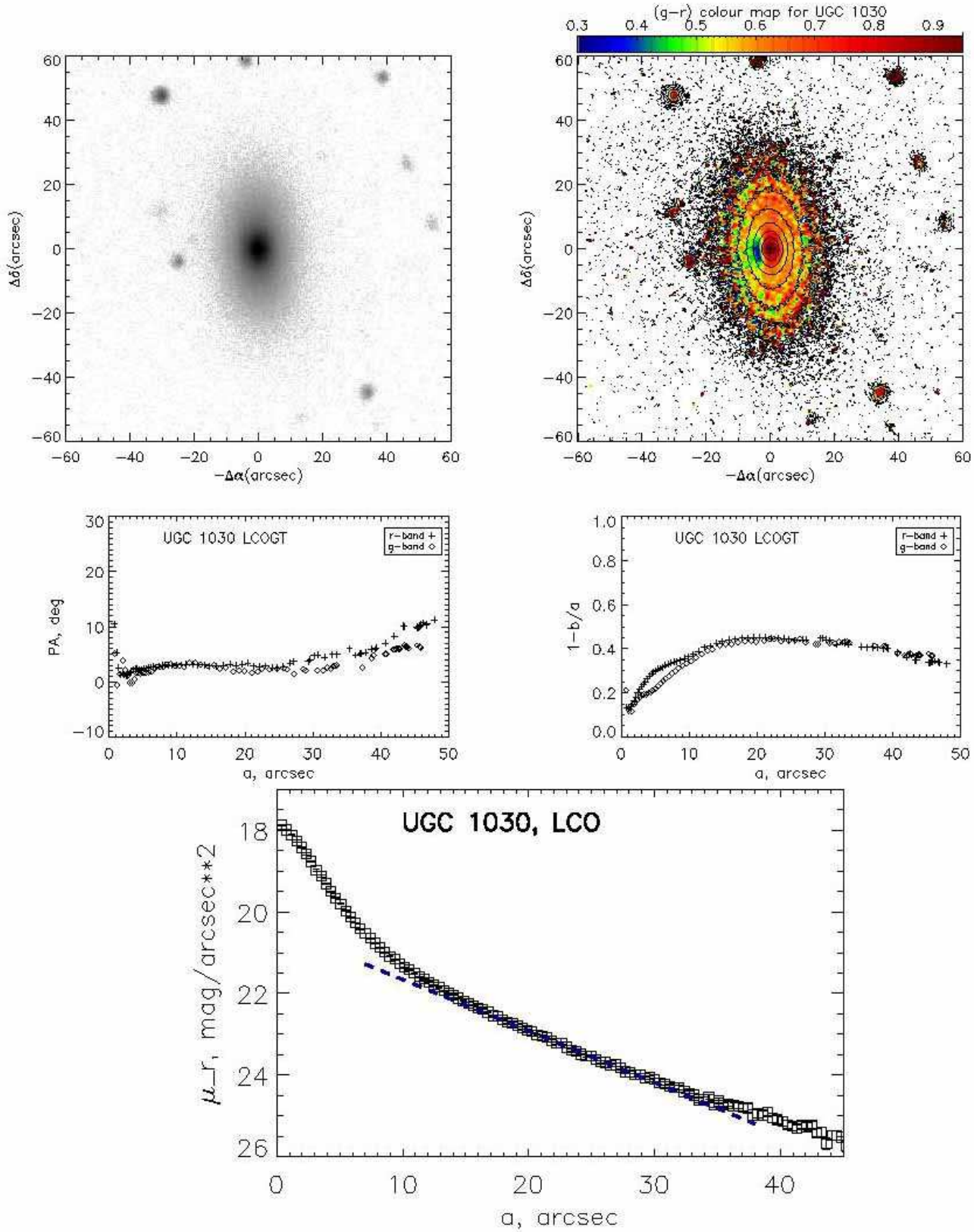
(g−r) colour map for UGC 1030
0.3 0.4 0.5 0.6 0.7 0.8 0.9
Δδ(arcsec)
−Δα(arcsec)
UGC 1030 LCOGT
r−band +
g−band ◇
PA, deg
a, arcsec
1−b/a
UGC 1030, LCO
μ_r, mag/arcsec**2

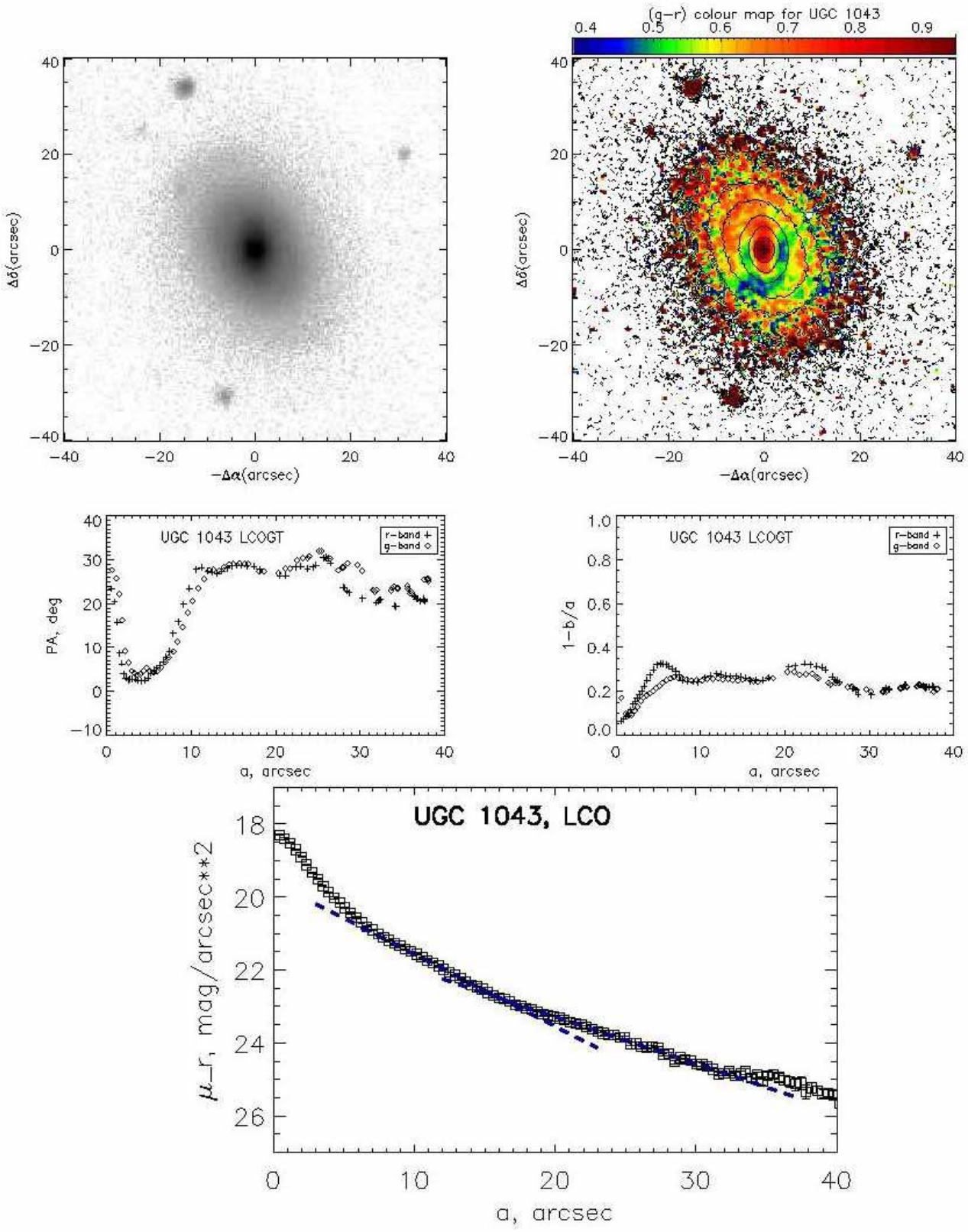
(g−r) colour map for UGC 1043
0.4
0.5
0.6
0.7
0.8
0.9
Δδ(arcsec)
−Δα(arcsec)
UGC 1043 LCOGT
r−band +
g−band ◇
PA, deg
a, arcsec
1−b/a
UGC 1043, LCO
μ_r, mag/arcsec**2

2 NGC 1550 group

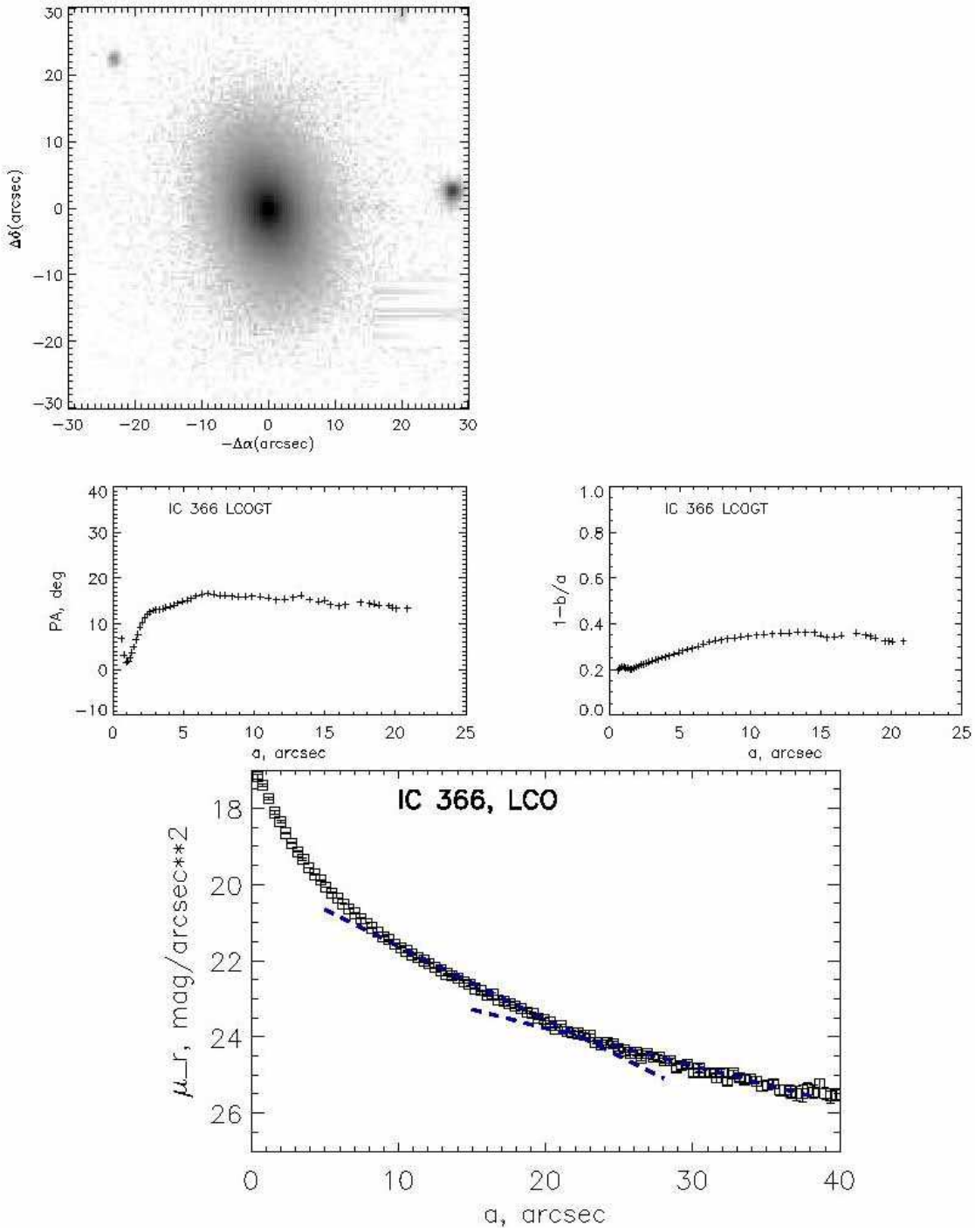

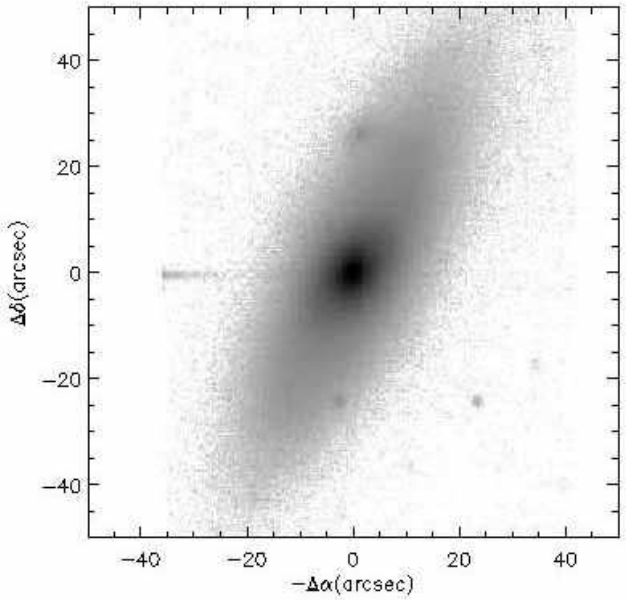
Δδ(arcsec)
−Δα(arcsec)

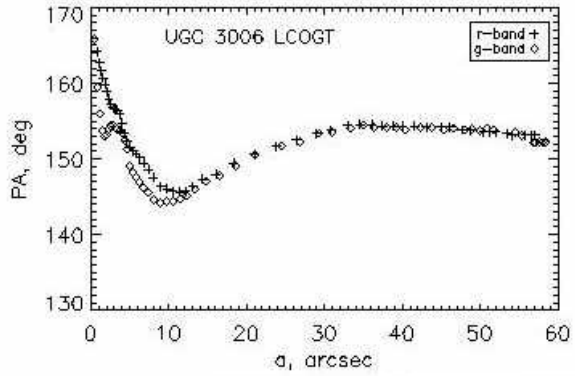
UGC 3006 LCOGT
r−band +
g−band ◇
PA, deg
a, arcsec

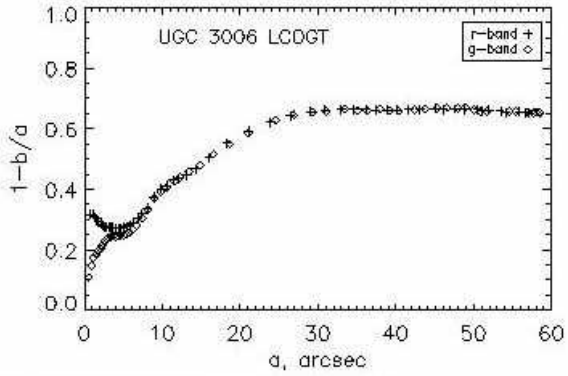
UGC 3006 LCOGT
r−band +
g−band ◇
1−b/a
a, arcsec

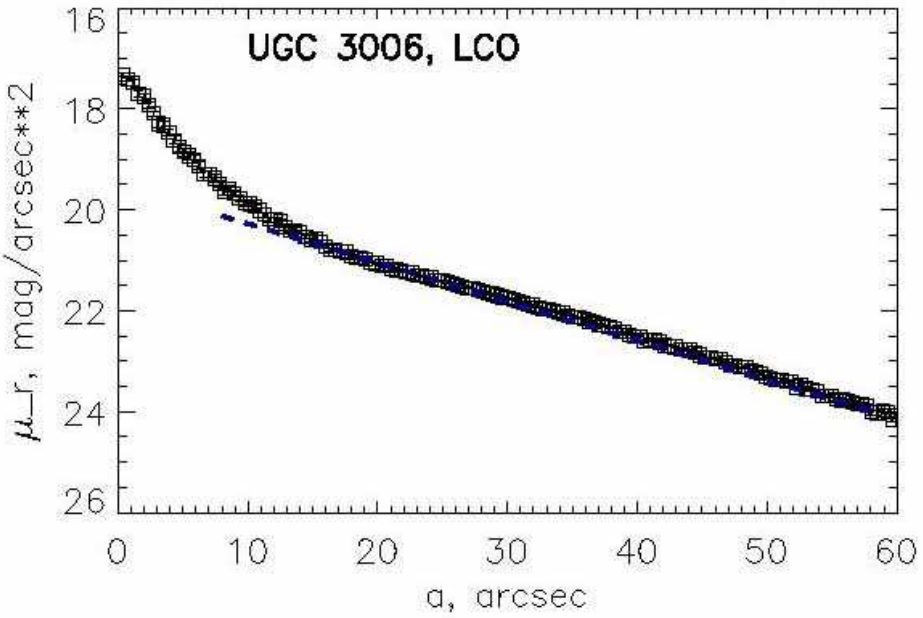
UGC 3006, LCO
μ_r, mag/arcsec**2
a, arcsec

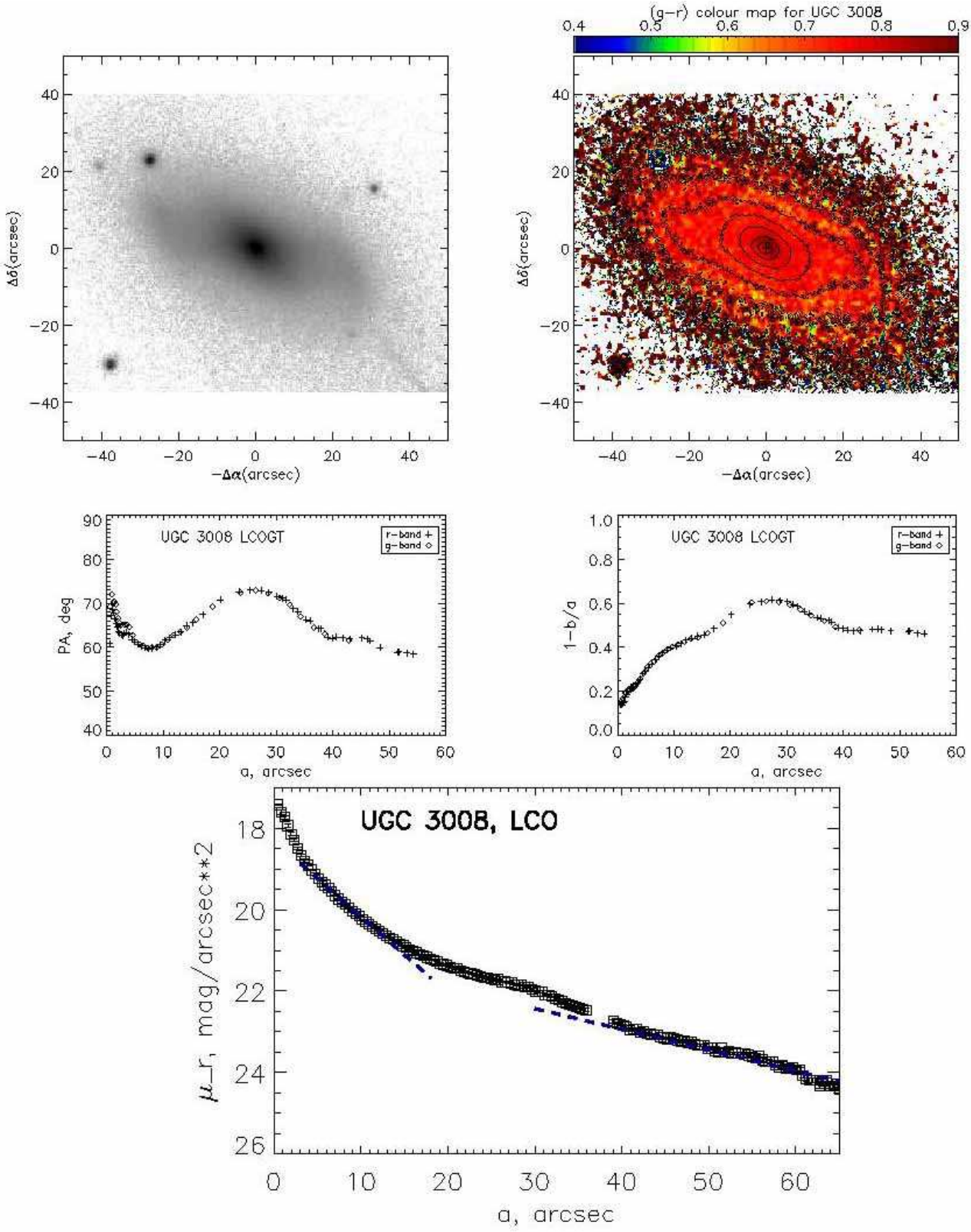
(g−r) colour map for UGC 3008
0.4
0.5
0.6
0.7
0.8
0.9
Δδ(arcsec)
−Δα(arcsec)
UGC 3008 LCOGT
r−band +
g−band ◇
PA, deg
a, arcsec
1−b/a
UGC 3008, LCO
μ_r, mag/arcsec**2

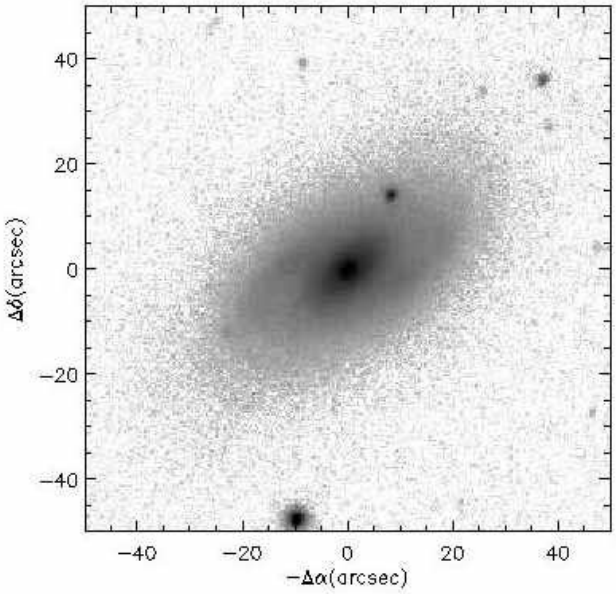
40
20
0
−20
−40
Δδ(arcsec)
−40
−20
0
20
40
−Δα(arcsec)

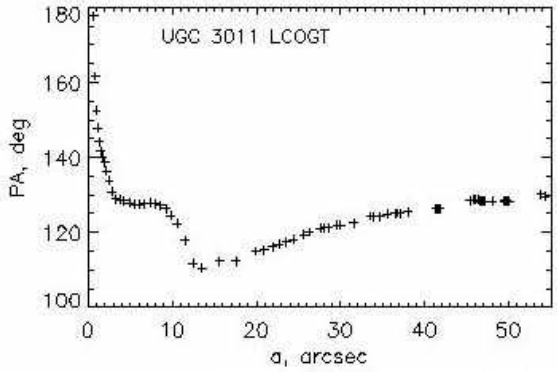
UGC 3011 LCOGT
180
160
140
120
100
PA, deg
0
10
20
30
40
50
a, arcsec

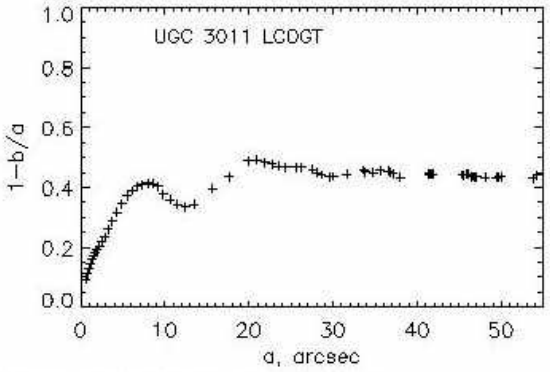
UGC 3011 LCOGT
1.0
0.8
0.6
0.4
0.2
0.0
1−b/a
0
10
20
30
40
50
a, arcsec

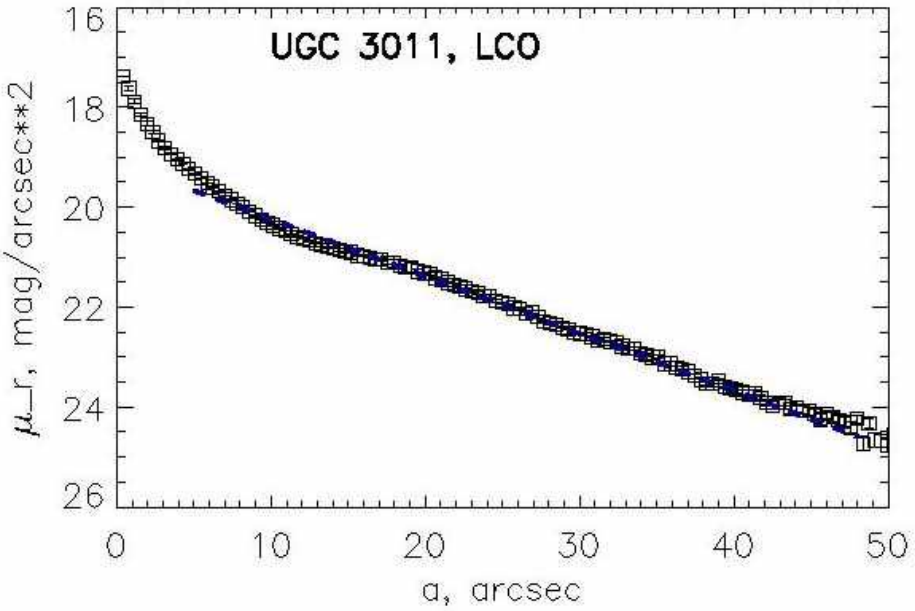
UGC 3011, LCO
16
18
20
22
24
26
μ_r, mag/arcsec**2
0
10
20
30
40
50
a, arcsec

3 Fornax

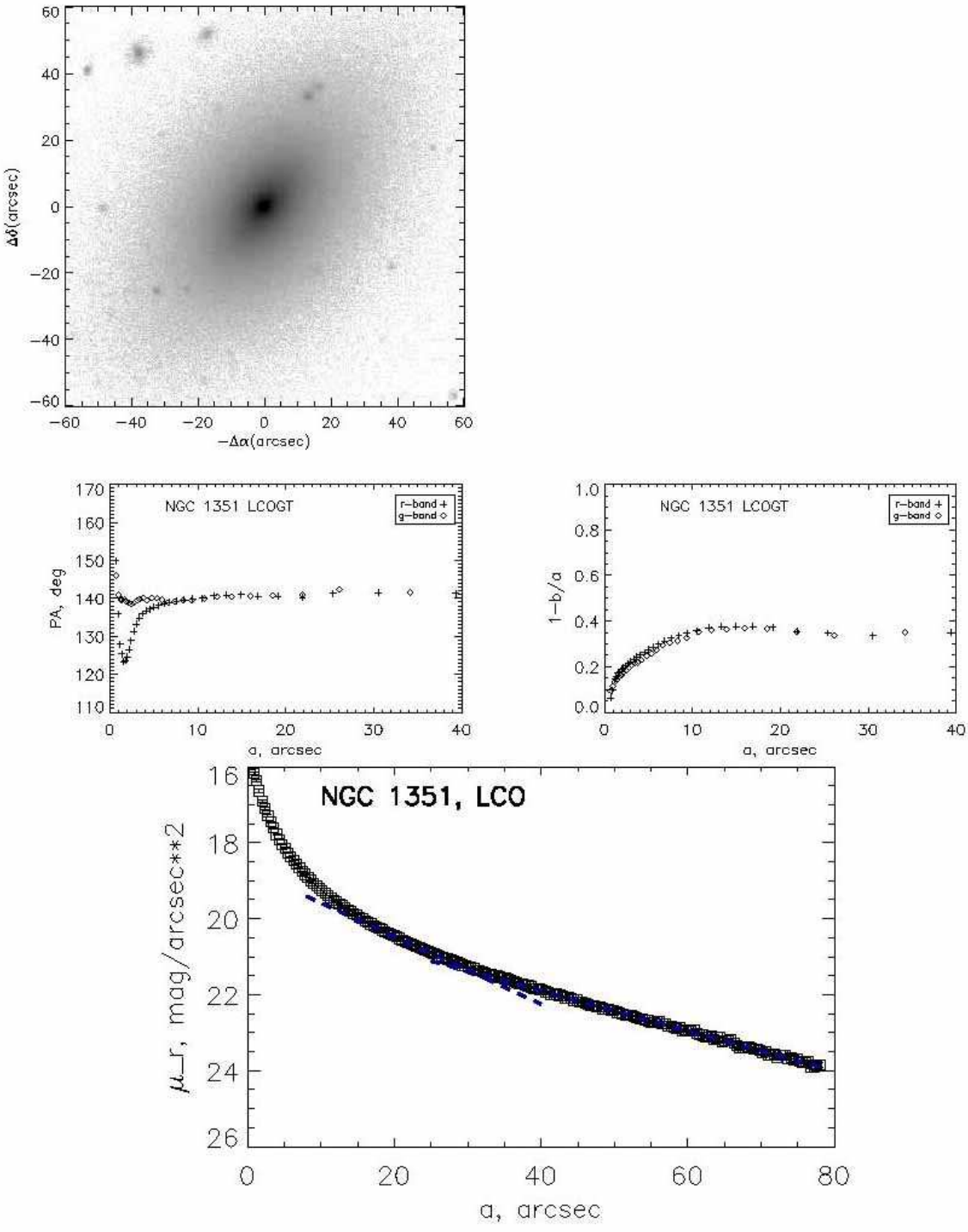
Δδ(arcsec)
−Δα(arcsec)
NGC 1351 LCOGT
r−band +
g−band ◇
PA, deg
a, arcsec
1−b/a
NGC 1351, LCO
μ_r, mag/arcsec**2

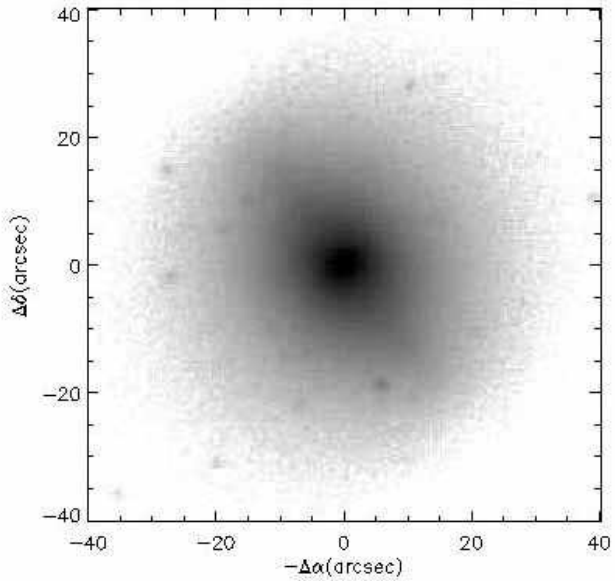
Δδ(arcsec)
−Δα(arcsec)

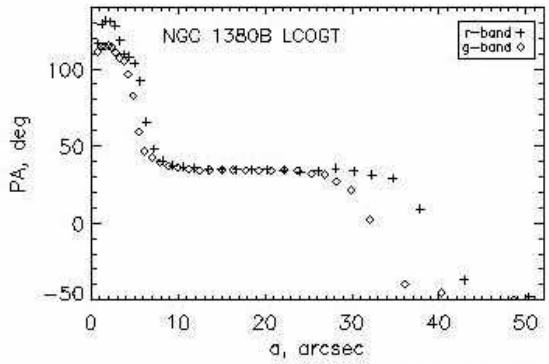
NGC 1380B LCOGT
r−band +
g−band ◇
PA, deg
a, arcsec

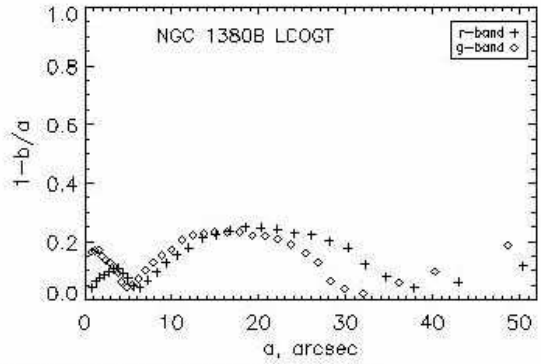
NGC 1380B LCOGT
r−band +
g−band ◇
1−b/a
a, arcsec

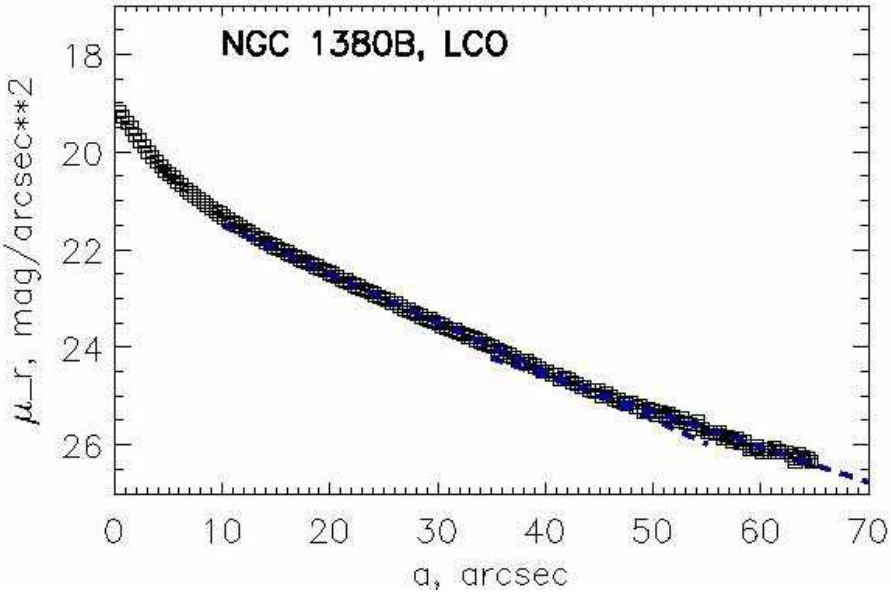
NGC 1380B, LCO
μ_r, mag/arcsec**2
a, arcsec

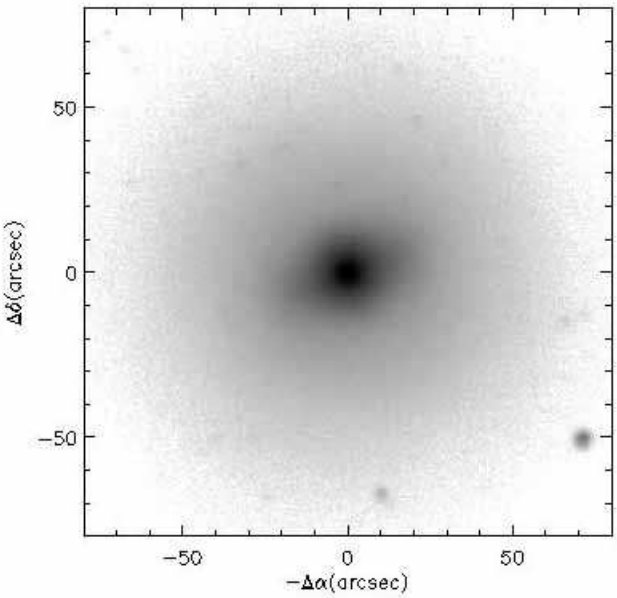
50
0
−50
Δδ(arcsec)
−50
0
50
−Δα(arcsec)

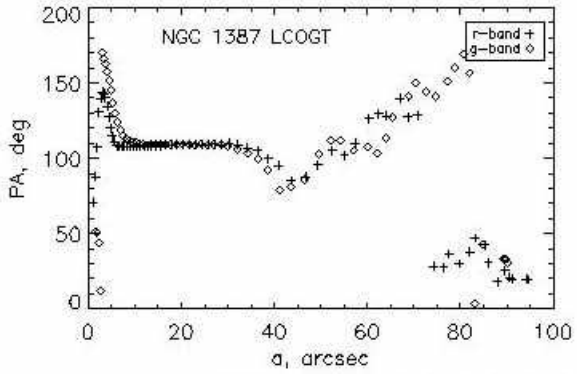
NGC 1387 LCOGT
r−band +
g−band ◇
PA, deg
200
150
100
50
0
0
20
40
60
80
100
a, arcsec

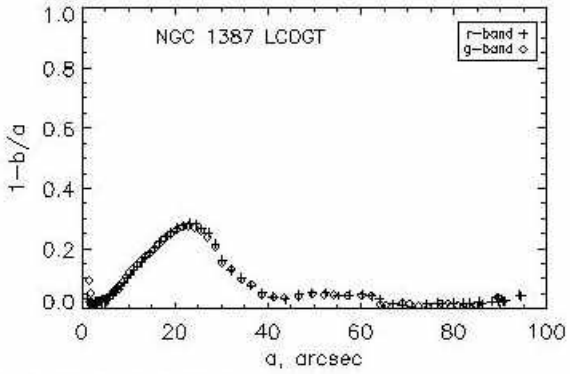
NGC 1387 LCOGT
r−band +
g−band ◇
1−b/a
1.0
0.8
0.6
0.4
0.2
0.0
0
20
40
60
80
100
a, arcsec

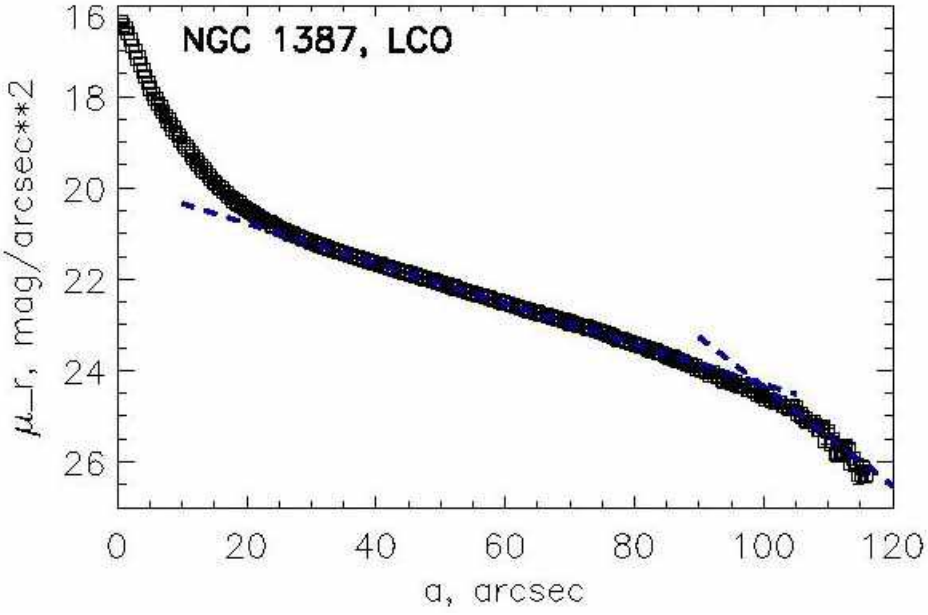
NGC 1387, LCO
μ_r, mag/arcsec**2
16
18
20
22
24
26
0
20
40
60
80
100
120
a, arcsec

4 Centaurus

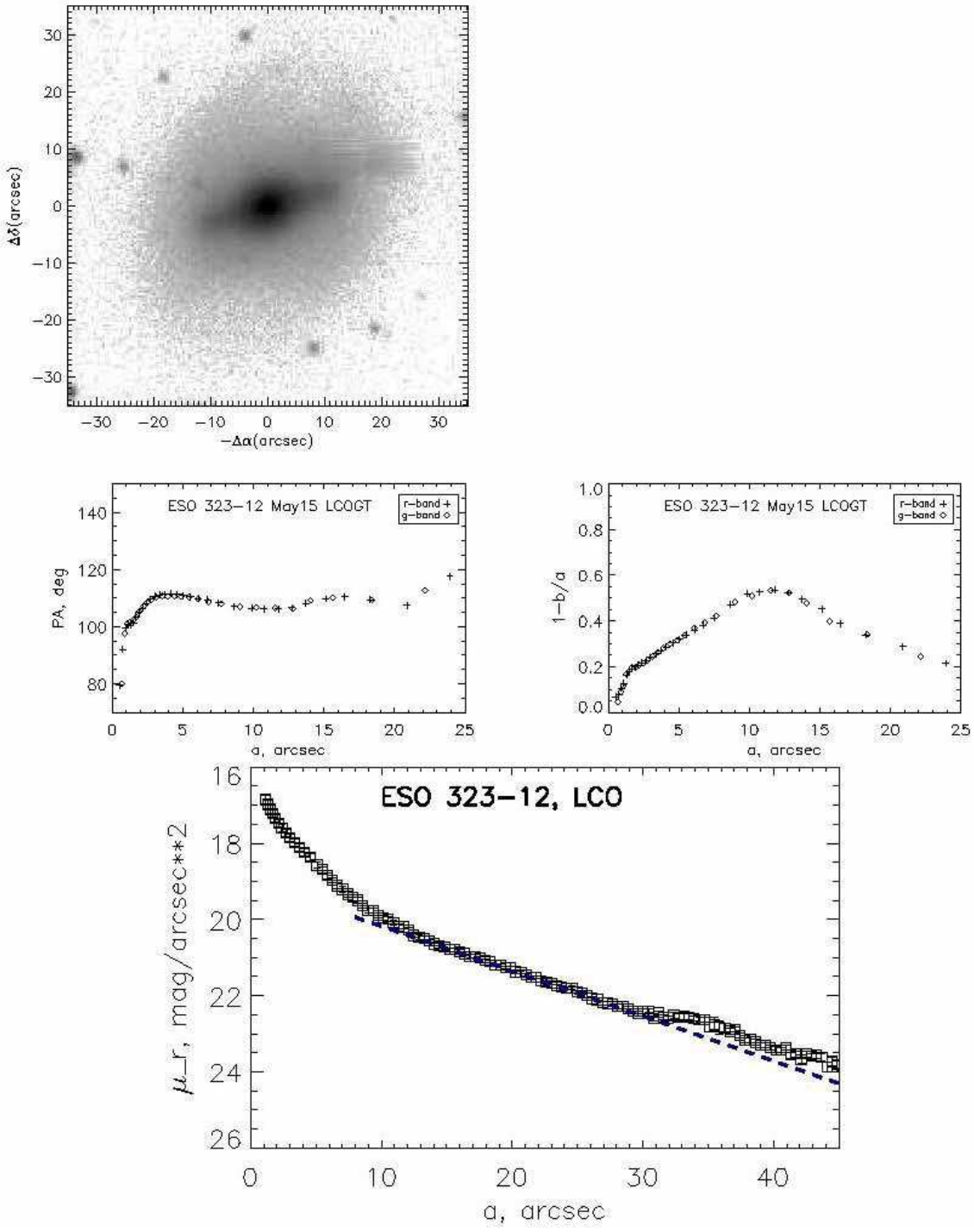
Δδ(arcsec)
−Δα(arcsec)
ESO 323−12 May15 LCOGT
r−band +
g−band ◇
PA, deg
a, arcsec
1−b/a
ESO 323−12, LCO
μ_r, mag/arcsec**2

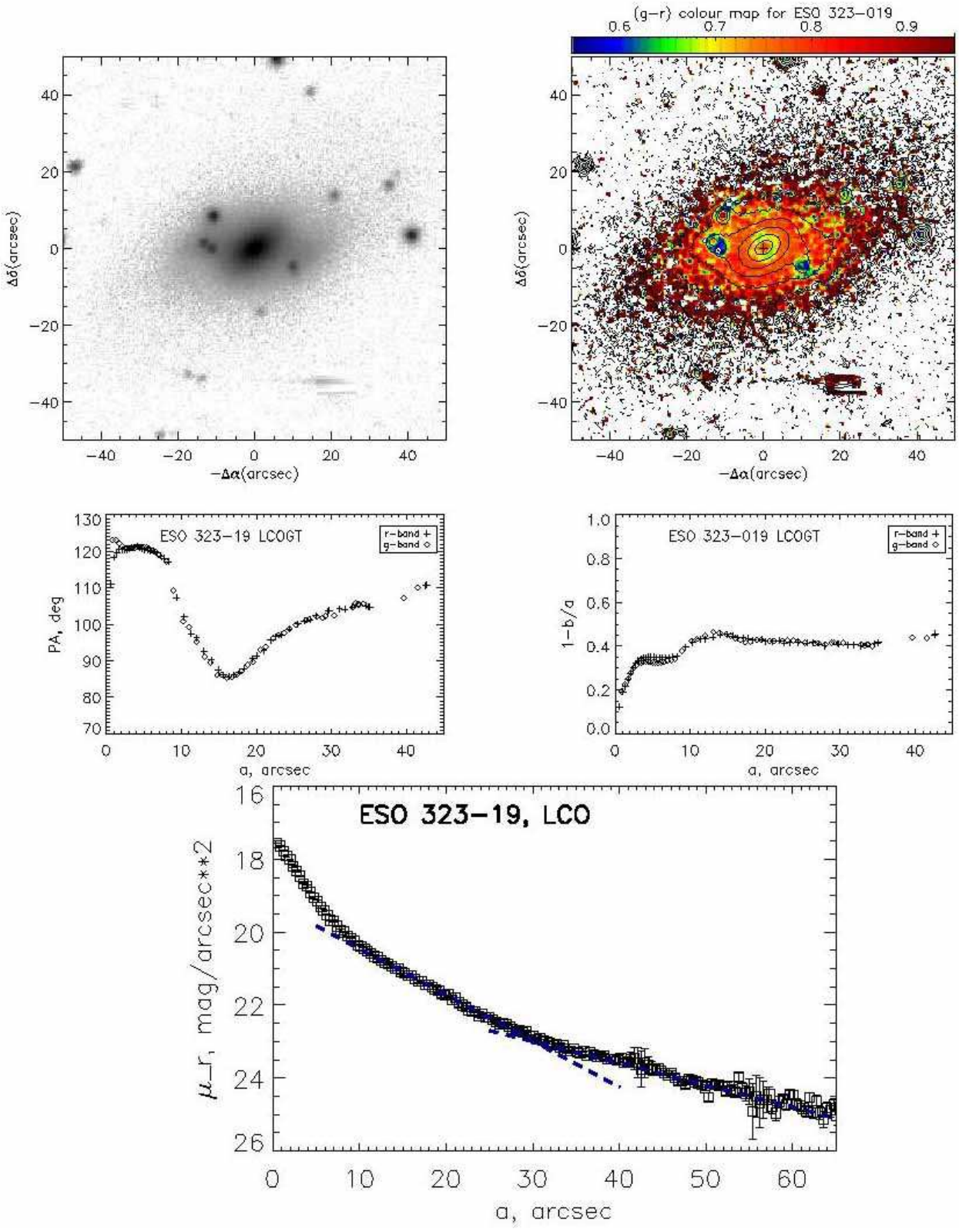
(g−r) colour map for ESO 323−019
0.6
0.7
0.8
0.9
Δδ(arcsec)
−Δα(arcsec)
ESO 323−19 LCOGT
r−band +
g−band ◇
PA, deg
a, arcsec
ESO 323−019 LCOGT
1−b/a
ESO 323−19, LCO
μ_r, mag/arcsec**2

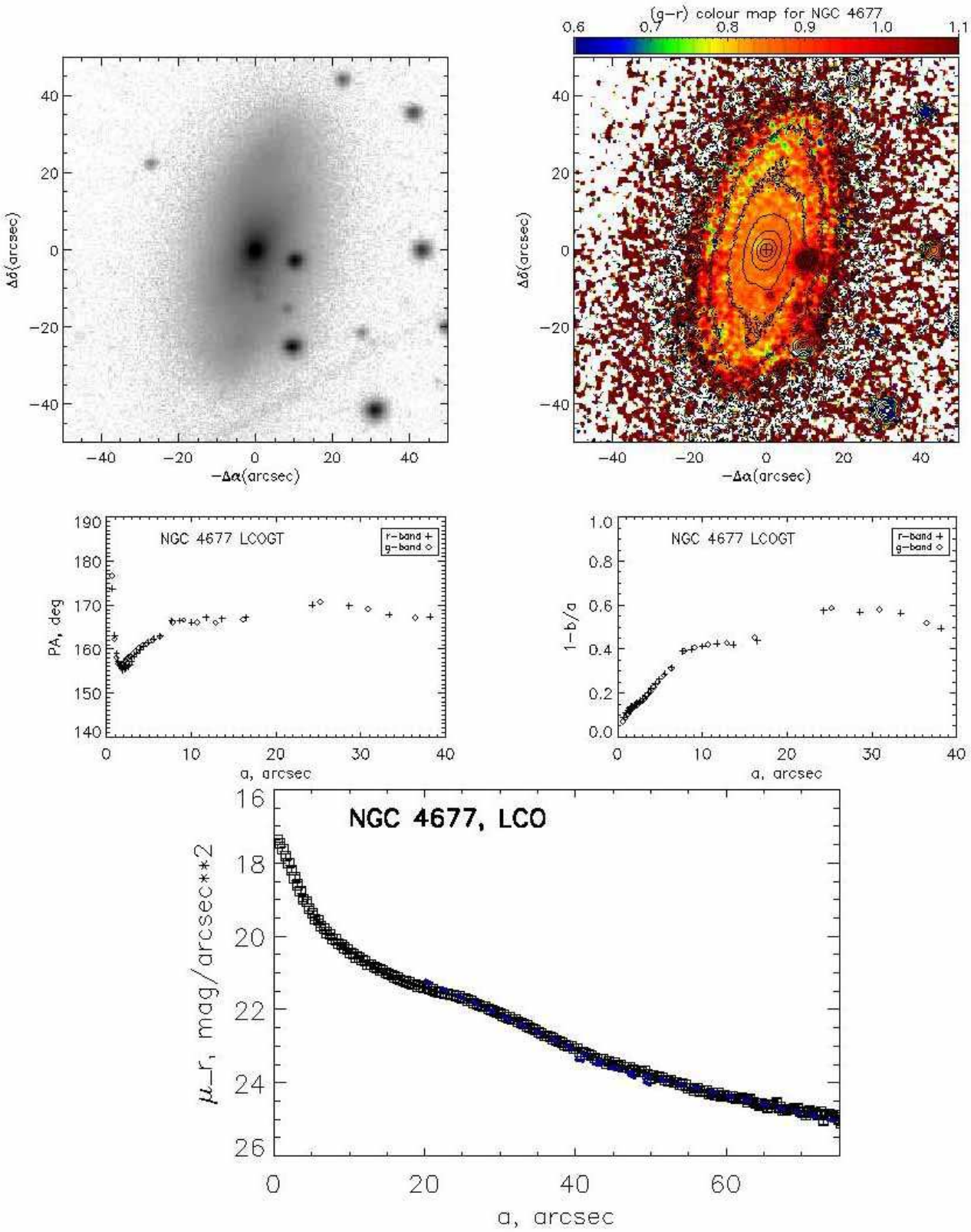
(g−r) colour map for NGC 4677
0.6
0.7
0.8
0.9
1.0
1.1
Δδ(arcsec)
−Δα(arcsec)
NGC 4677 LCOGT
r−band +
g−band ◇
PA, deg
1−b/a
a, arcsec
NGC 4677, LCO
μ_r, mag/arcsec**2
a, arcsec

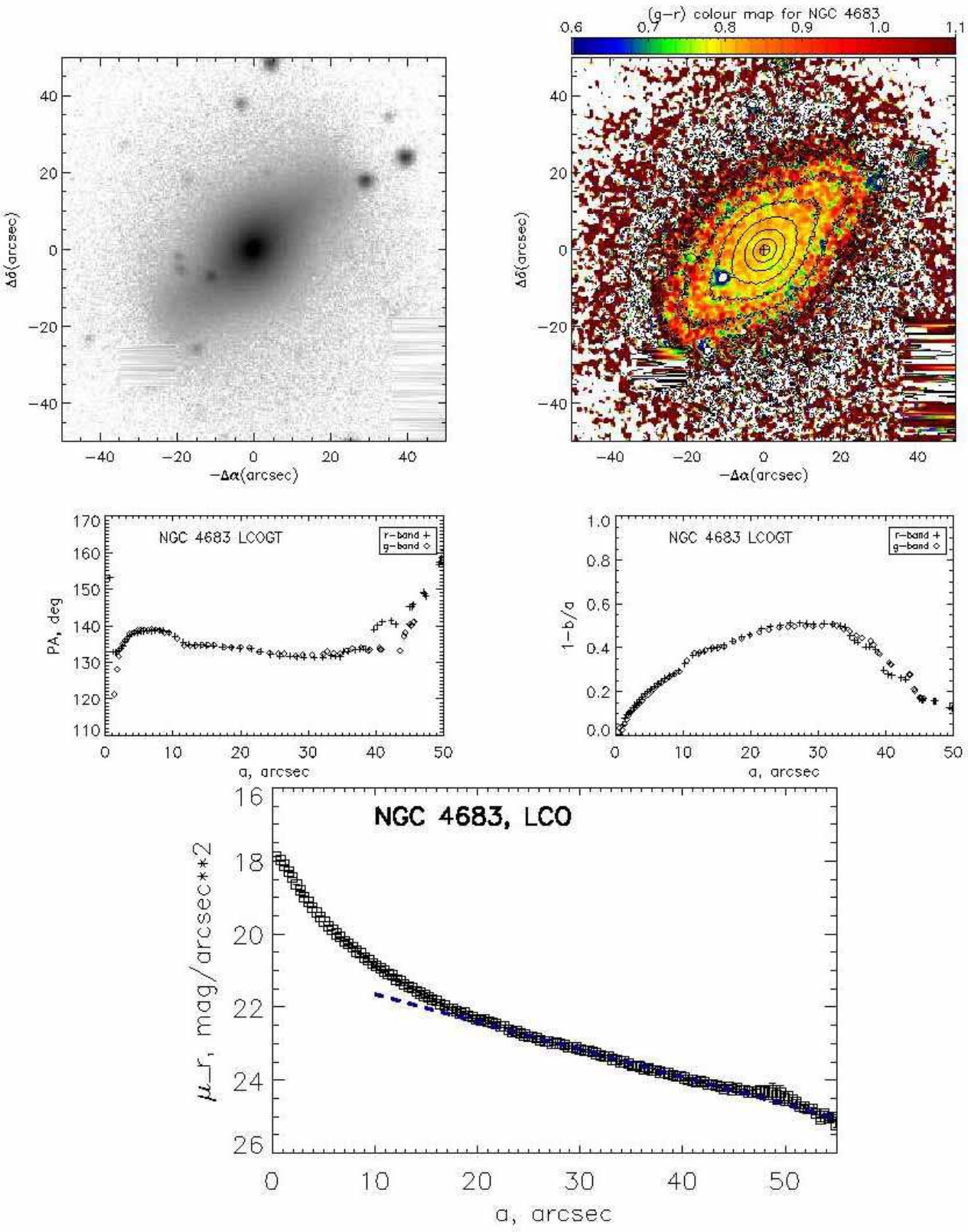
(g−r) colour map for NGC 4683
0.6
0.7
0.8
0.9
1.0
1.1
Δδ(arcsec)
−Δα(arcsec)
NGC 4683 LCOGT
r−band +
g−band ◇
PA, deg
1−b/a
a, arcsec
NGC 4683, LCO
μ_r, mag/arcsec**2

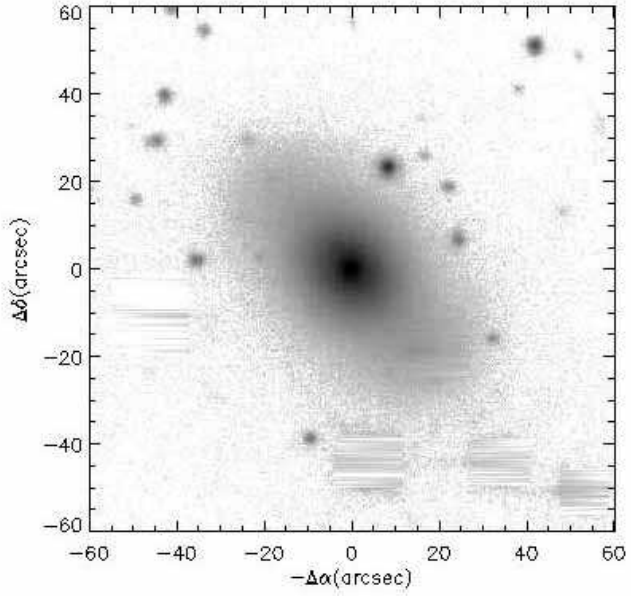
Δδ(arcsec)
−Δα(arcsec)

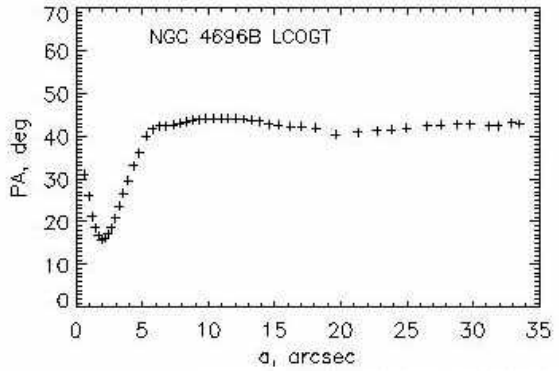
NGC 4696B LCOGT
PA, deg
a, arcsec

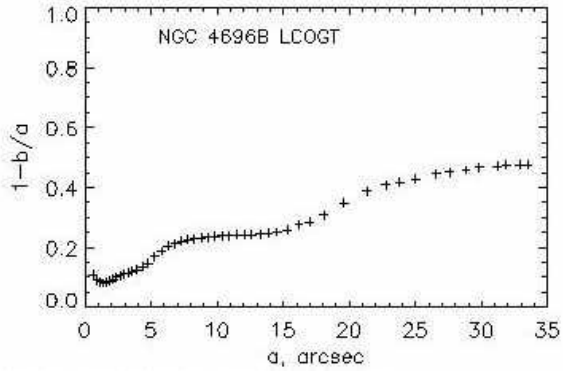
NGC 4696B LCOGT
1−b/a
a, arcsec

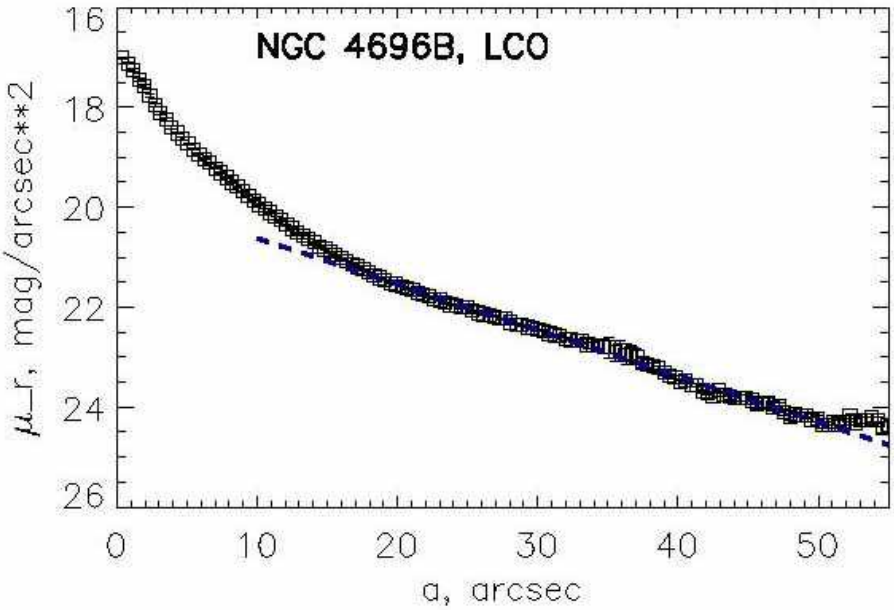
NGC 4696B, LCO
μ_r, mag/arcsec**2
a, arcsec

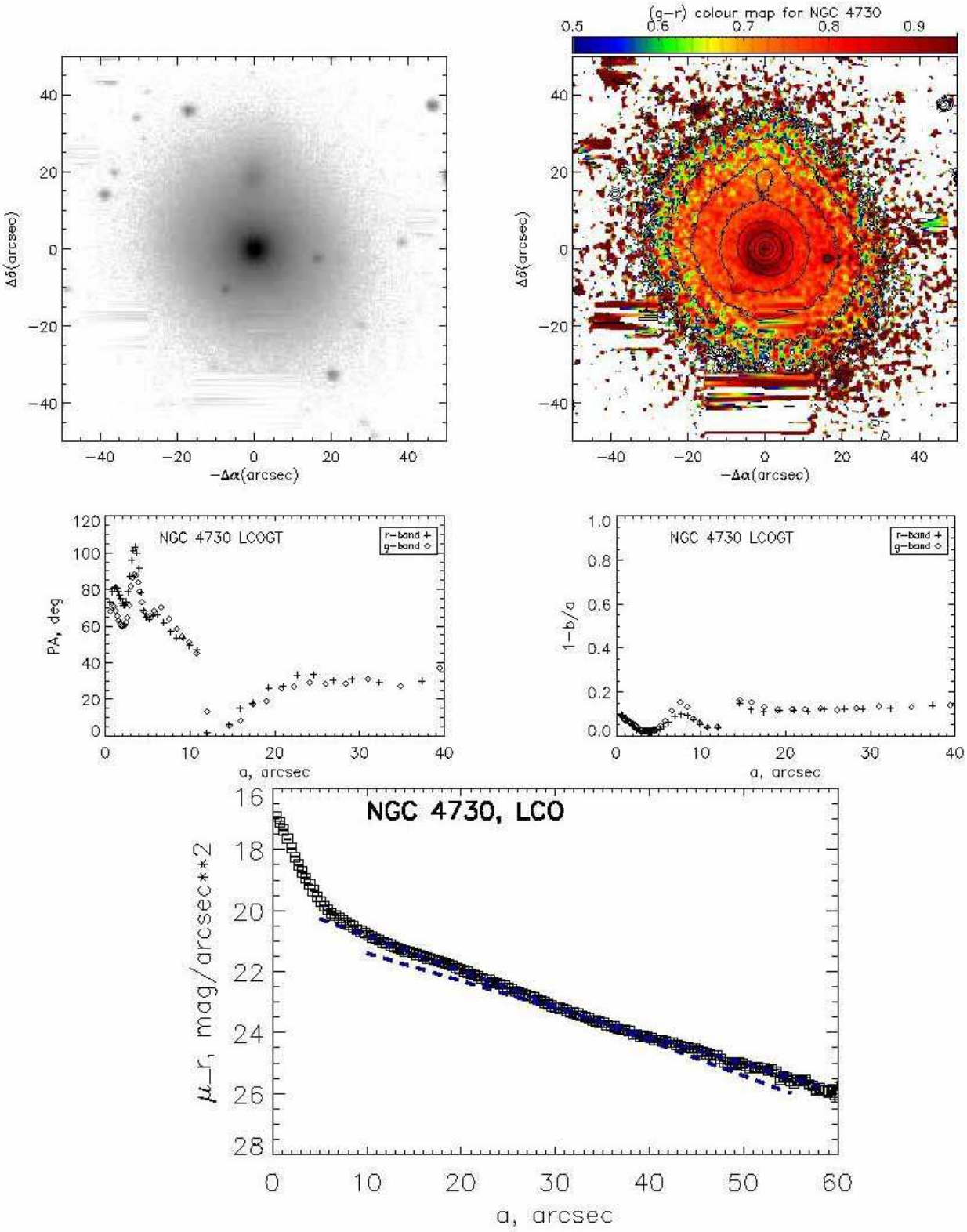
(g−r) colour map for NGC 4730
0.5
0.6
0.7
0.8
0.9
Δδ(arcsec)
−Δα(arcsec)
NGC 4730 LCOGT
r−band +
g−band ◇
PA, deg
a, arcsec
1−b/a
NGC 4730, LCO
μ_r, mag/arcsec**2

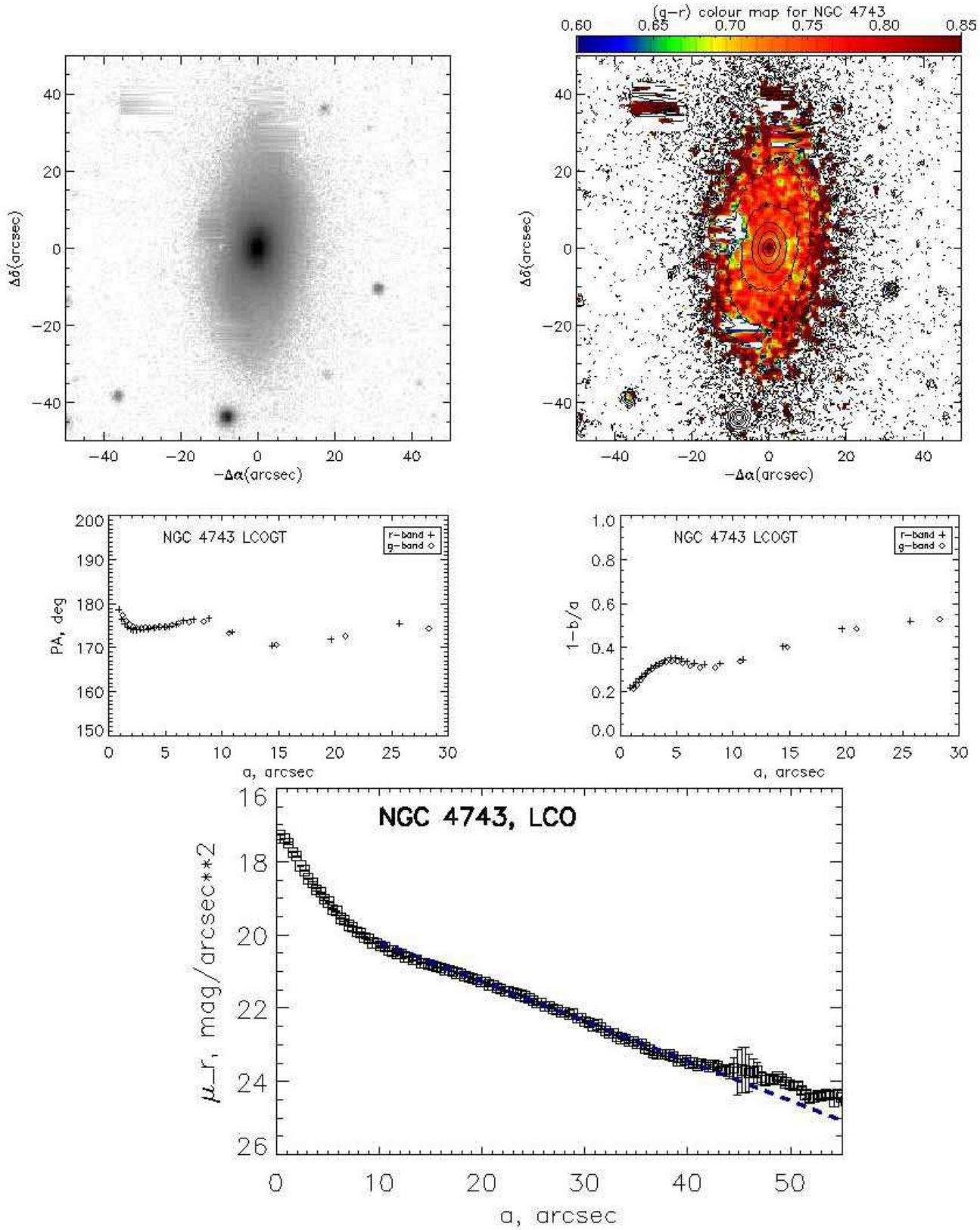
(g−r) colour map for NGC 4743
0.60
0.65
0.70
0.75
0.80
0.85
Δδ(arcsec)
−Δα(arcsec)
NGC 4743 LCOGT
r−band +
g−band ◇
PA, deg
a, arcsec
1−b/a
NGC 4743, LCO
μ_r, mag/arcsec**2

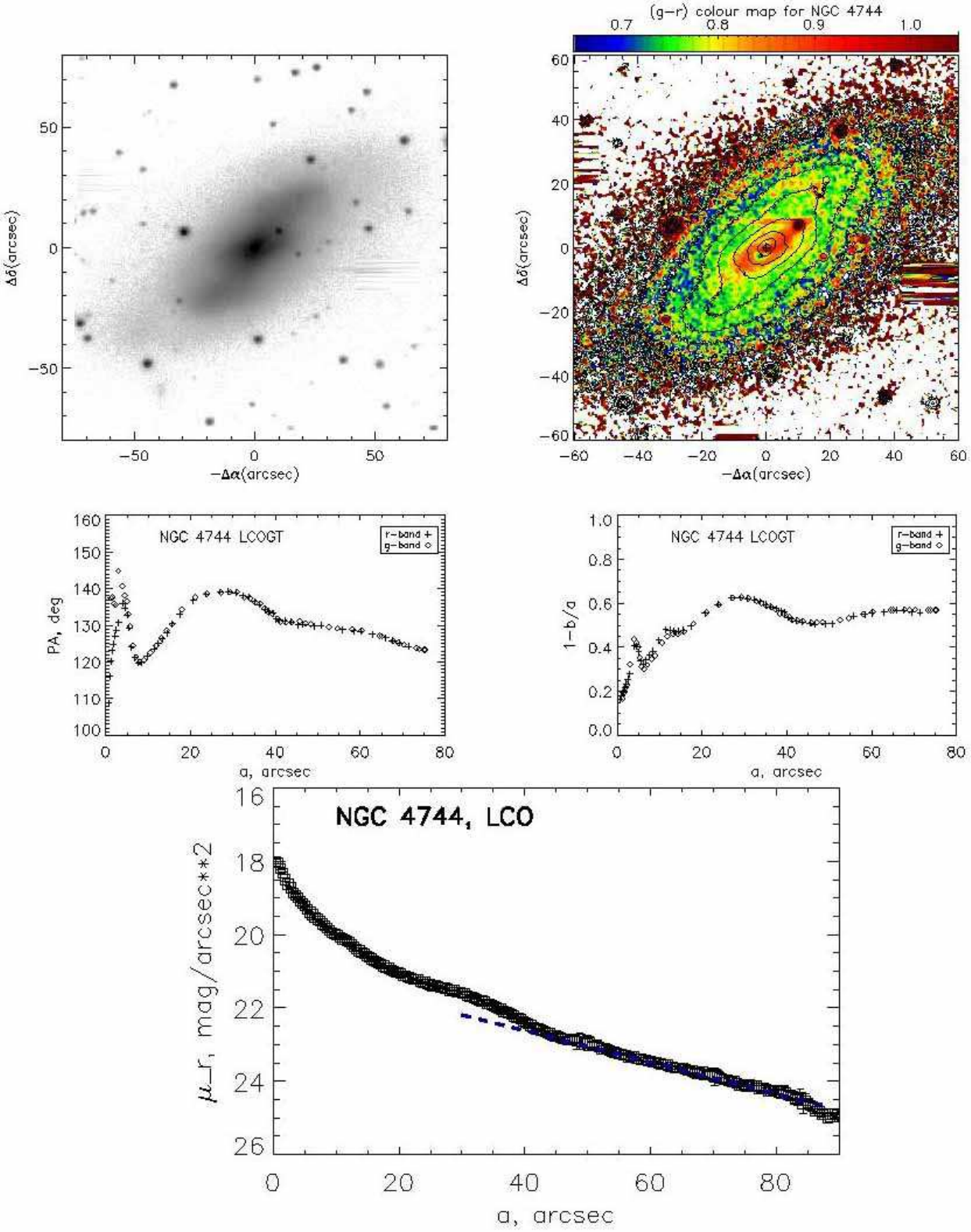
(g−r) colour map for NGC 4744
0.7
0.8
0.9
1.0
Δδ(arcsec)
−Δα(arcsec)
NGC 4744 LCOGT
r−band +
g−band ◇
PA, deg
a, arcsec
1−b/a
NGC 4744, LCO
μ_r, mag/arcsec**2

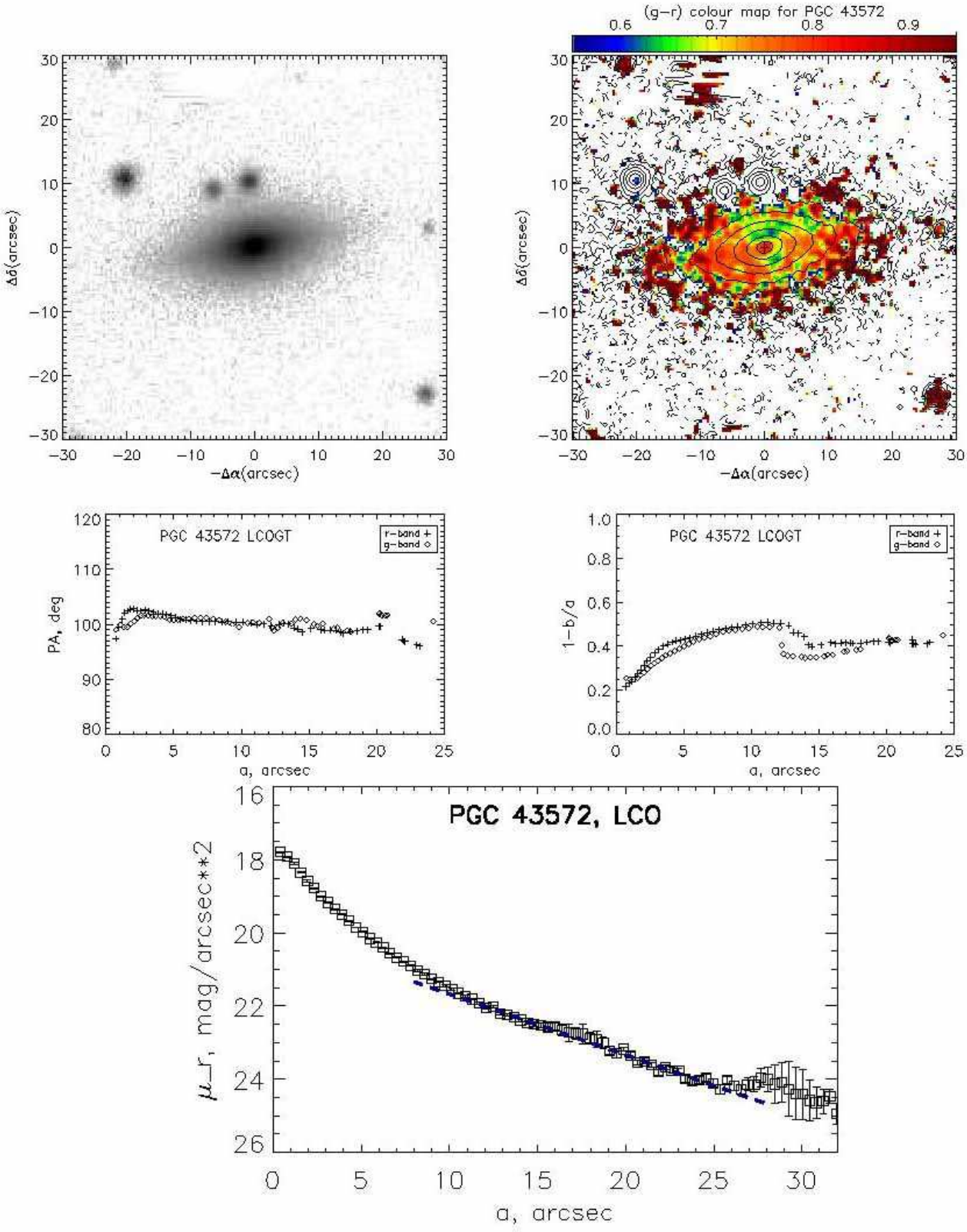
(g−r) colour map for PGC 43572
0.6
0.7
0.8
0.9
Δδ(arcsec)
−Δα(arcsec)
PGC 43572 LCOGT
r−band +
g−band ◇
PA, deg
a, arcsec
1−b/a
PGC 43572, LCO
μ_r, mag/arcsec**2

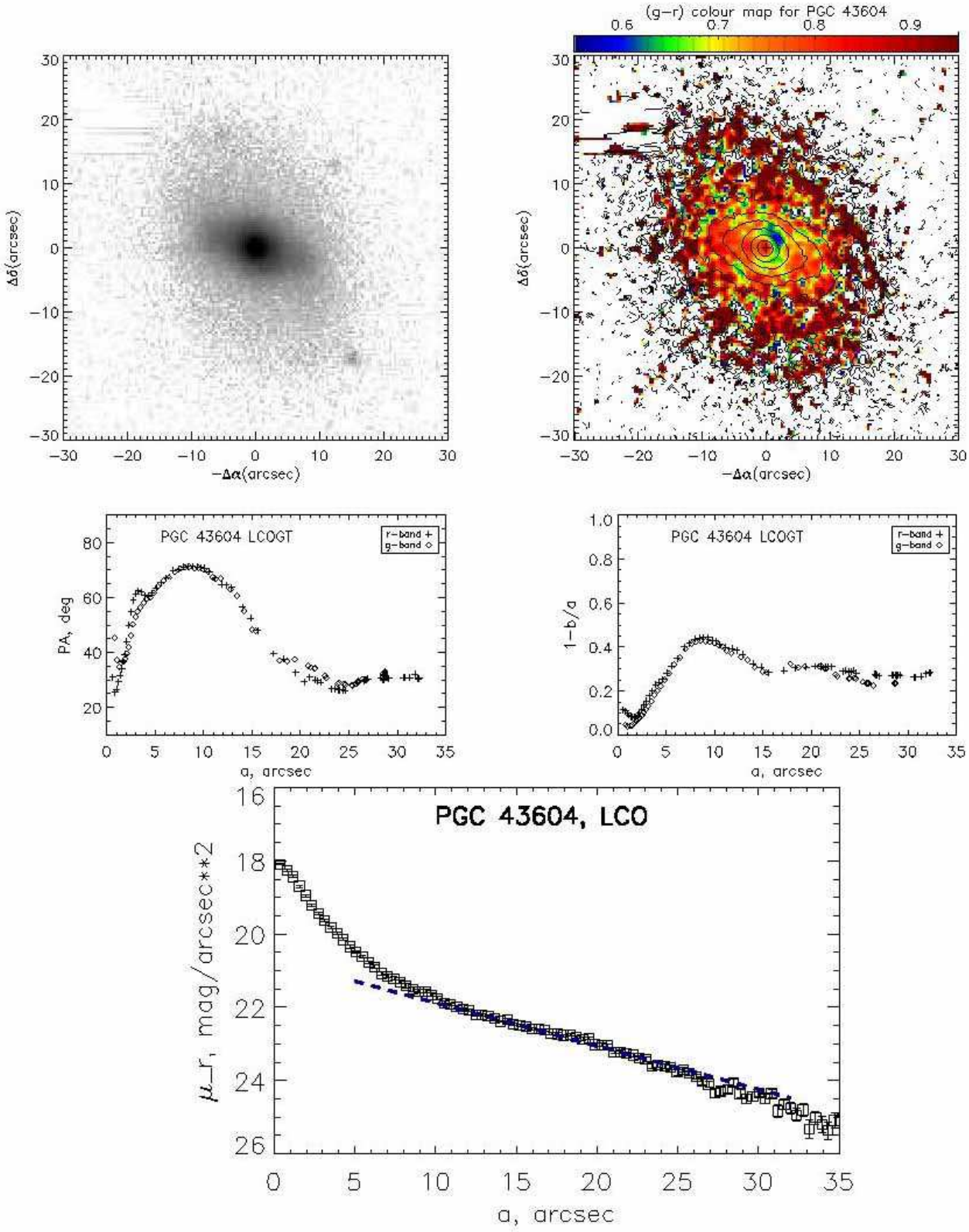
(g−r) colour map for PGC 43604
0.6
0.7
0.8
0.9
Δδ(arcsec)
−Δα(arcsec)
PGC 43604 LCOGT
r−band +
g−band ◇
PA, deg
1−b/a
a, arcsec
PGC 43604, LCO
μ_r, mag/arcsec**2

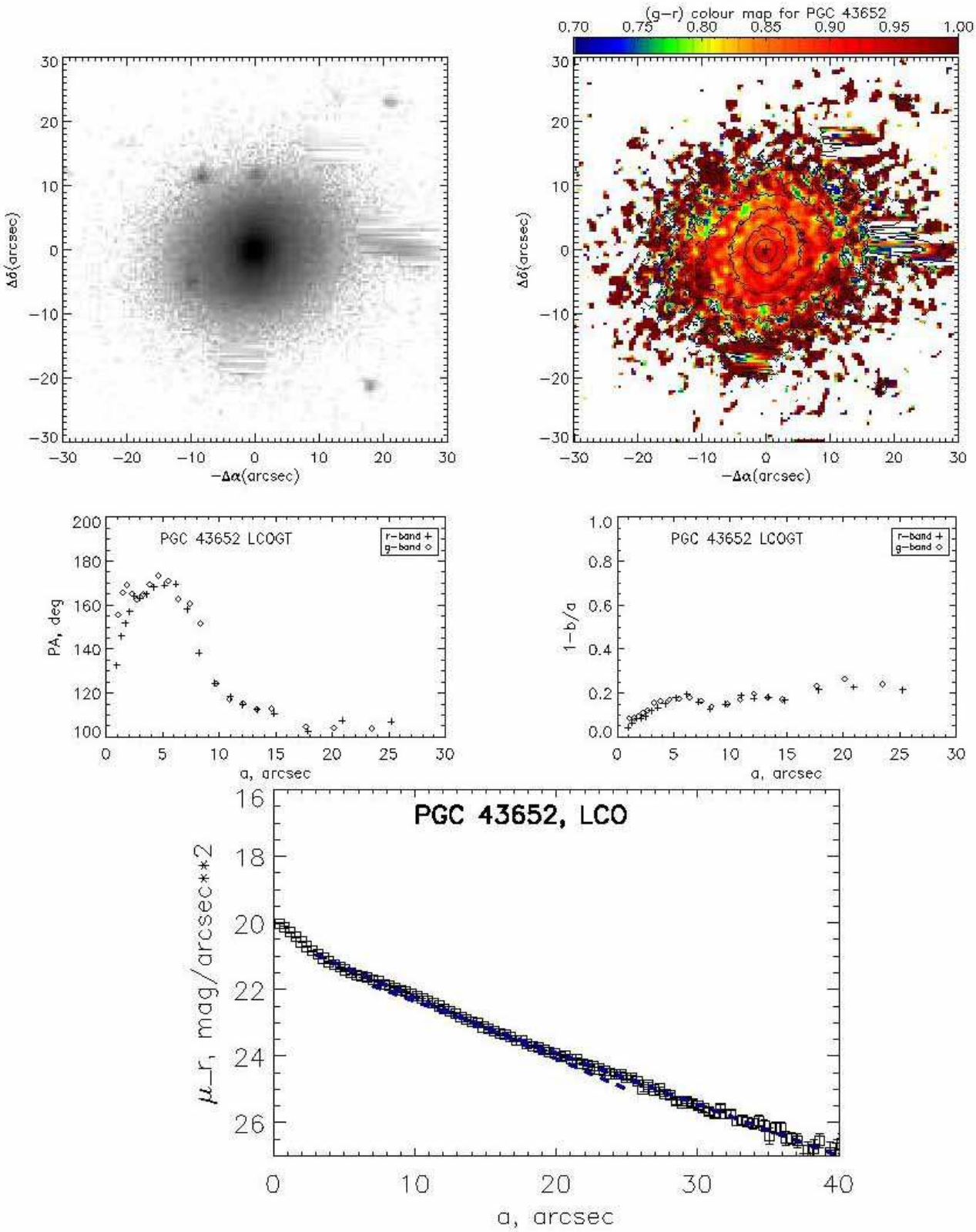
(g−r) colour map for PGC 43652
0.70 0.75 0.80 0.85 0.90 0.95 1.00
Δδ(arcsec)
−Δα(arcsec)
PGC 43652 LCOGT
r−band +
g−band ◇
PA, deg
a, arcsec
1−b/a
PGC 43652, LCO
μ_r, mag/arcsec**2

5 Hydra

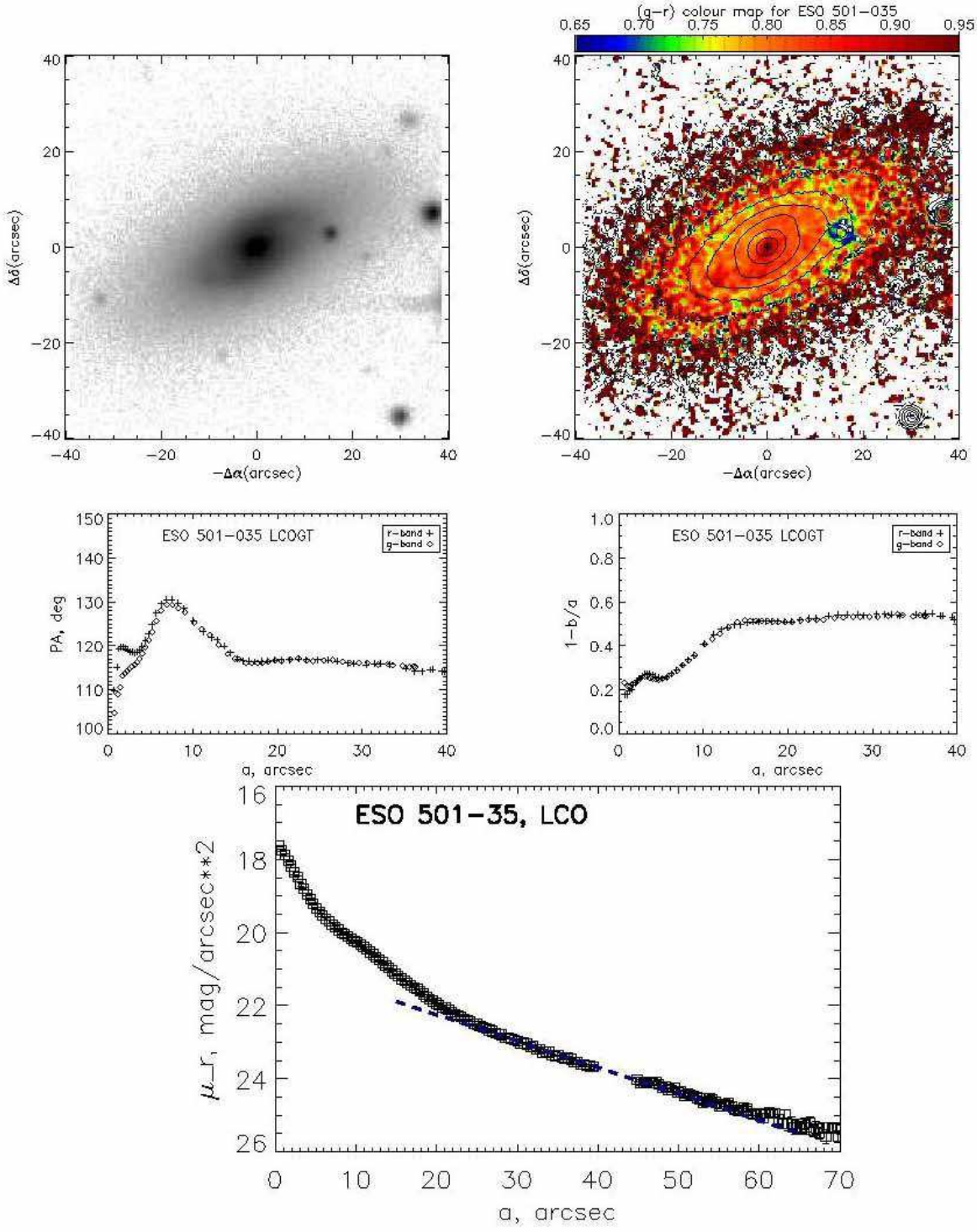
(g−r) colour map for ESO 501−035
0.65 0.70 0.75 0.80 0.85 0.90 0.95
Δδ(arcsec)
−Δα(arcsec)
ESO 501−035 LCOGT
r−band +
g−band ◇
PA, deg
a, arcsec
1−b/a
ESO 501−35, LCO
μ_r, mag/arcsec**2

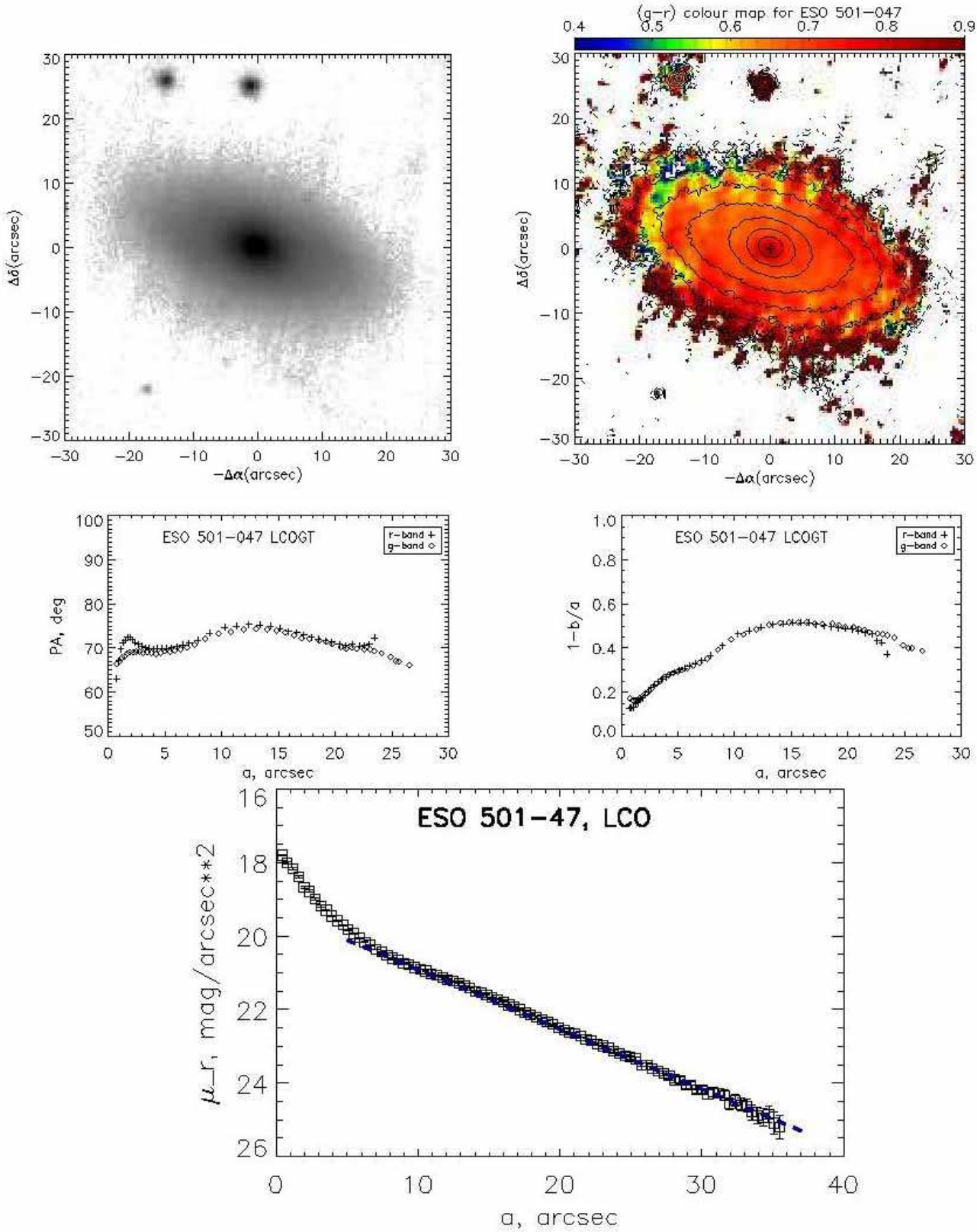
(g−r) colour map for ESO 501−047
0.4
0.5
0.6
0.7
0.8
0.9
Δδ(arcsec)
−Δα(arcsec)
ESO 501−047 LCOGT
r−band +
g−band ◇
PA, deg
a, arcsec
1−b/a
ESO 501−47, LCO
μ_r, mag/arcsec**2
a, arcsec

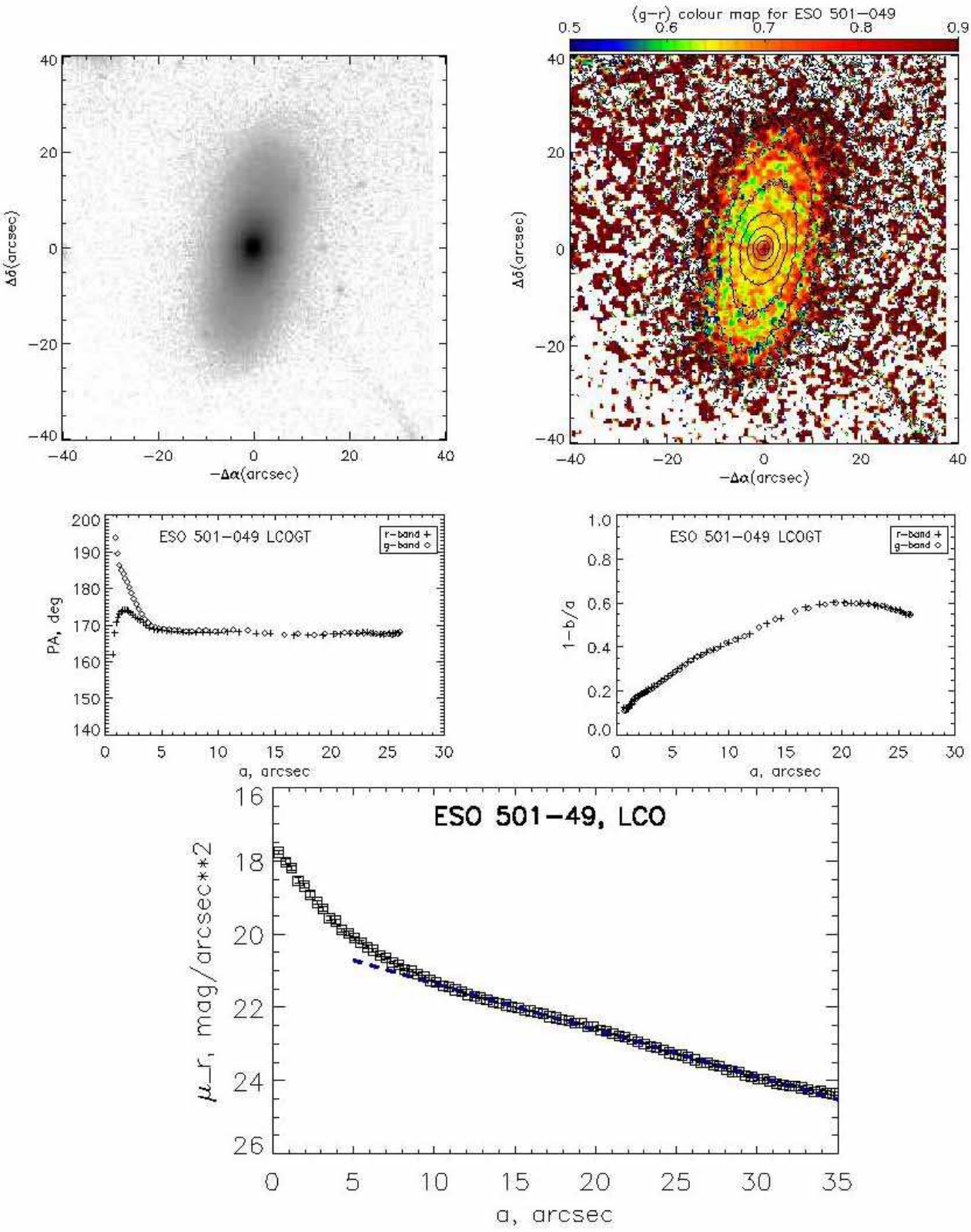
(g−r) colour map for ESO 501−049
0.5
0.6
0.7
0.8
0.9
Δδ(arcsec)
−Δα(arcsec)
ESO 501−049 LCOGT
r−band +
g−band ◇
PA, deg
a, arcsec
1−b/a
ESO 501−49, LCO
μ_r, mag/arcsec**2

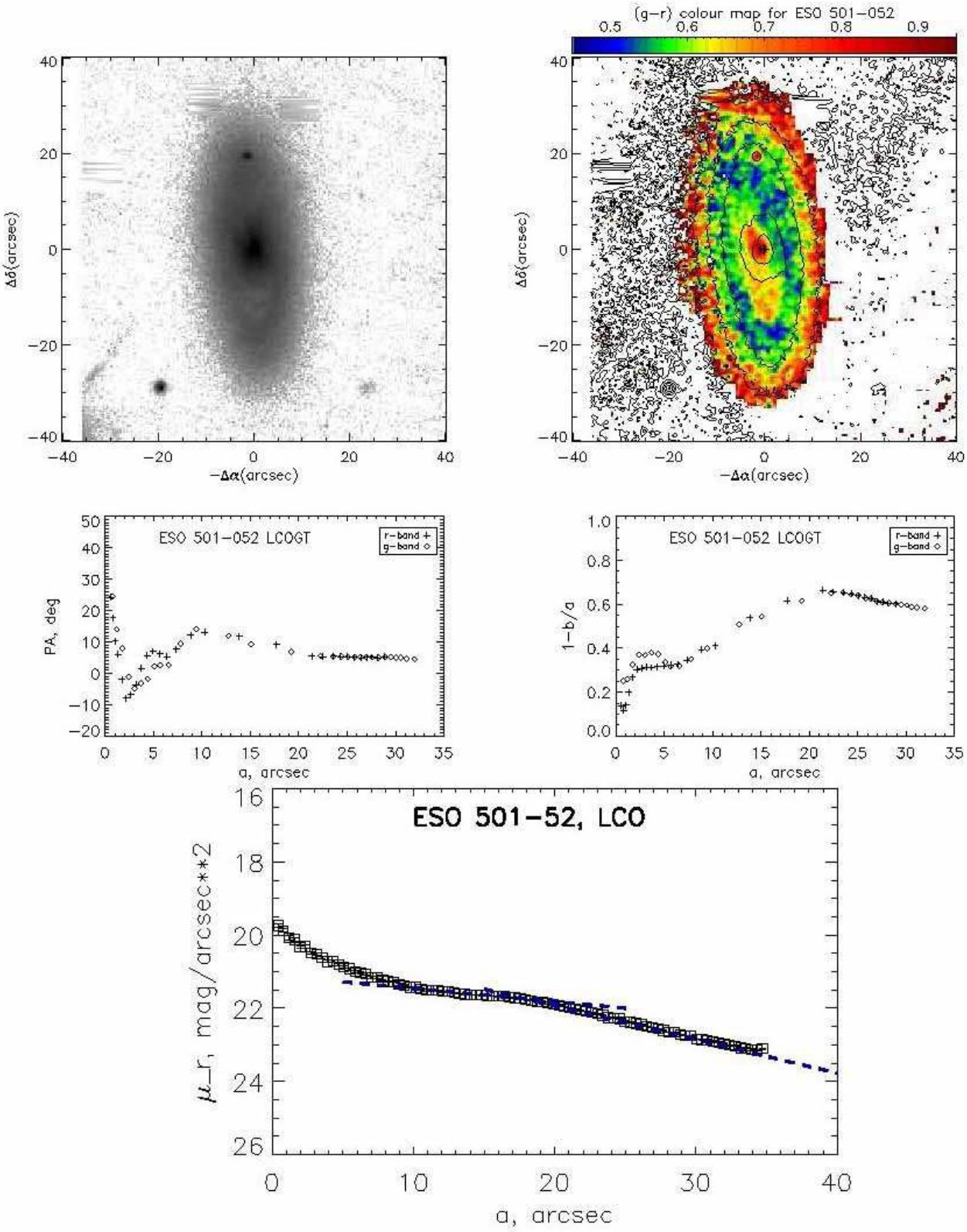
(g−r) colour map for ESO 501−052
0.5
0.6
0.7
0.8
0.9
Δδ(arcsec)
−Δα(arcsec)
ESO 501−052 LCOGT
r−band +
g−band ◇
PA, deg
a, arcsec
1−b/a
ESO 501−52, LCO
μ_r, mag/arcsec**2

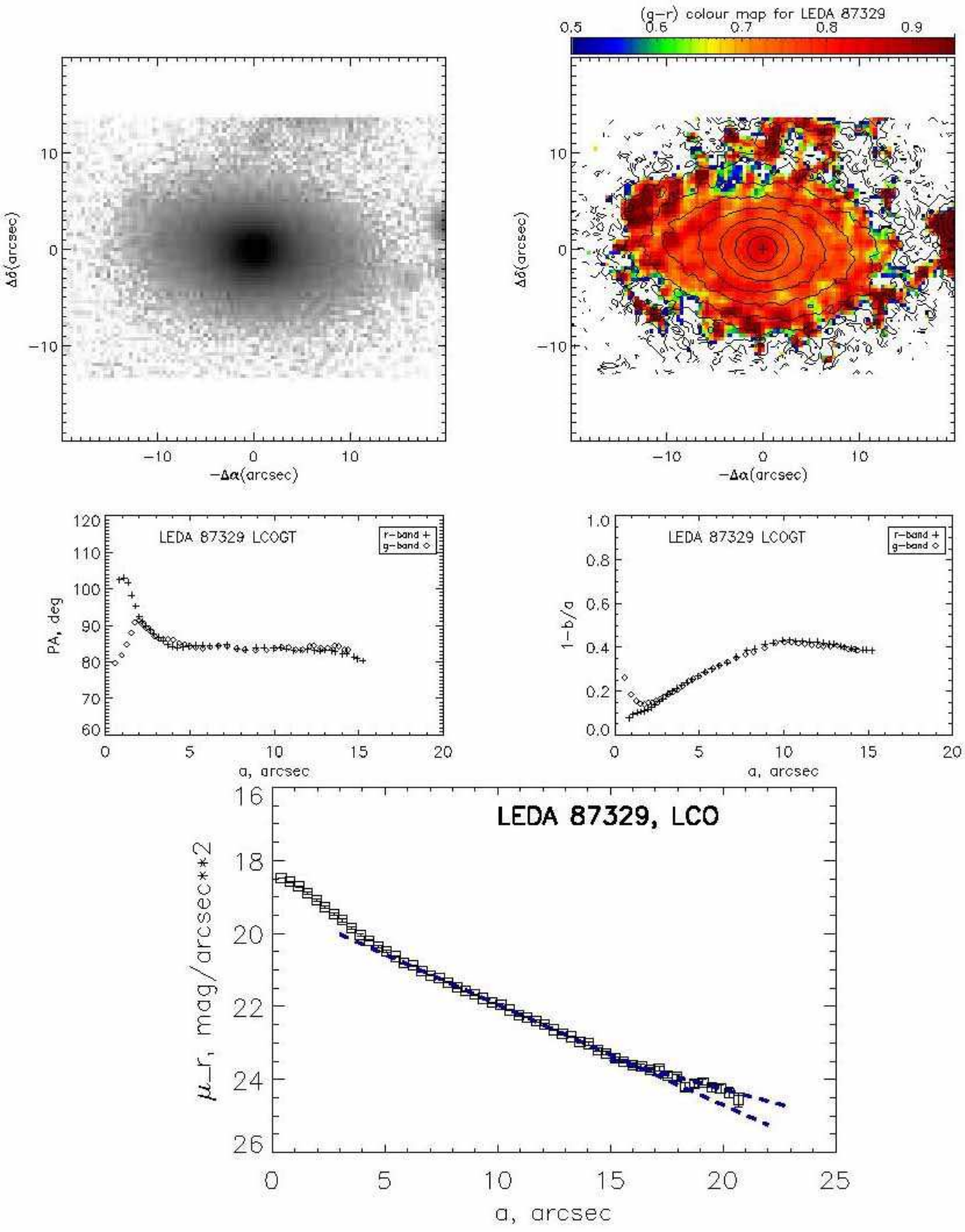
(g−r) colour map for LEDA 87329
0.5
0.6
0.7
0.8
0.9
Δδ(arcsec)
−Δα(arcsec)
LEDA 87329 LCOGT
r−band +
g−band ◇
PA, deg
1−b/a
a, arcsec
LEDA 87329, LCO
μ_r, mag/arcsec**2
a, arcsec

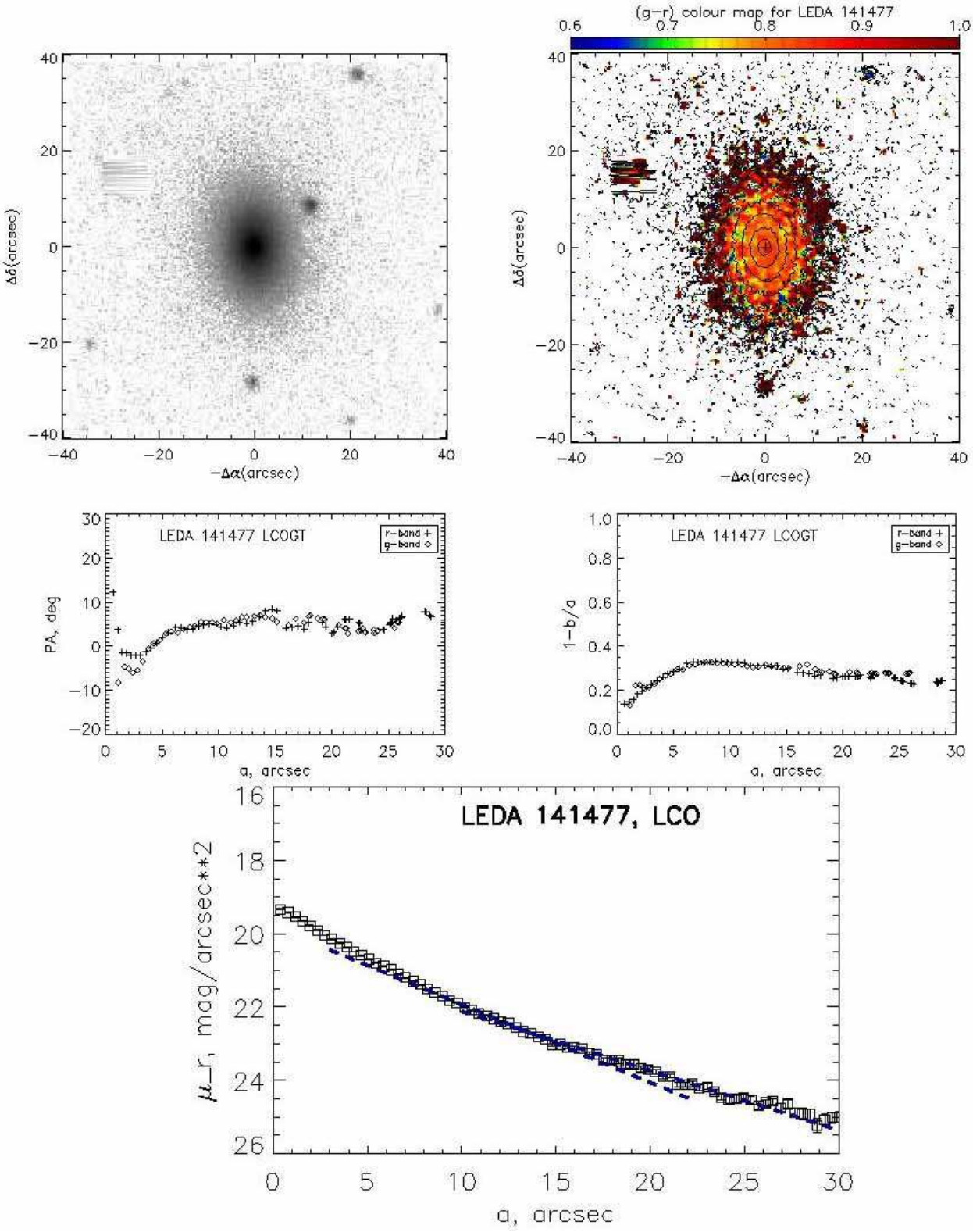
(g−r) colour map for LEDA 141477
0.6
0.7
0.8
0.9
1.0
Δδ(arcsec)
−Δα(arcsec)
LEDA 141477 LCOGT
r−band +
g−band ◇
PA, deg
a, arcsec
1−b/a
LEDA 141477, LCO
μ_r, mag/arcsec**2

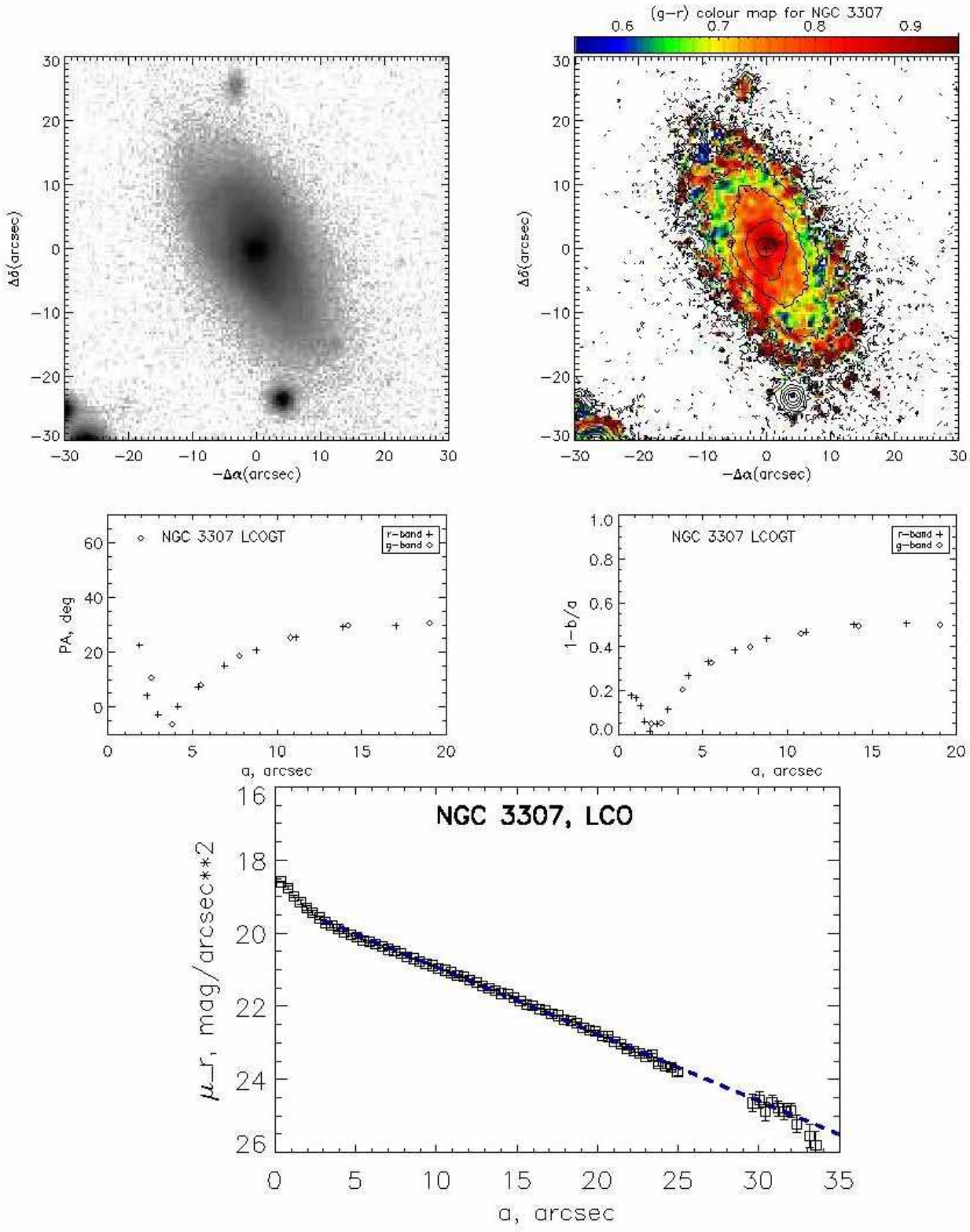
(g−r) colour map for NGC 3307
0.6
0.7
0.8
0.9
Δδ(arcsec)
−Δα(arcsec)
NGC 3307 LCOGT
r−band +
g−band ◇
PA, deg
a, arcsec
1−b/a
NGC 3307, LCO
μ⊥r, mag/arcsec**2

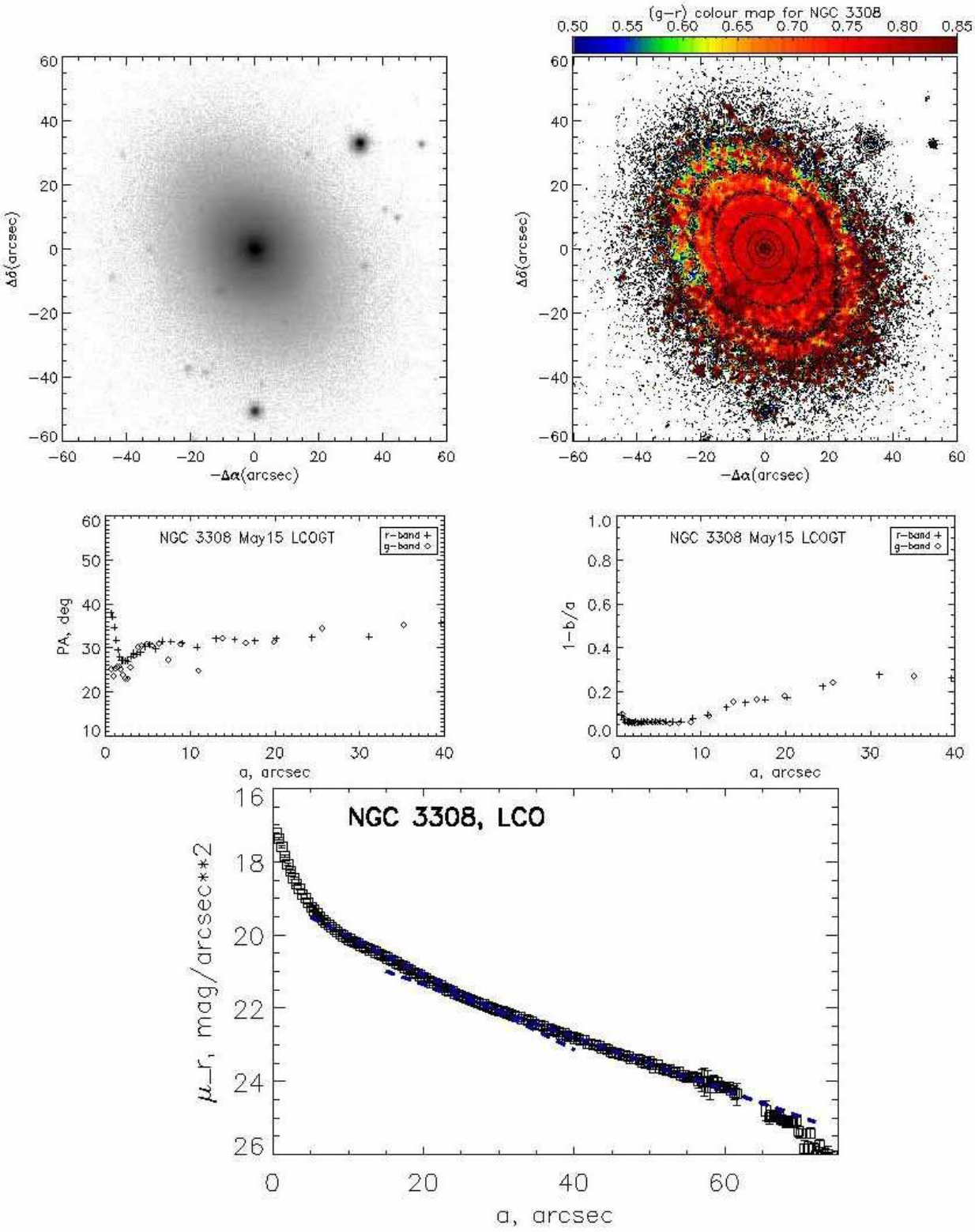
(g−r) colour map for NGC 3308
0.50 0.55 0.60 0.65 0.70 0.75 0.80 0.85
Δδ(arcsec)
−Δα(arcsec)
NGC 3308 May15 LCOGT
r−band +
g−band ◇
PA, deg
a, arcsec
1−b/a
NGC 3308, LCO
μ_r, mag/arcsec**2

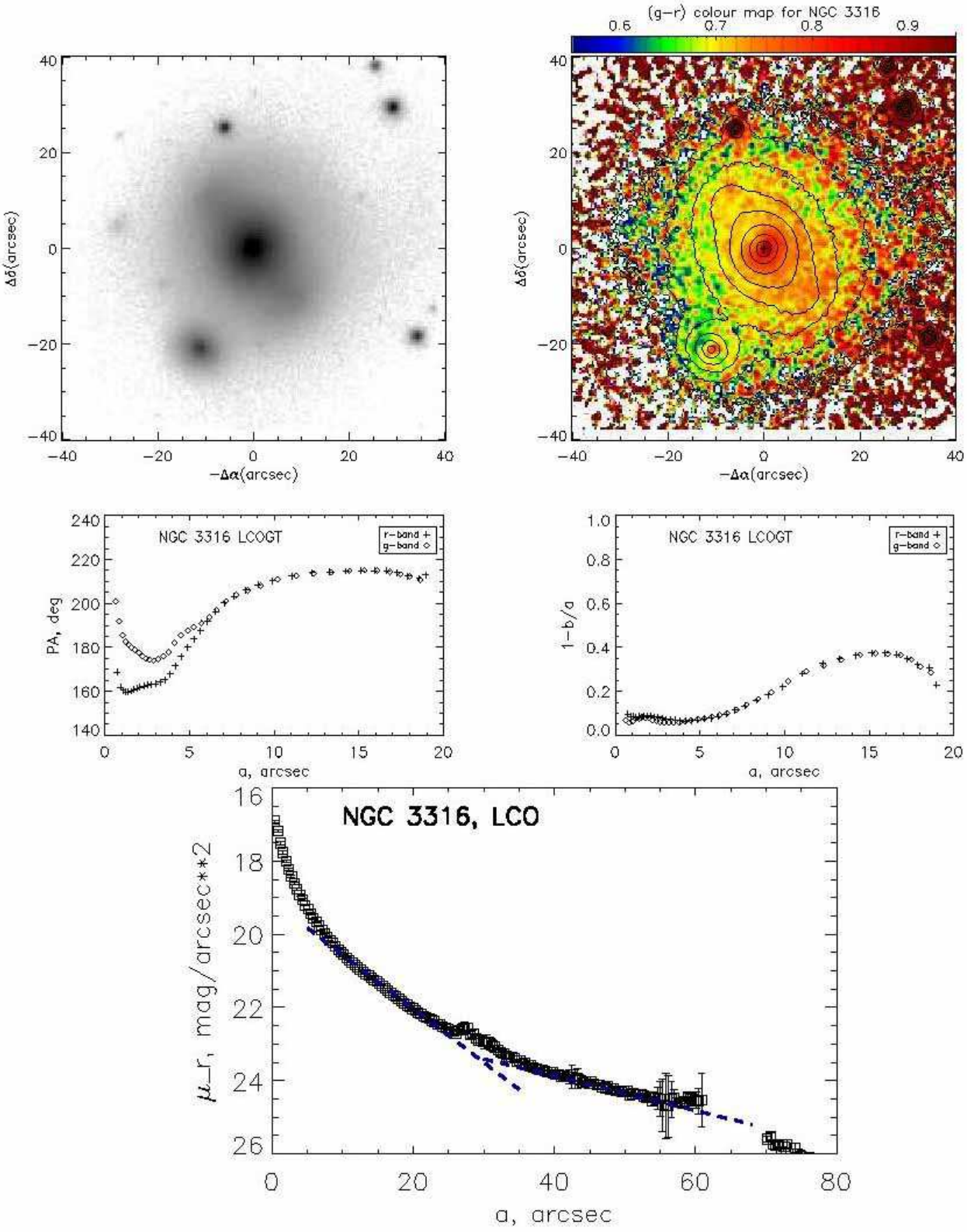
(g−r) colour map for NGC 3316
0.6
0.7
0.8
0.9
Δδ(arcsec)
−Δα(arcsec)
NGC 3316 LCOGT
r−band +
g−band ◇
PA, deg
1−b/a
a, arcsec
NGC 3316, LCO
μ_r, mag/arcsec**2
a, arcsec

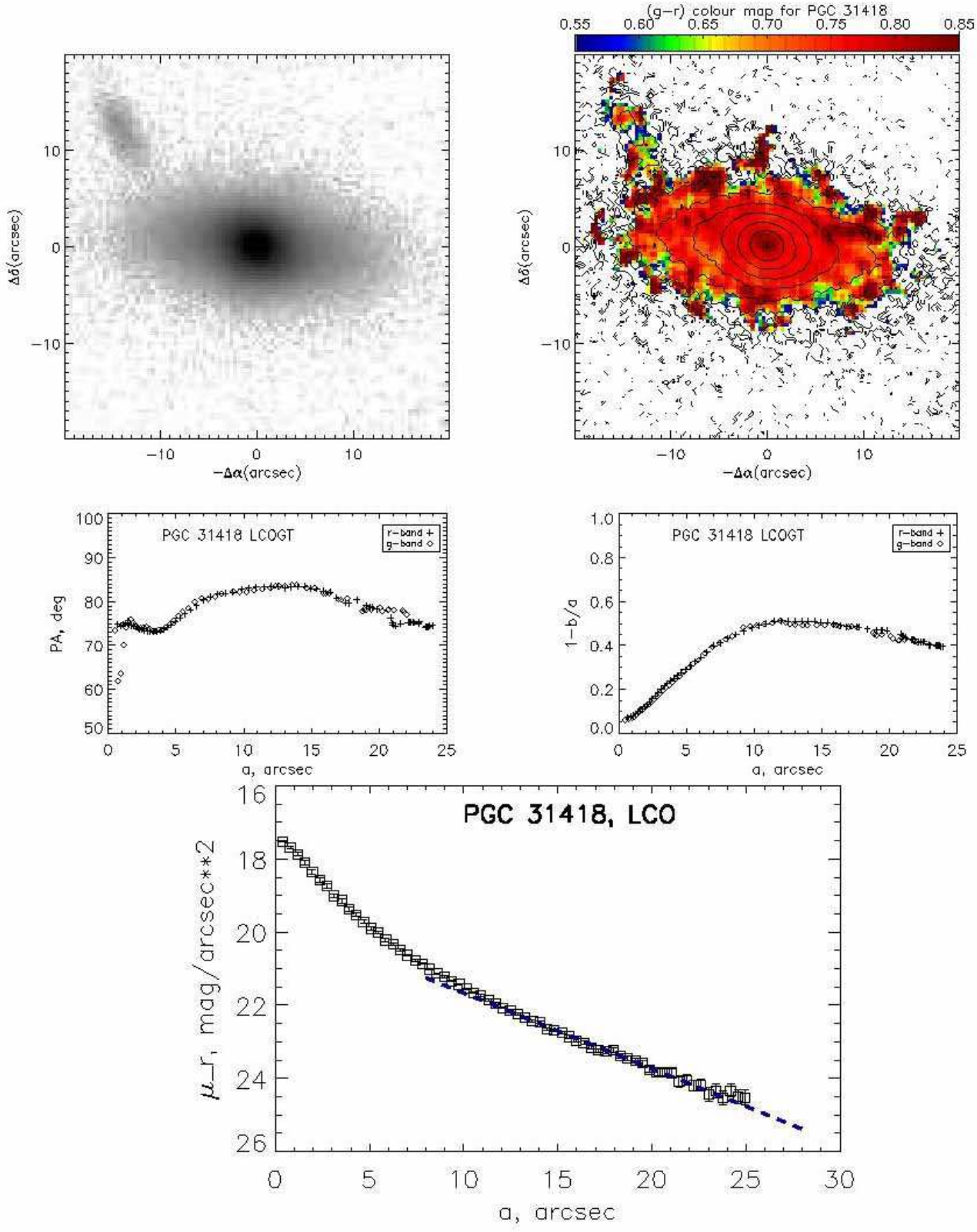
(g−r) colour map for PGC 31418
0.55 0.60 0.65 0.70 0.75 0.80 0.85
Δδ(arcsec)
−Δα(arcsec)
PGC 31418 LCOGT
r−band +
g−band ◇
PA, deg
1−b/a
a, arcsec
PGC 31418, LCO
μ_r, mag/arcsec**2
a, arcsec

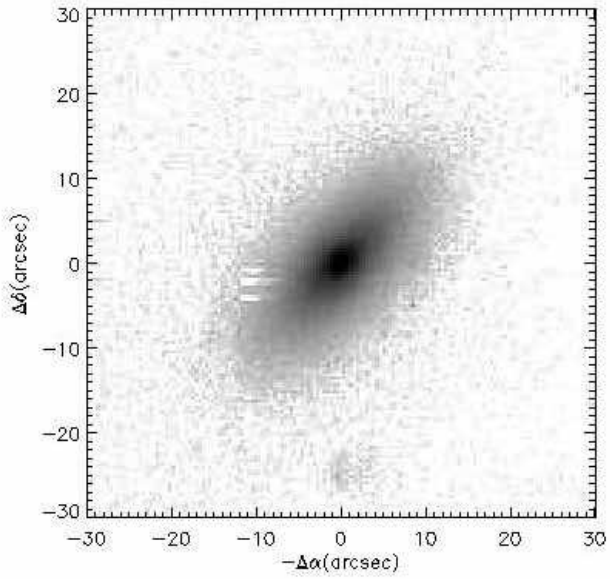
Δδ(arcsec)
−Δα(arcsec)

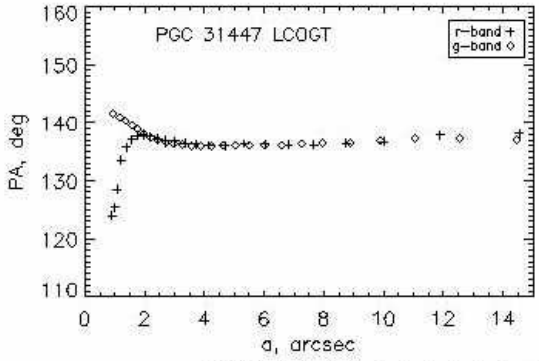
PGC 31447 LCOGT
r−band +
g−band ◇
PA, deg
a, arcsec

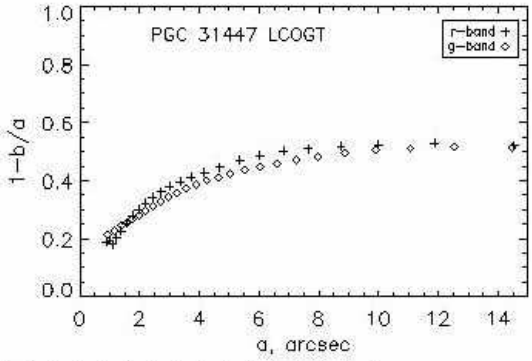
PGC 31447 LCOGT
r−band +
g−band ◇
1−b/a
a, arcsec

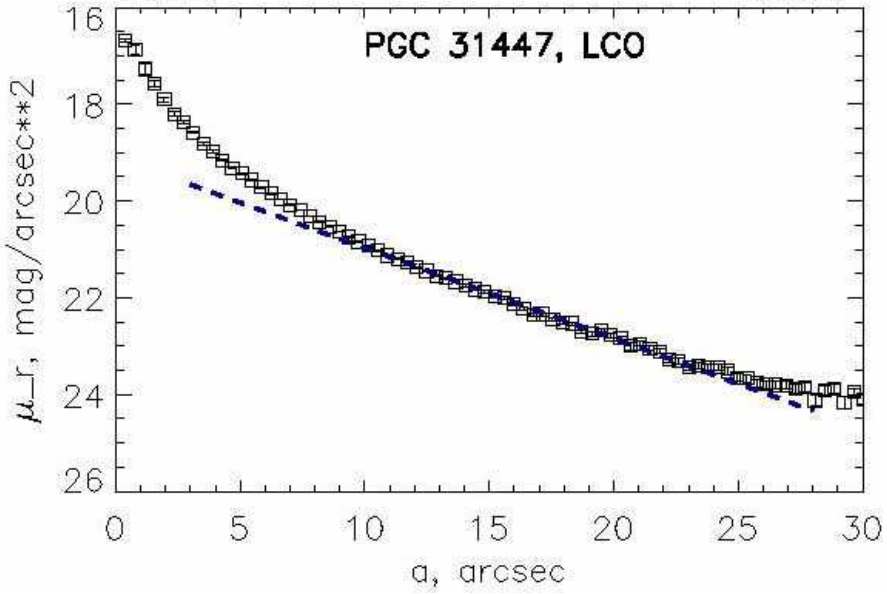
PGC 31447, LCO
μ_r, mag/arcsec**2
a, arcsec

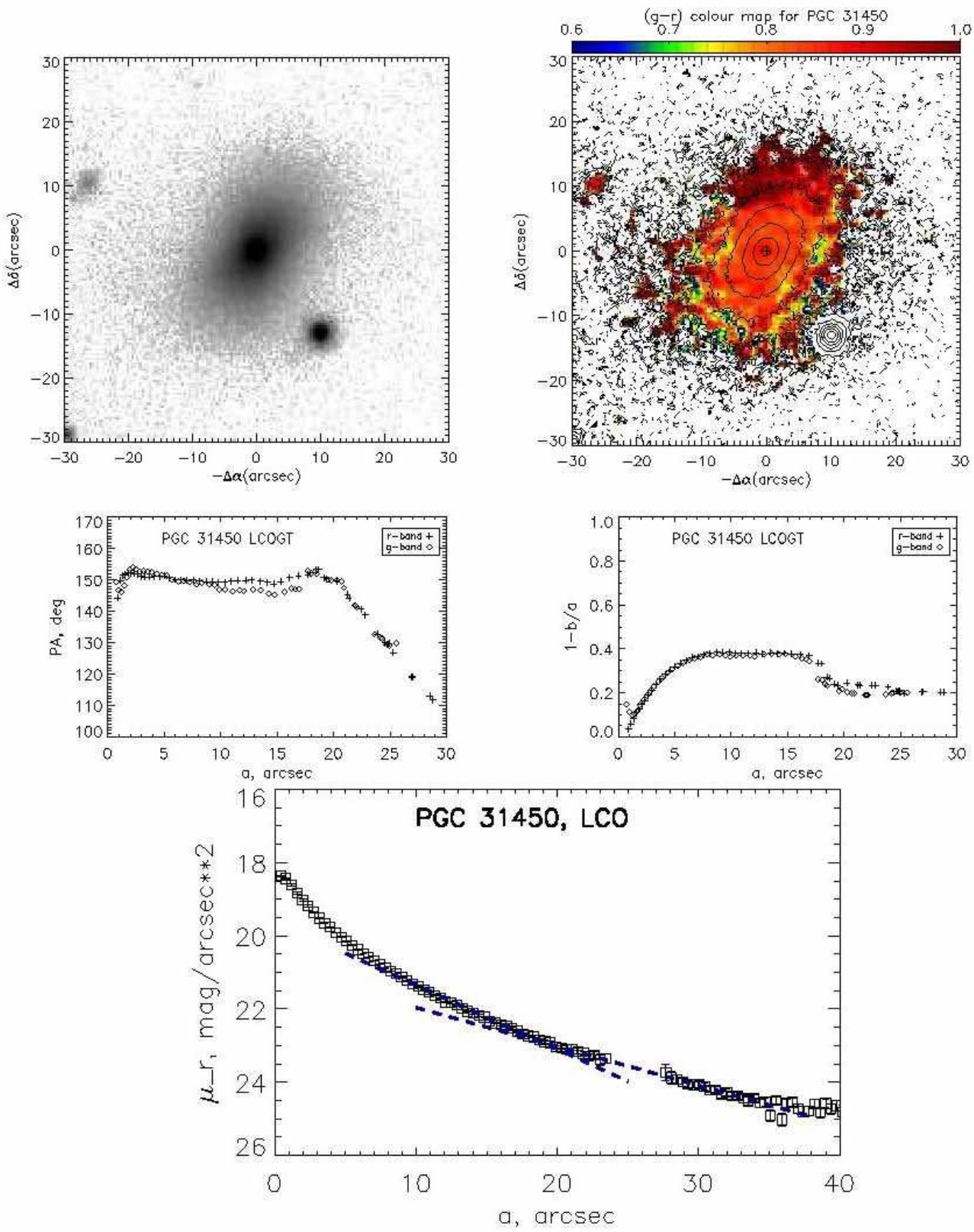
(g−r) colour map for PGC 31450
Δδ(arcsec)
−Δα(arcsec)
PGC 31450 LCOGT
r−band +
g−band ◇
PA, deg
a, arcsec
1−b/a
PGC 31450, LCO
μ_r, mag/arcsec**2

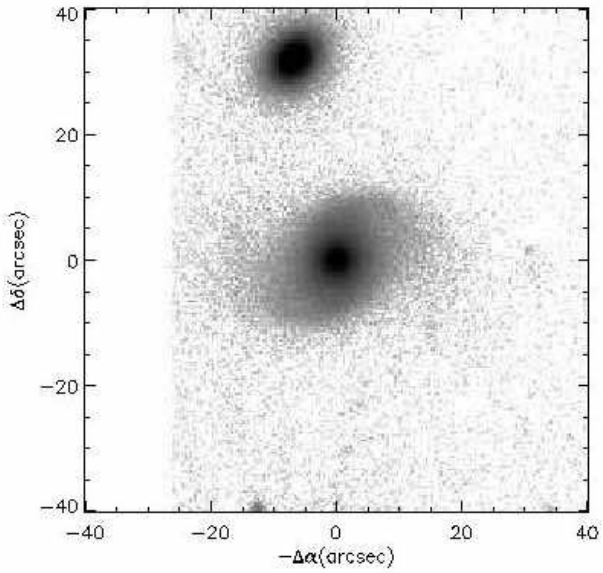
Δδ(arcsec)
−Δα(arcsec)

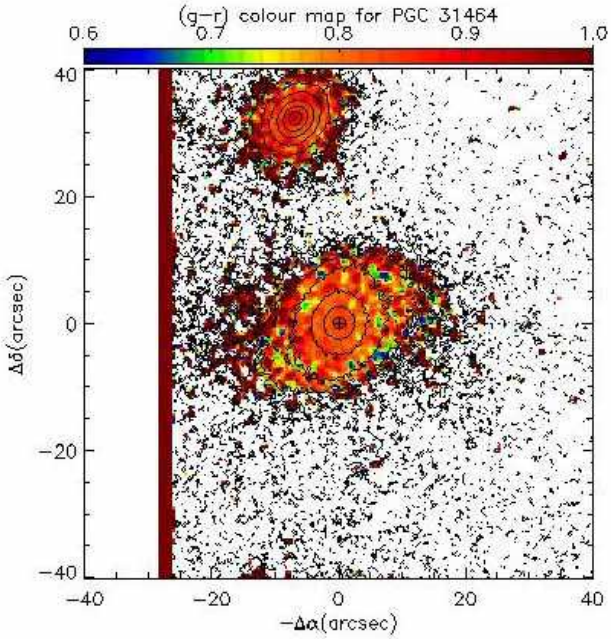
(g−r) colour map for PGC 31464
Δδ(arcsec)
−Δα(arcsec)

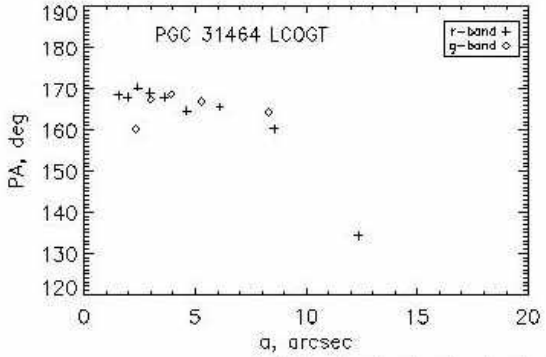
PGC 31464 LCOGT
r−band +
g−band ◇
PA, deg
a, arcsec

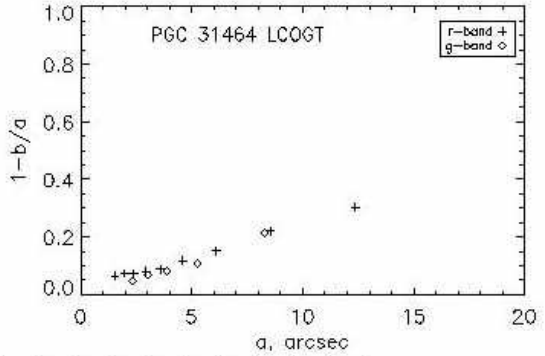
PGC 31464 LCOGT
r−band +
g−band ◇
1−b/a
a, arcsec

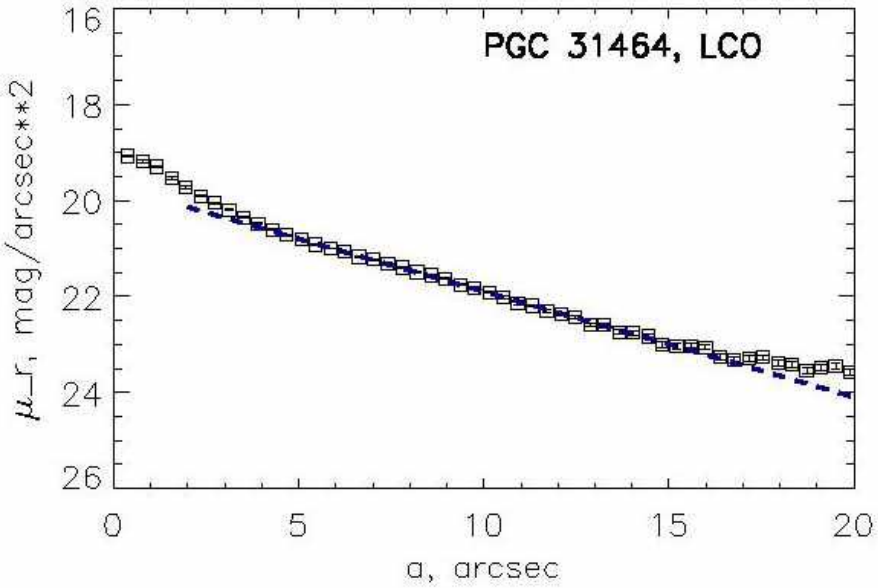
PGC 31464, LCO
μ_r, mag/arcsec**2
a, arcsec

6 Antlia

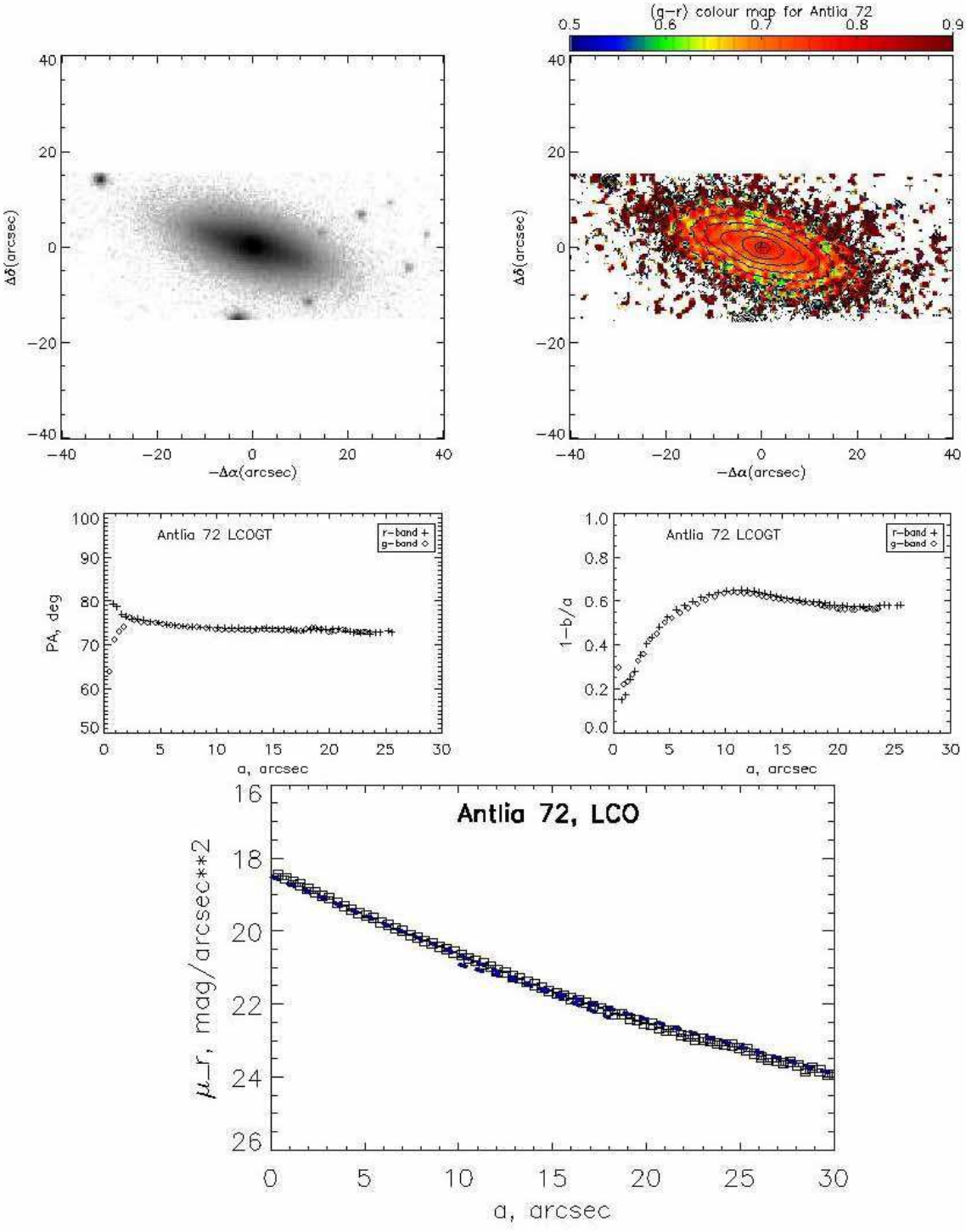
(g−r) colour map for Antlia 72
0.5
0.6
0.7
0.8
0.9
Δδ(arcsec)
−Δα(arcsec)
Antlia 72 LCOGT
r−band +
g−band ◇
PA, deg
1−b/a
a, arcsec
Antlia 72, LCO
μ_r, mag/arcsec**2

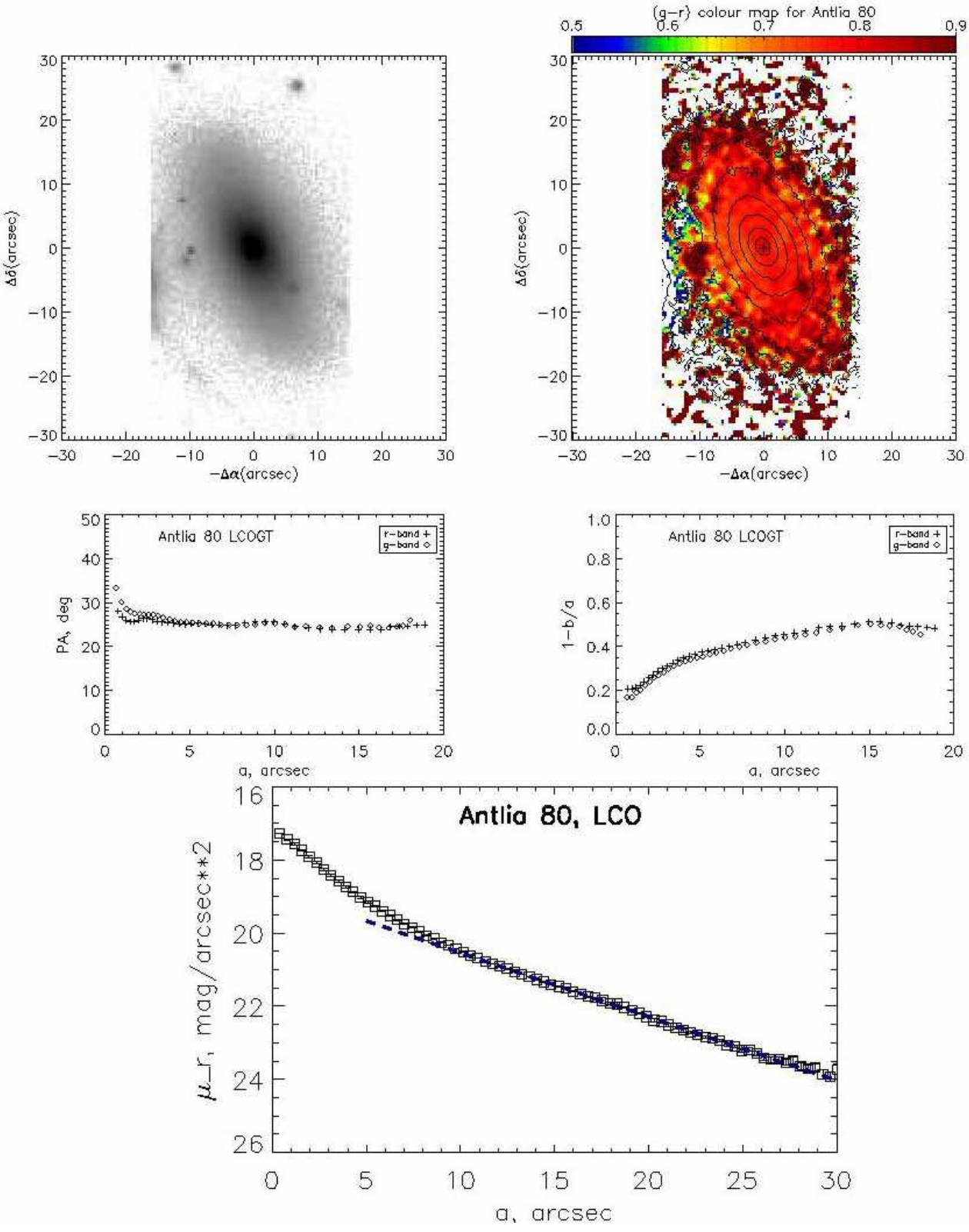
(g−r) colour map for Antlia 80
0.5
0.6
0.7
0.8
0.9
Δδ(arcsec)
−Δα(arcsec)
Antlia 80 LCOGT
r−band +
g−band ◇
PA, deg
a, arcsec
1−b/a
Antlia 80, LCO
μ_r, mag/arcsec**2

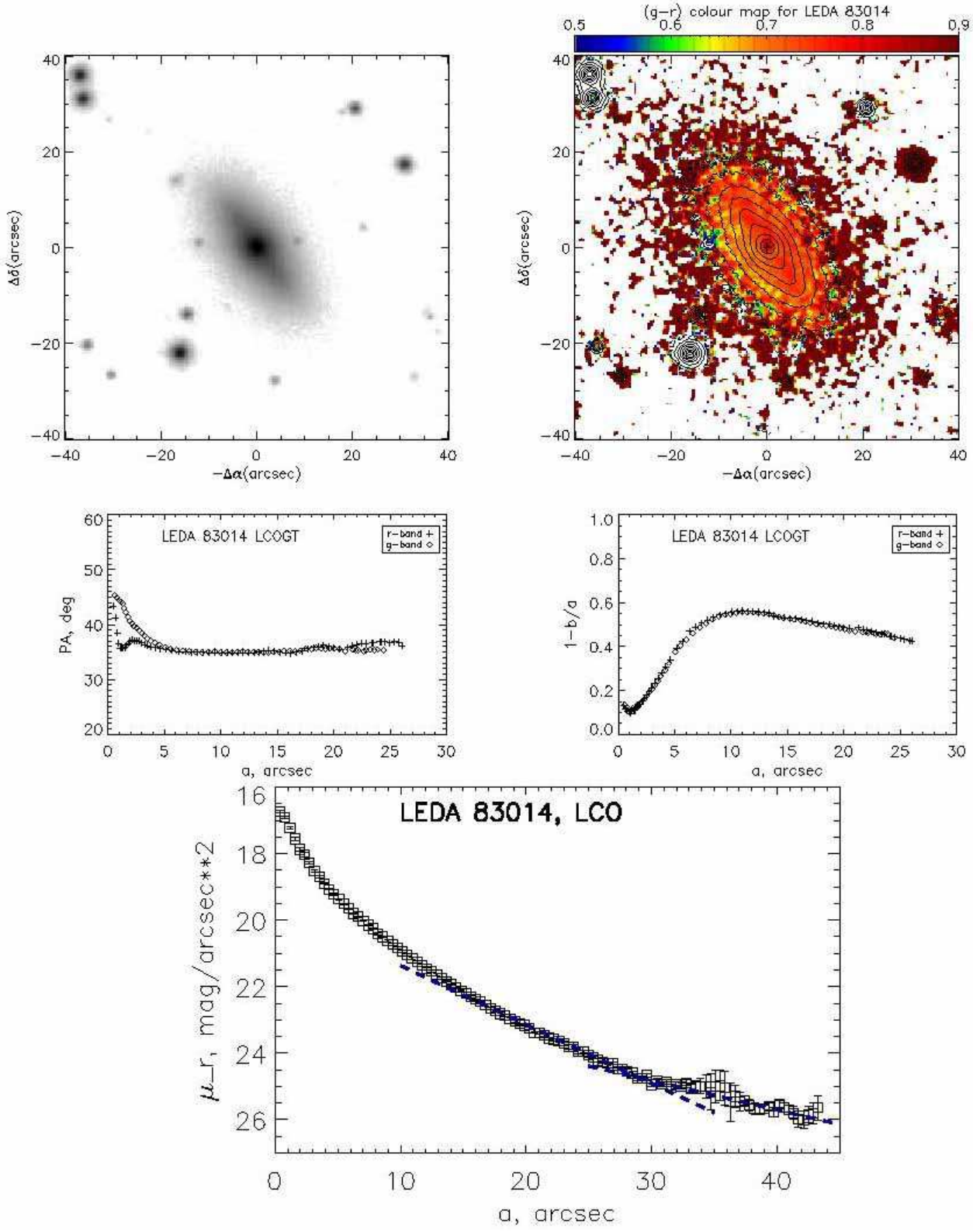
(g−r) colour map for LEDA 83014
0.5
0.6
0.7
0.8
0.9
Δδ(arcsec)
−Δα(arcsec)
LEDA 83014 LCOGT
r−band +
g−band ◇
PA, deg
a, arcsec
1−b/a
LEDA 83014, LCO
μ_r, mag/arcsec**2

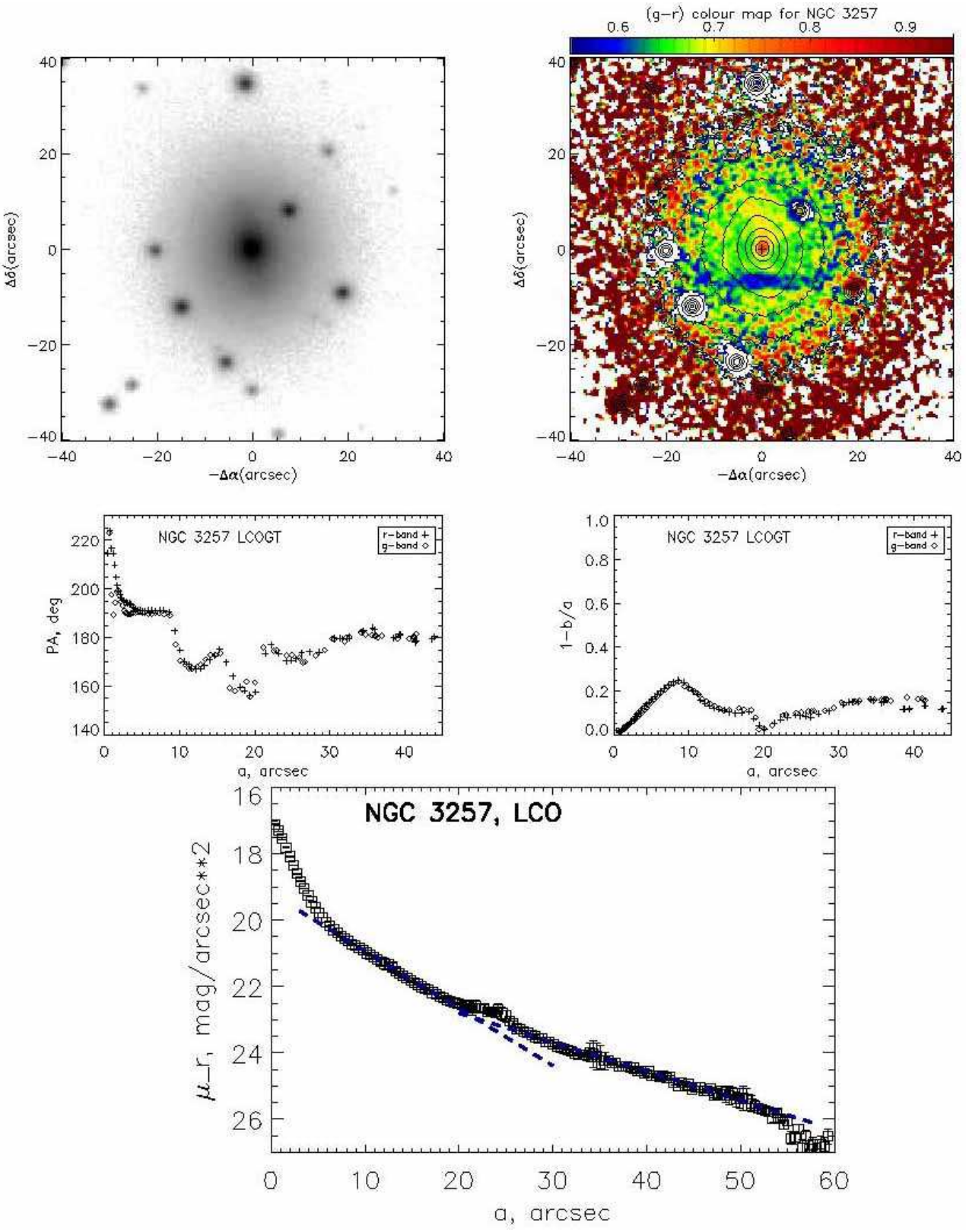
(g−r) colour map for NGC 3257
0.6
0.7
0.8
0.9
Δδ(arcsec)
−Δα(arcsec)
NGC 3257 LCOGT
r−band +
g−band ◇
PA, deg
a, arcsec
1−b/a
NGC 3257, LCO
μ_r, mag/arcsec**2

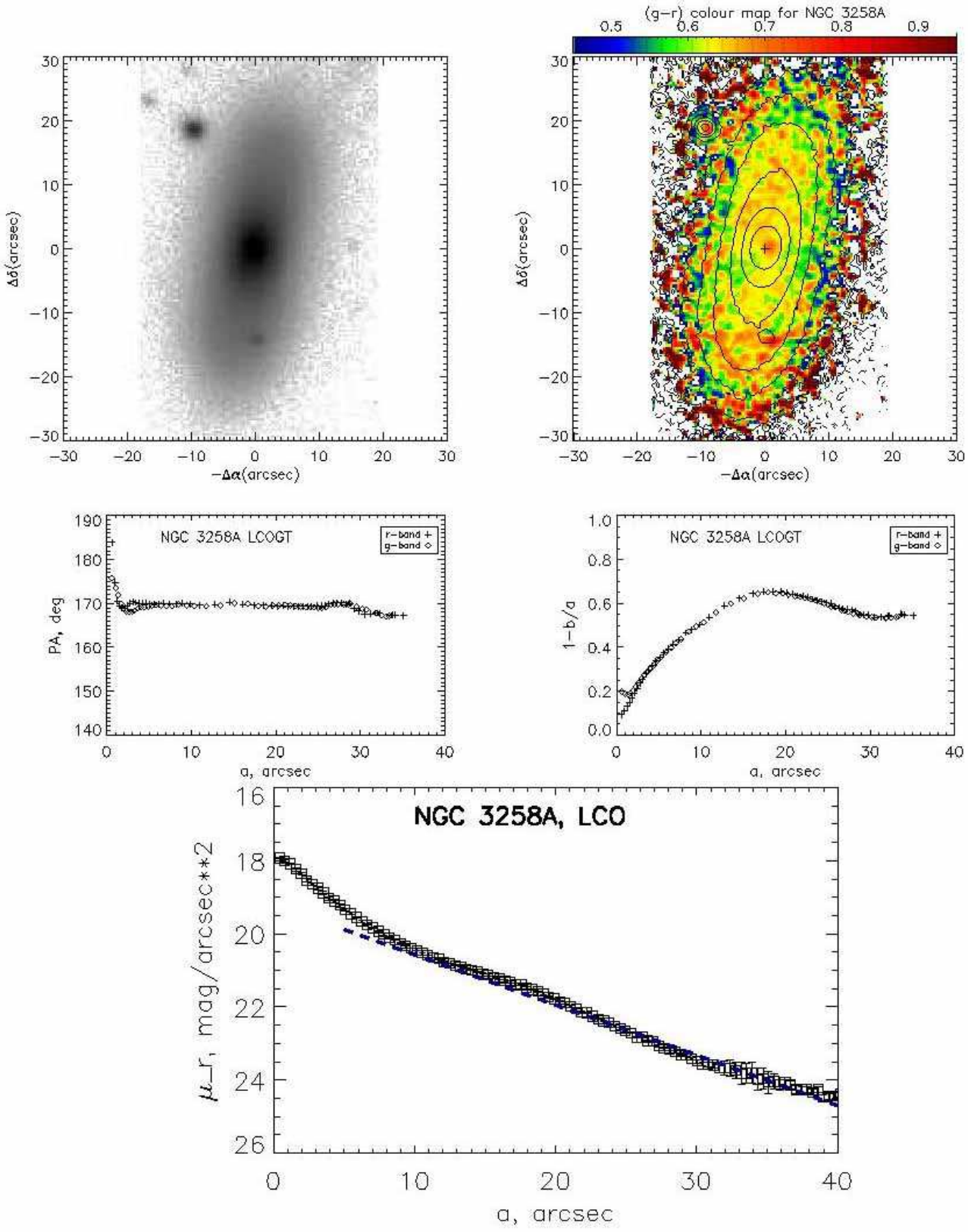
(g−r) colour map for NGC 3258A
0.5
0.6
0.7
0.8
0.9
Δδ(arcsec)
−Δα(arcsec)
NGC 3258A LCOGT
r−band +
g−band ◇
PA, deg
1−b/a
a, arcsec
NGC 3258A, LCO
μ_r, mag/arcsec**2

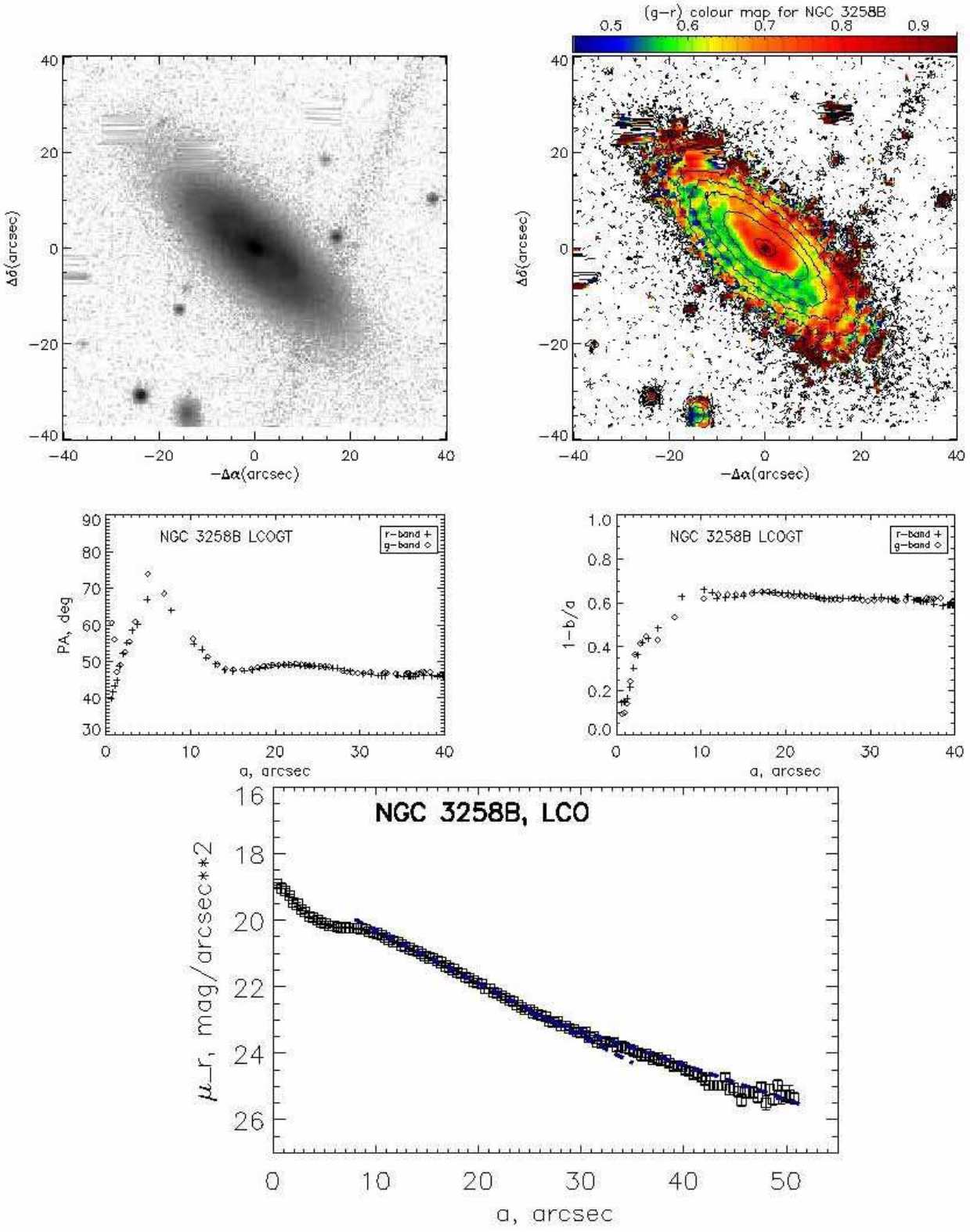
(g−r) colour map for NGC 3258B
0.5
0.6
0.7
0.8
0.9
Δδ(arcsec)
−Δα(arcsec)
NGC 3258B LCOGT
r−band +
g−band ◇
PA, deg
a, arcsec
1−b/a
NGC 3258B, LCO
μ_r, mag/arcsec**2

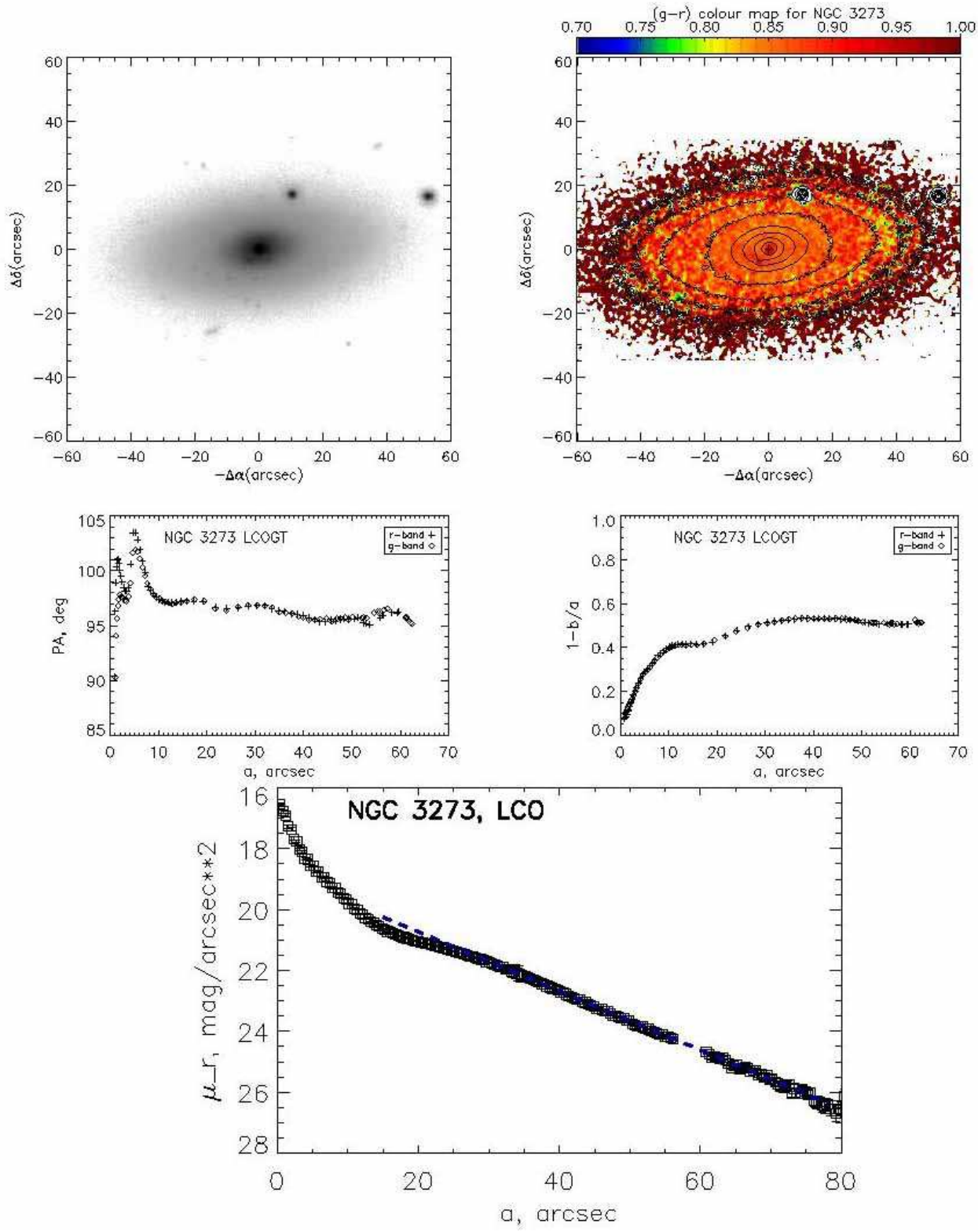
(g−r) colour map for NGC 3273
0.70 0.75 0.80 0.85 0.90 0.95 1.00
Δδ(arcsec)
−Δα(arcsec)
NGC 3273 LCOGT
r−band +
g−band ◇
PA, deg
a, arcsec
1−b/a
NGC 3273, LCO
μ_r, mag/arcsec**2

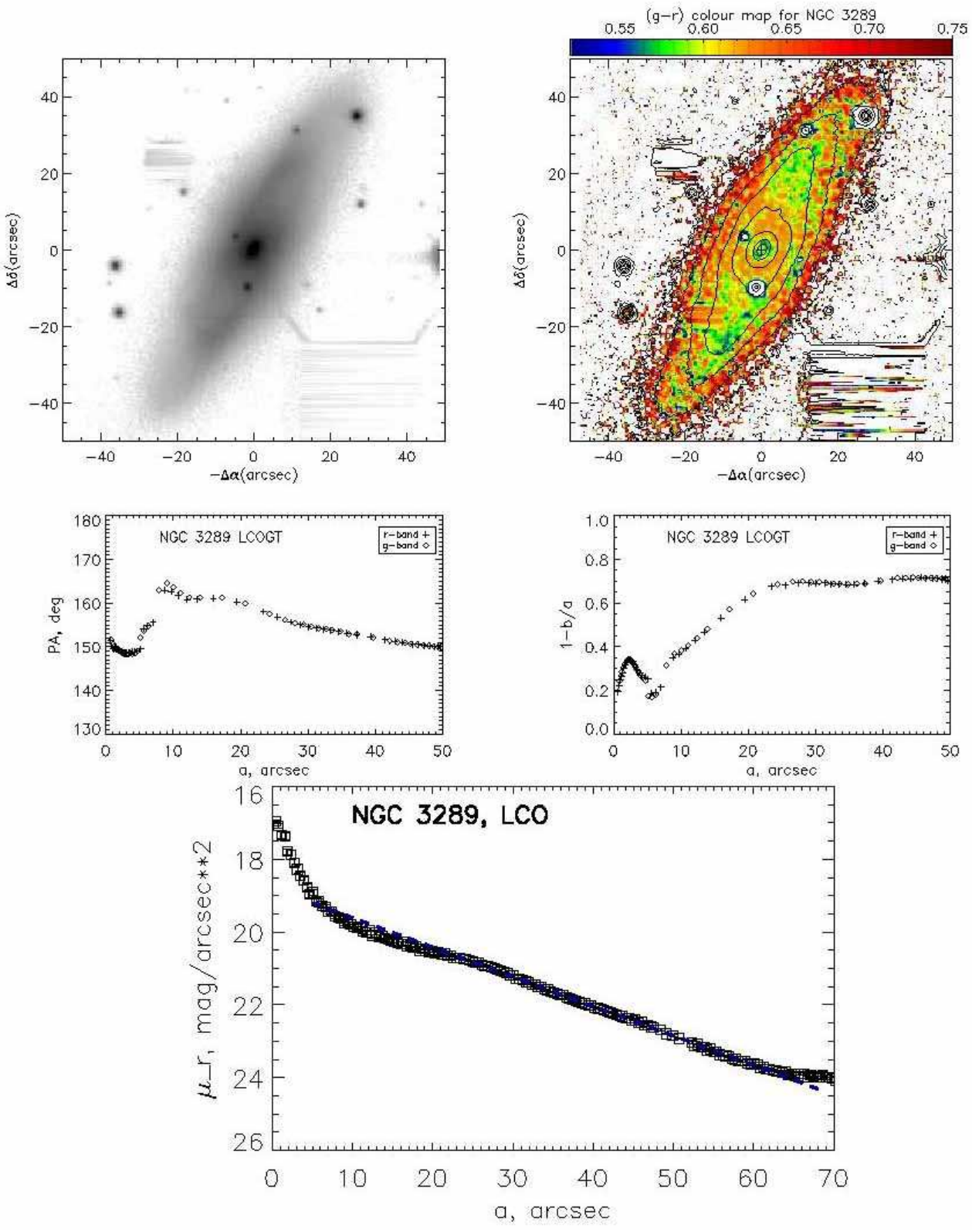
(g−r) colour map for NGC 3289
0.55
0.60
0.65
0.70
0.75
Δδ(arcsec)
−Δα(arcsec)
NGC 3289 LCOGT
r−band +
g−band ◇
PA, deg
a, arcsec
1−b/a
NGC 3289, LCO
μ_r, mag/arcsec**2

7 Abell 3565

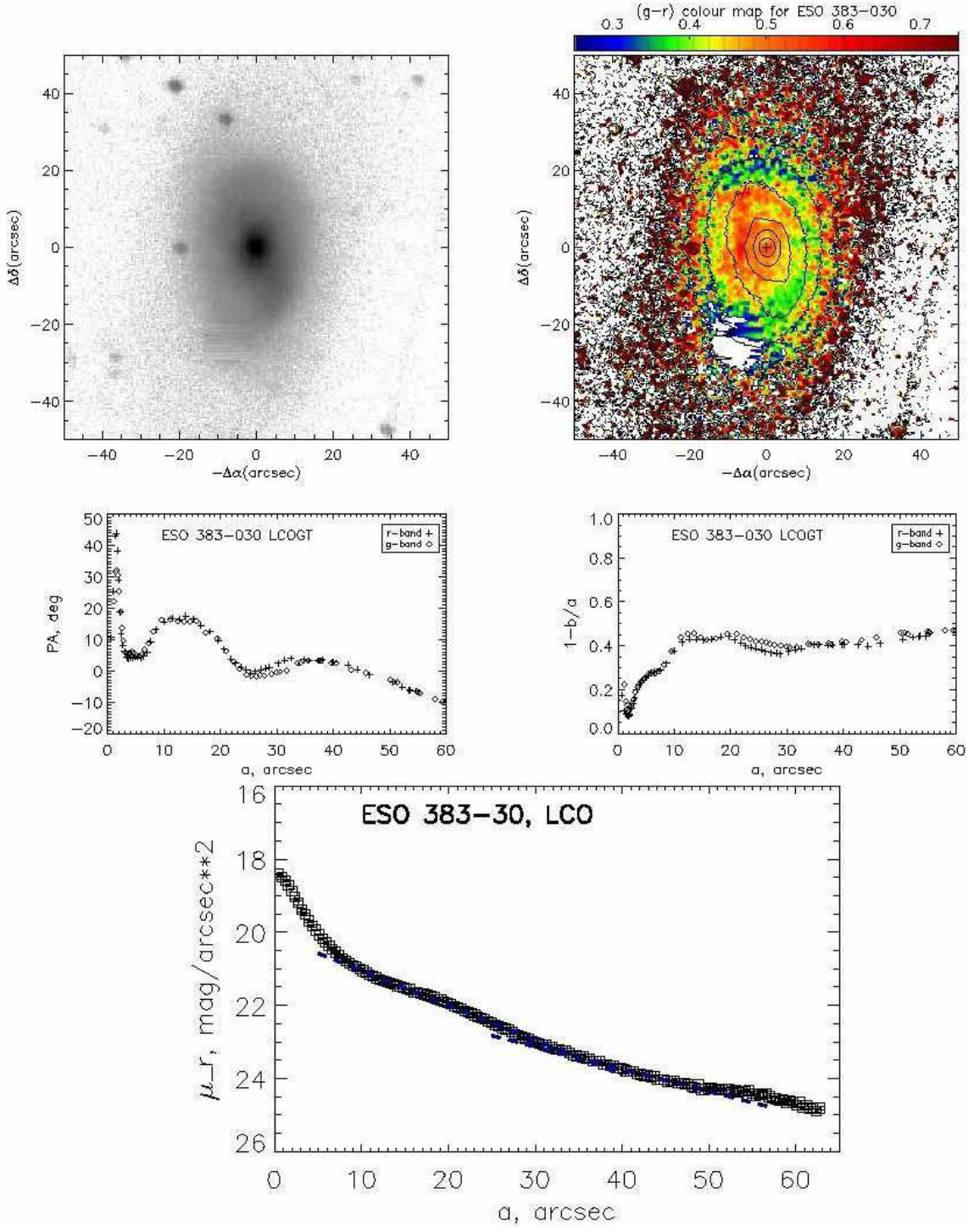
(g−r) colour map for ESO 383−030
0.3
0.4
0.5
0.6
0.7
Δδ(arcsec)
−Δα(arcsec)
ESO 383−030 LCOGT
r−band +
g−band ◇
PA, deg
a, arcsec
1−b/a
ESO 383−30, LCO
μ_r, mag/arcsec**2

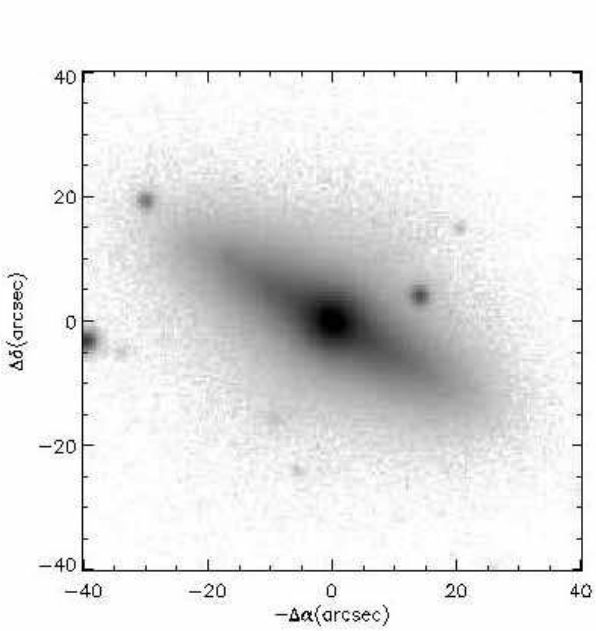
40
20
0
−20
−40
−40
−20
0
20
40
Δδ(arcsec)
−Δα(arcsec)

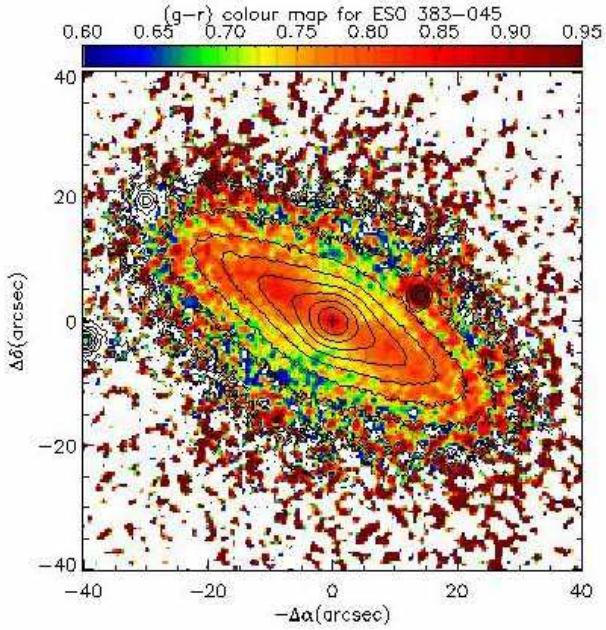
(g−r) colour map for ESO 383−045
0.60 0.65 0.70 0.75 0.80 0.85 0.90 0.95
40
20
0
−20
−40
−40
−20
0
20
40
Δδ(arcsec)
−Δα(arcsec)

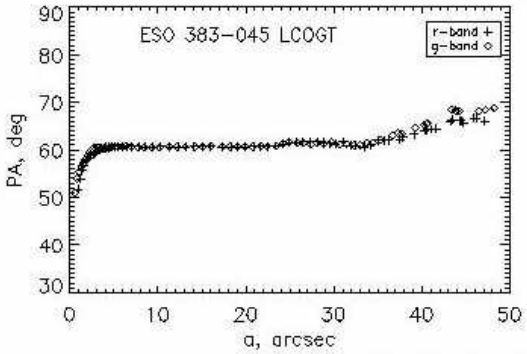
ESO 383−045 LCOGT
r−band +
g−band ◇
90
80
70
60
50
40
30
PA, deg
0
10
20
30
40
50
a, arcsec

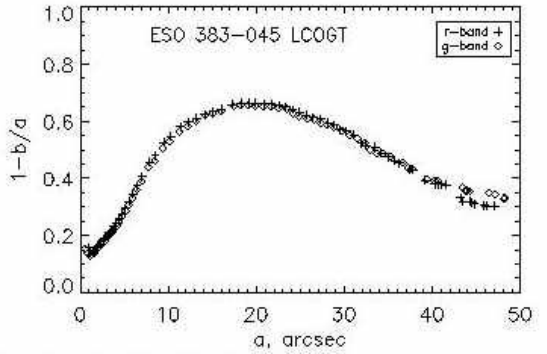
ESO 383−045 LCOGT
r−band +
g−band ◇
1.0
0.8
0.6
0.4
0.2
0.0
1−b/a
0
10
20
30
40
50
a, arcsec

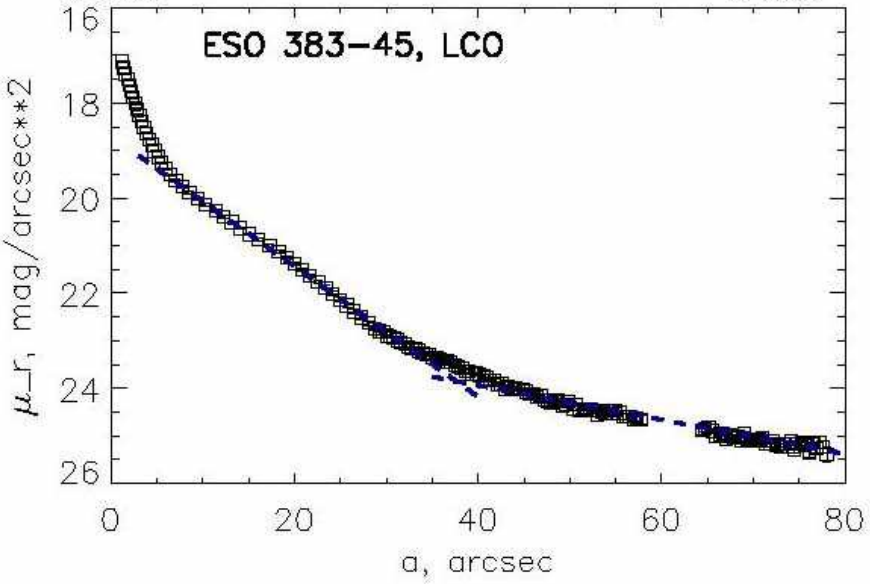
ESO 383−45, LCO
16
18
20
22
24
26
μ_r, mag/arcsec**2
0
20
40
60
80
a, arcsec

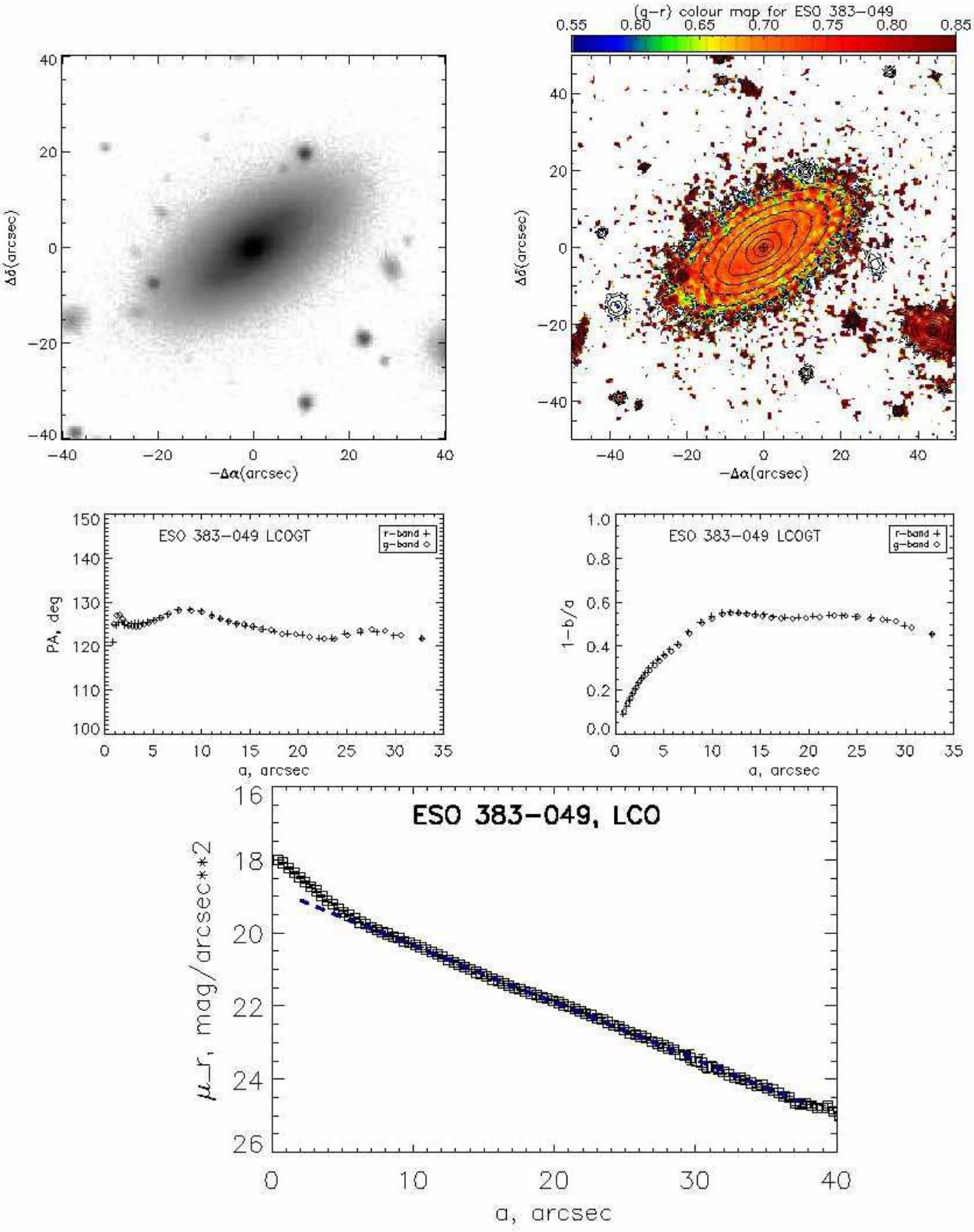
(g−r) colour map for ESO 383−049
0.55 0.60 0.65 0.70 0.75 0.80 0.85
Δδ(arcsec)
−Δα(arcsec)
ESO 383−049 LCOGT
r−band +
g−band ◇
PA, deg
a, arcsec
1−b/a
ESO 383−049, LCO
μ_r, mag/arcsec**2

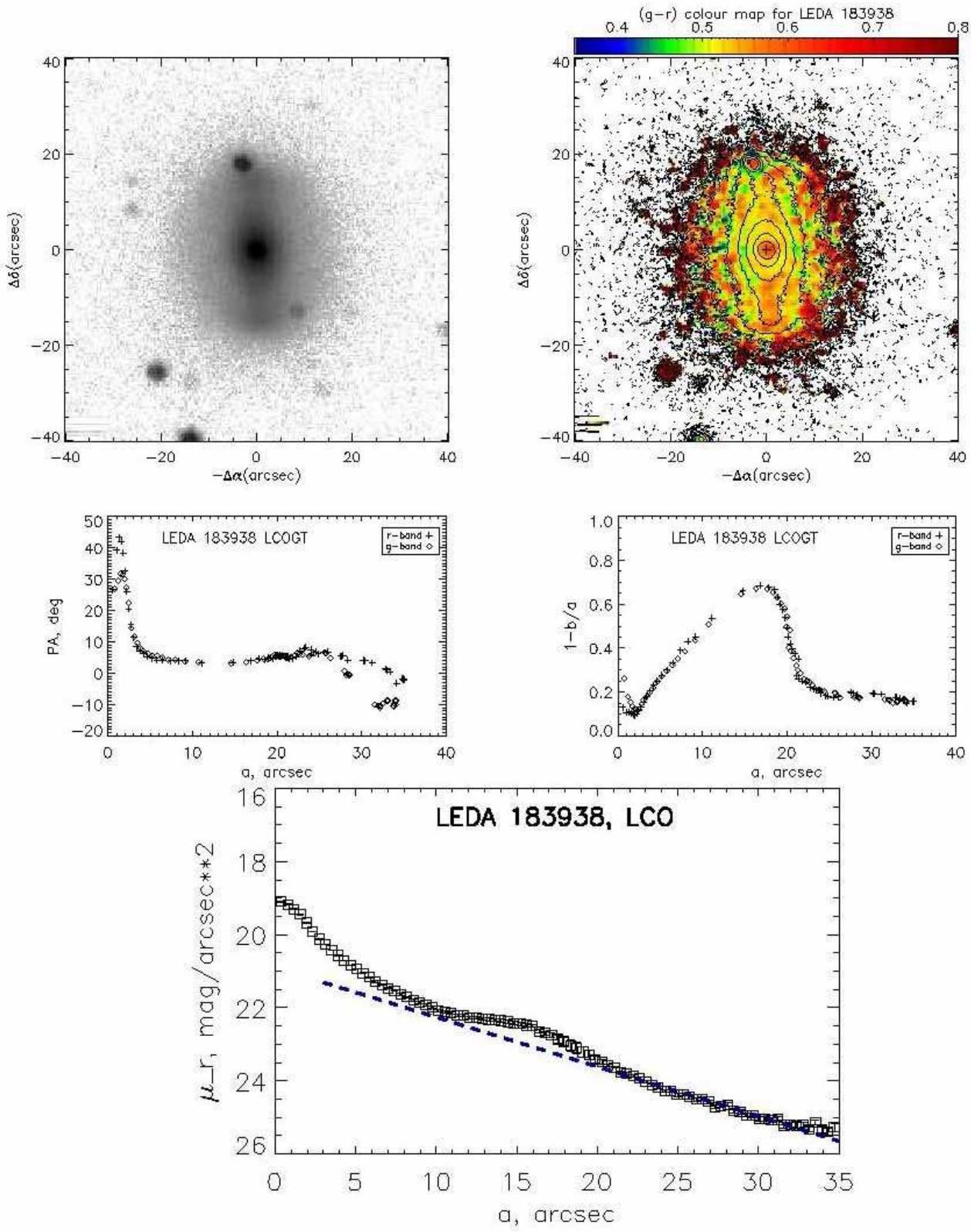
(g−r) colour map for LEDA 183938
0.4
0.5
0.6
0.7
0.8
Δδ(arcsec)
−Δα(arcsec)
LEDA 183938 LCOGT
r−band +
g−band ◇
PA, deg
a, arcsec
1−b/a
LEDA 183938, LCO
μ_r, mag/arcsec**2

8 Abell S0805

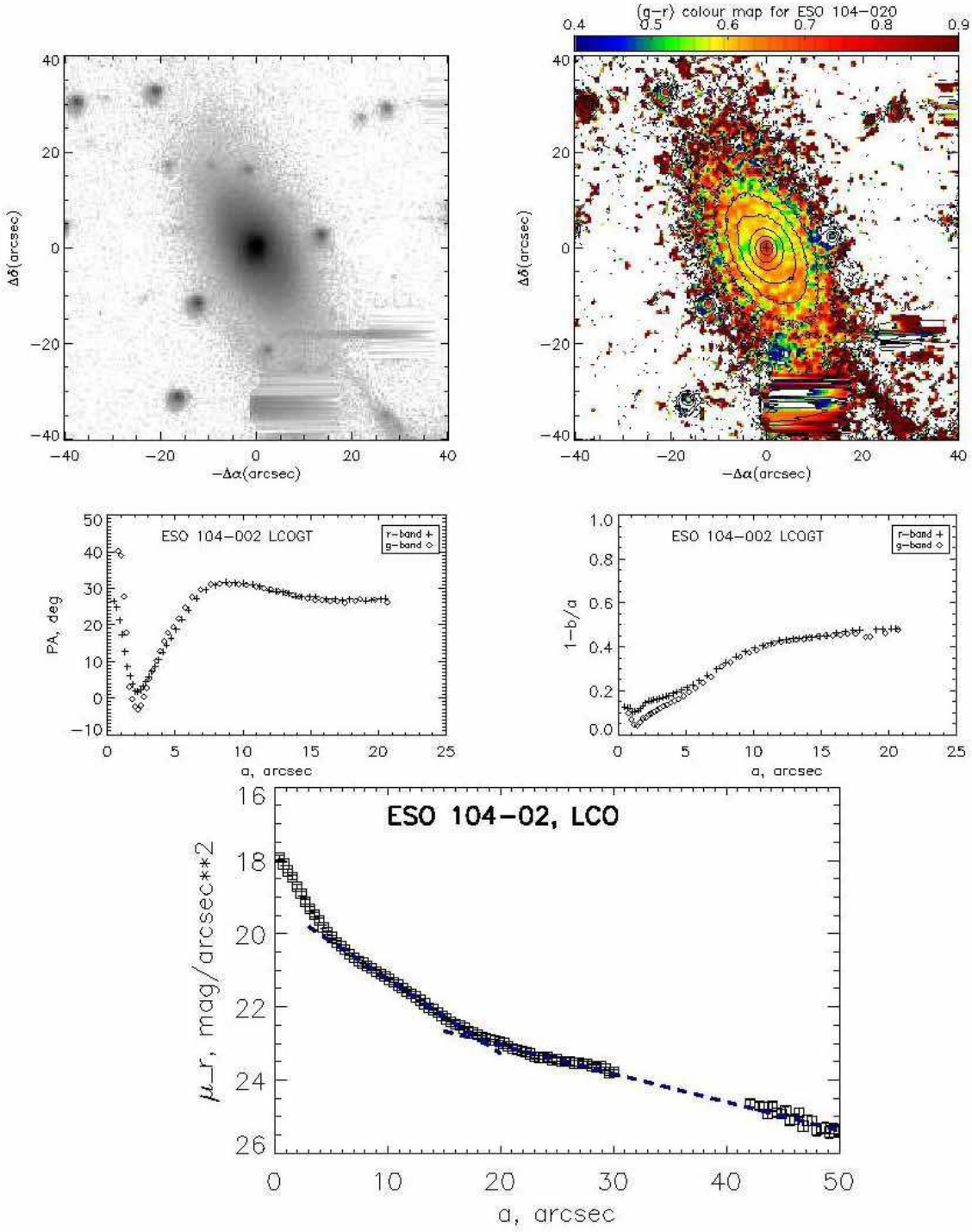

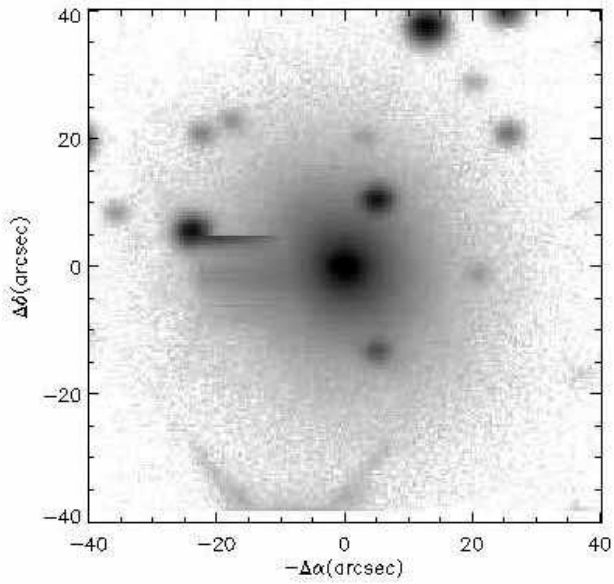
40
20
0
−20
−40
Δδ(arcsec)
−40
−20
0
20
40
−Δα(arcsec)

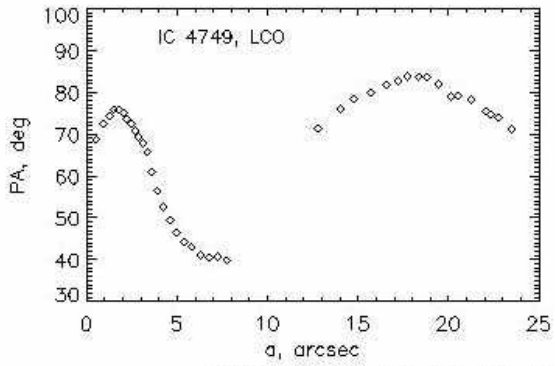
IC 4749, LCO
PA, deg
a, arcsec

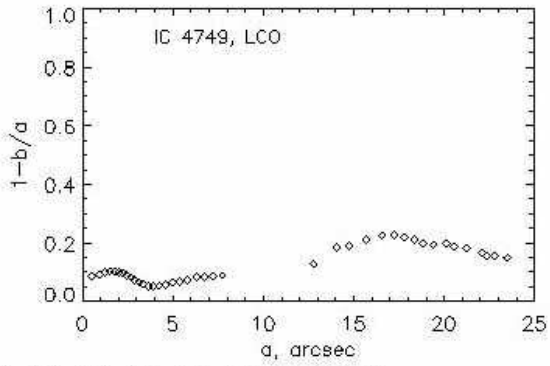
IC 4749, LCO
1−b/a
a, arcsec

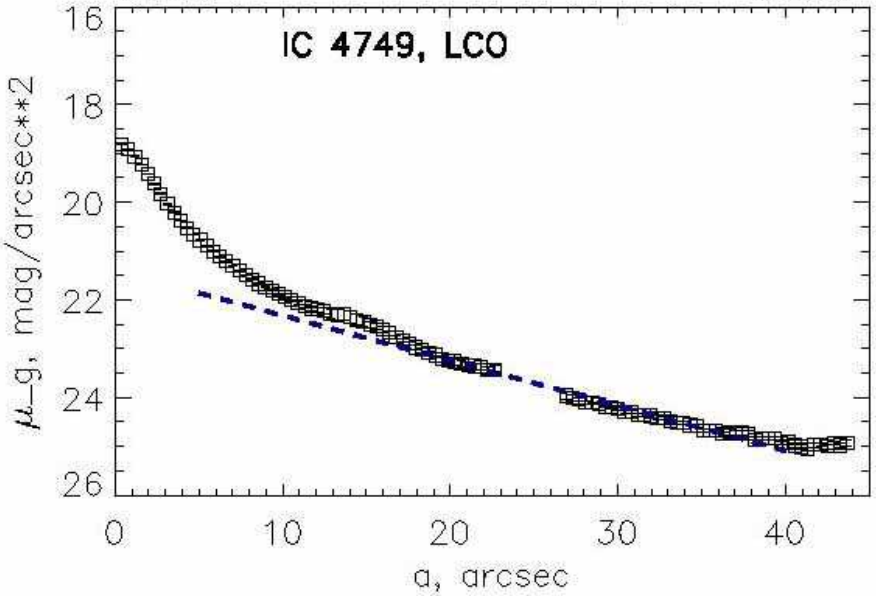
IC 4749, LCO
μ_g, mag/arcsec**2
a, arcsec

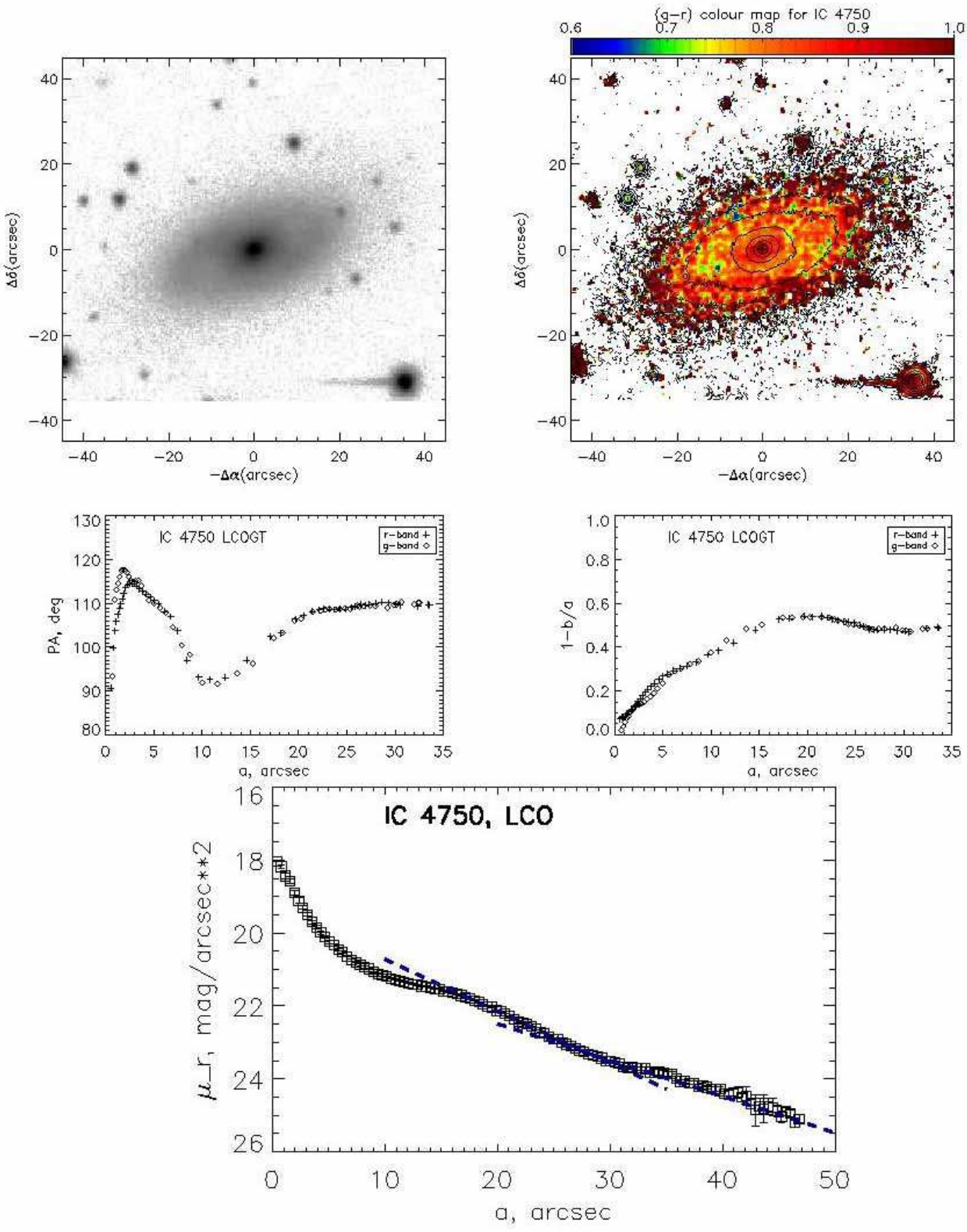
(g−r) colour map for IC 4750
0.6
0.7
0.8
0.9
1.0
Δδ(arcsec)
−Δα(arcsec)
IC 4750 LCOGT
r−band +
g−band ◇
PA, deg
a, arcsec
1−b/a
IC 4750, LCO
μ_r, mag/arcsec**2

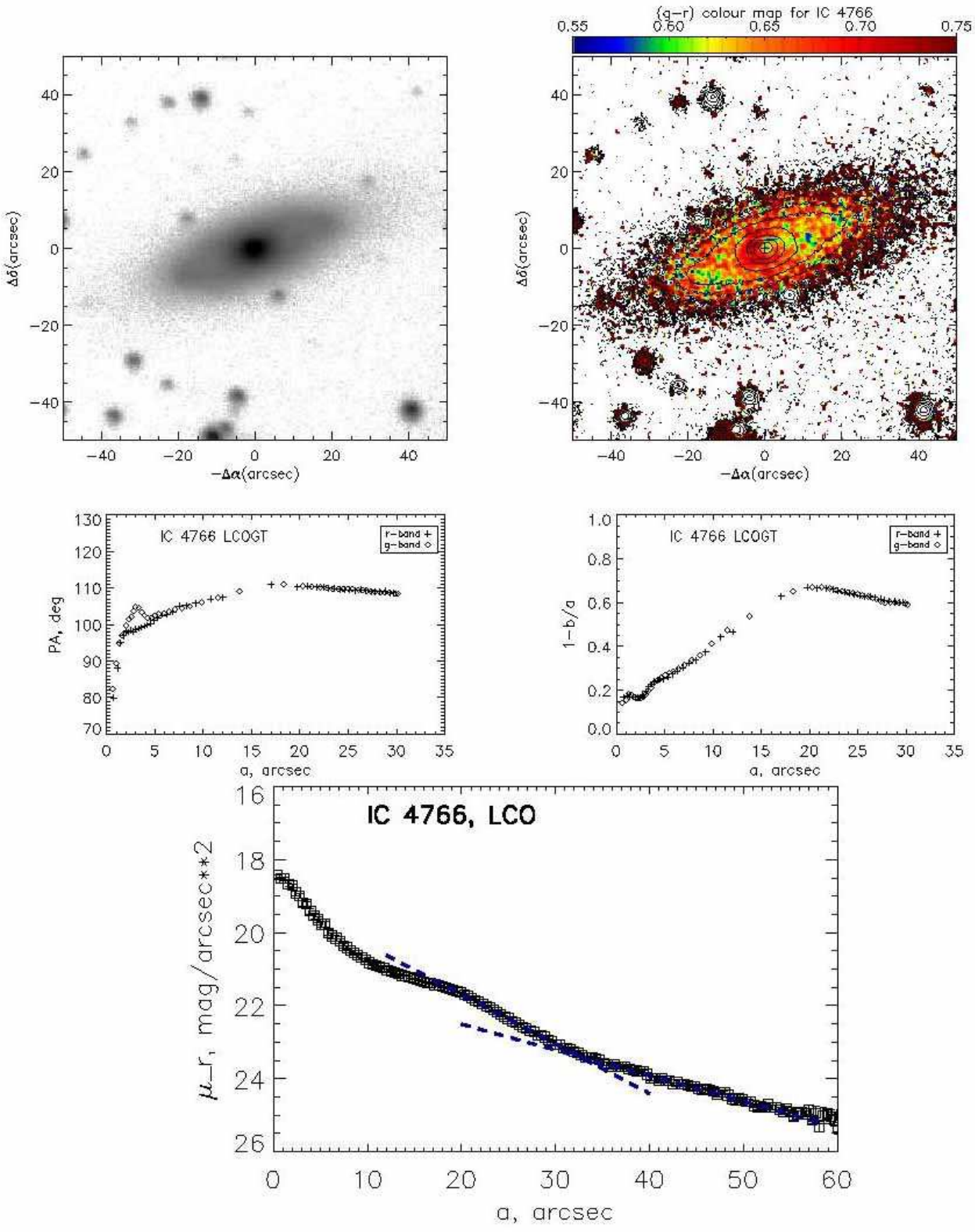
(g−r) colour map for IC 4766
0.55
0.60
0.65
0.70
0.75
Δδ(arcsec)
−Δα(arcsec)
IC 4766 LCOGT
r−band +
g−band ◇
PA, deg
1−b/a
a, arcsec
IC 4766, LCO
μ_r, mag/arcsec**2

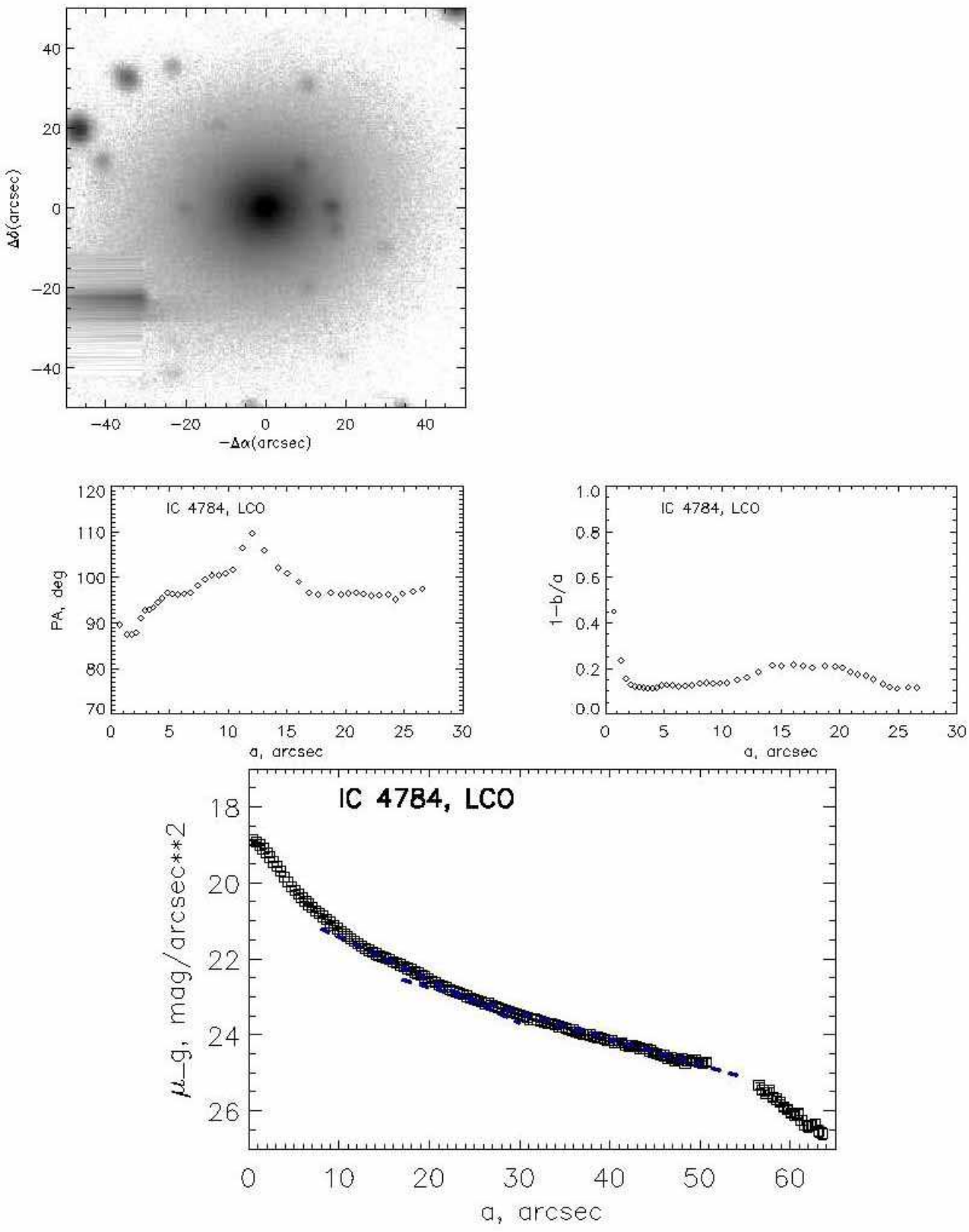
Δδ(arcsec)
−Δα(arcsec)
IC 4784, LCO
PA, deg
a, arcsec
IC 4784, LCO
1−b/a
a, arcsec
IC 4784, LCO
μ_g, mag/arcsec**2
a, arcsec

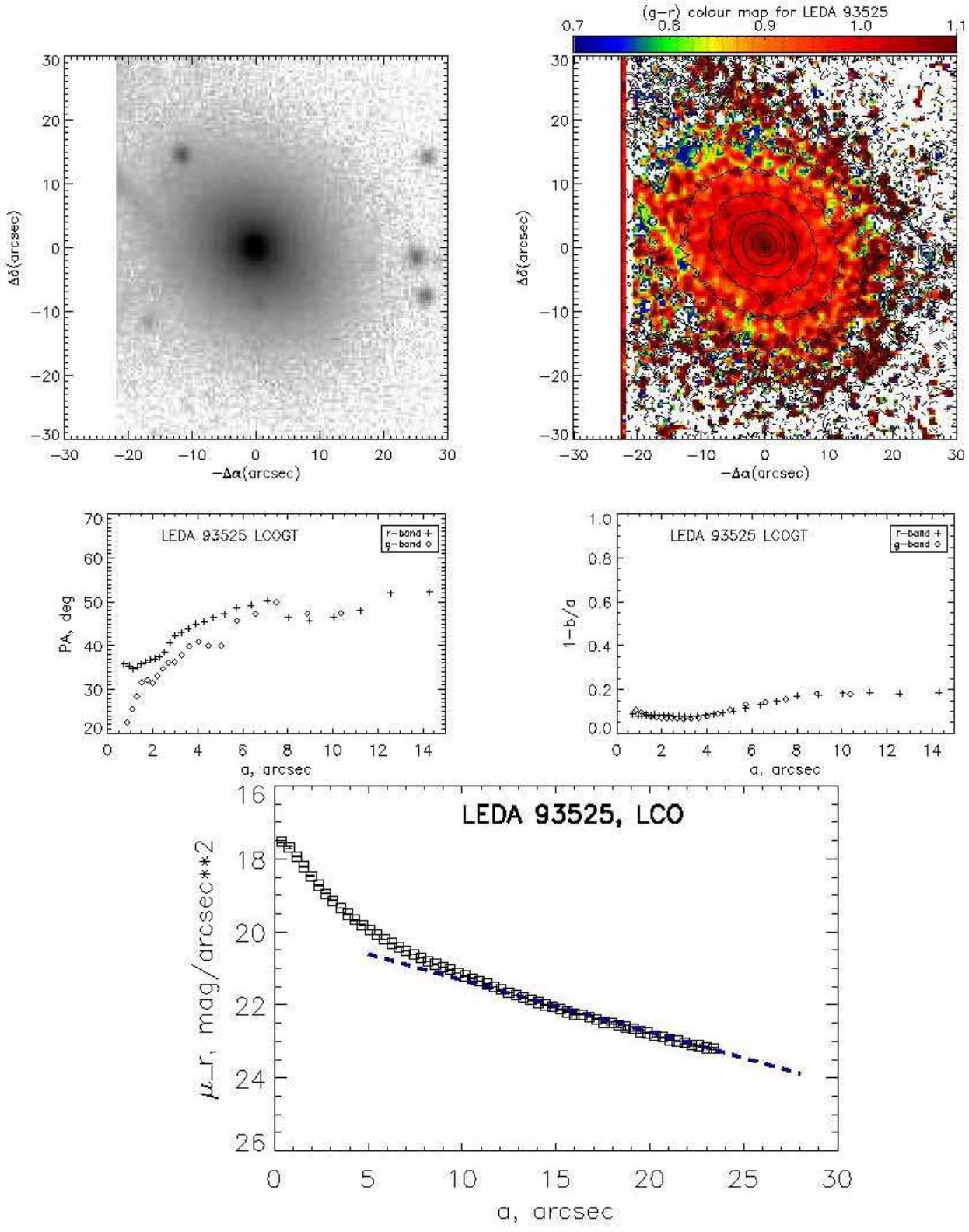
(g−r) colour map for LEDA 93525
0.7
0.8
0.9
1.0
1.1
Δδ(arcsec)
−Δα(arcsec)
LEDA 93525 LCOGT
r−band +
g−band ◇
PA, deg
a, arcsec
1−b/a
LEDA 93525, LCO
μ_r, mag/arcsec**2

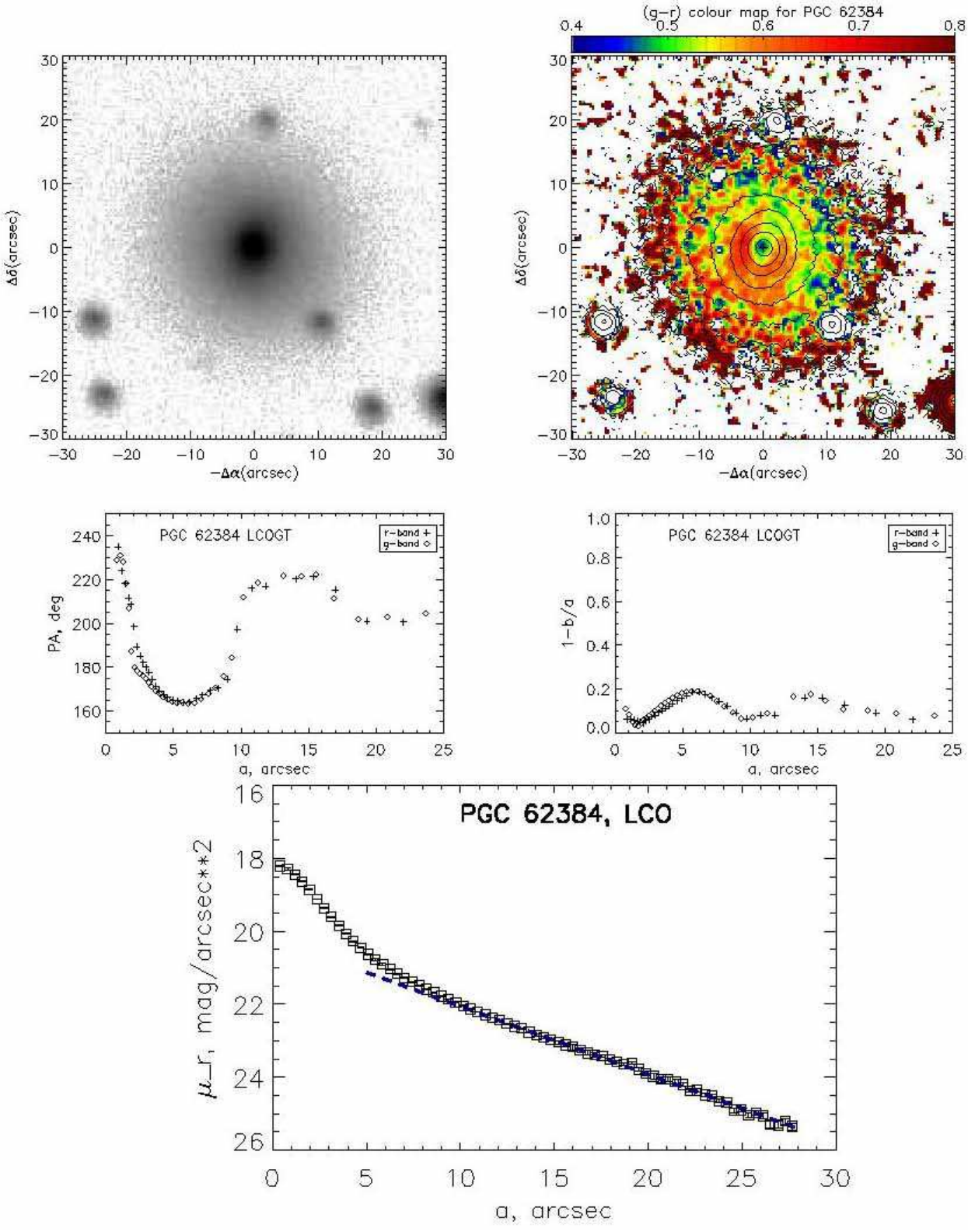
(g−r) colour map for PGC 62384
0.4
0.5
0.6
0.7
0.8
Δδ(arcsec)
−Δα(arcsec)
PGC 62384 LCOGT
r−band +
g−band ◇
PA, deg
1−b/a
a, arcsec
PGC 62384, LCO
μ_r, mag/arcsec**2

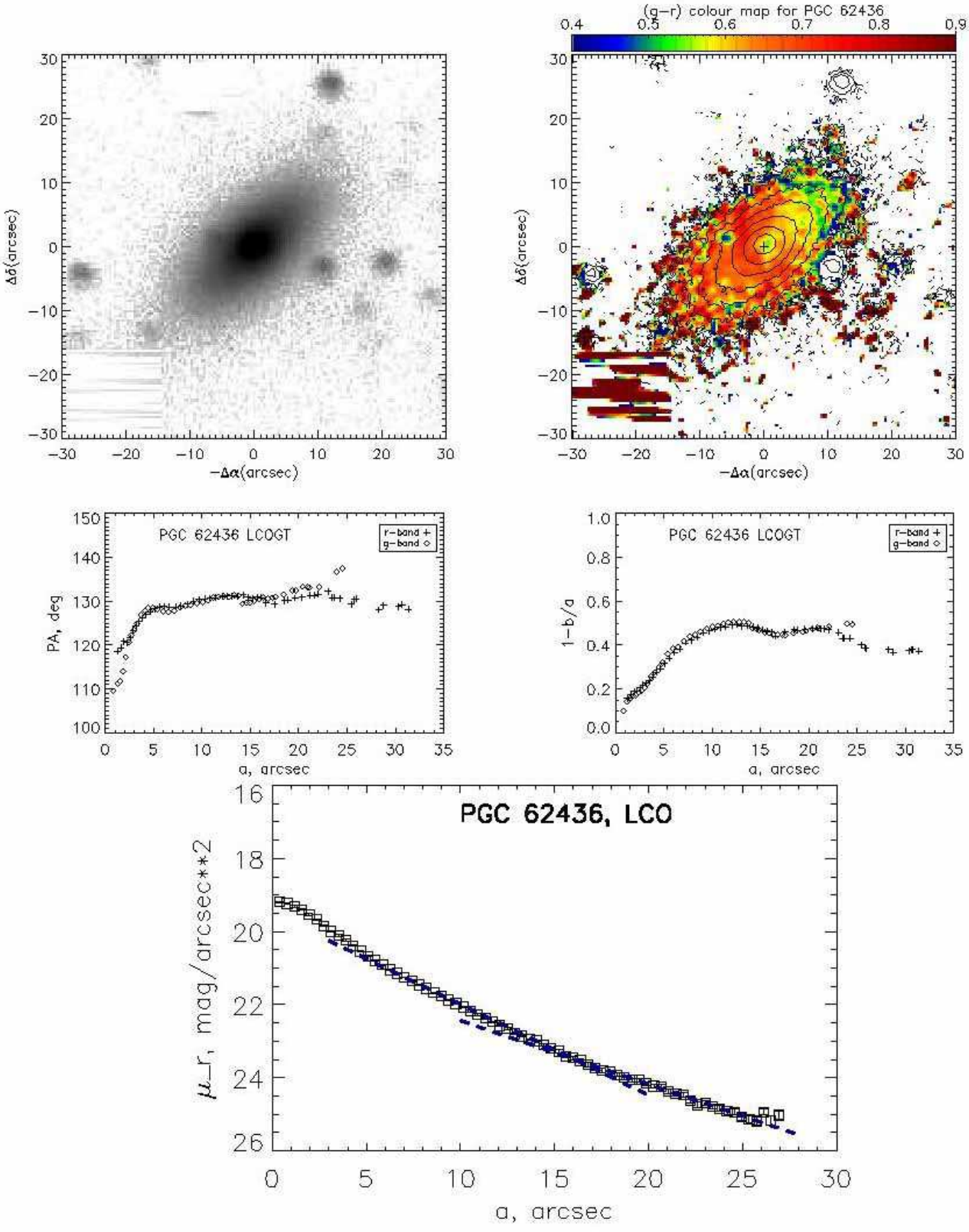
(g−r) colour map for PGC 62436
0.4 0.5 0.6 0.7 0.8 0.9
Δδ(arcsec)
−Δα(arcsec)
PGC 62436 LCOGT
r−band +
g−band ◇
PA, deg
a, arcsec
1−b/a
PGC 62436, LCO
μ_r, mag/arcsec**2

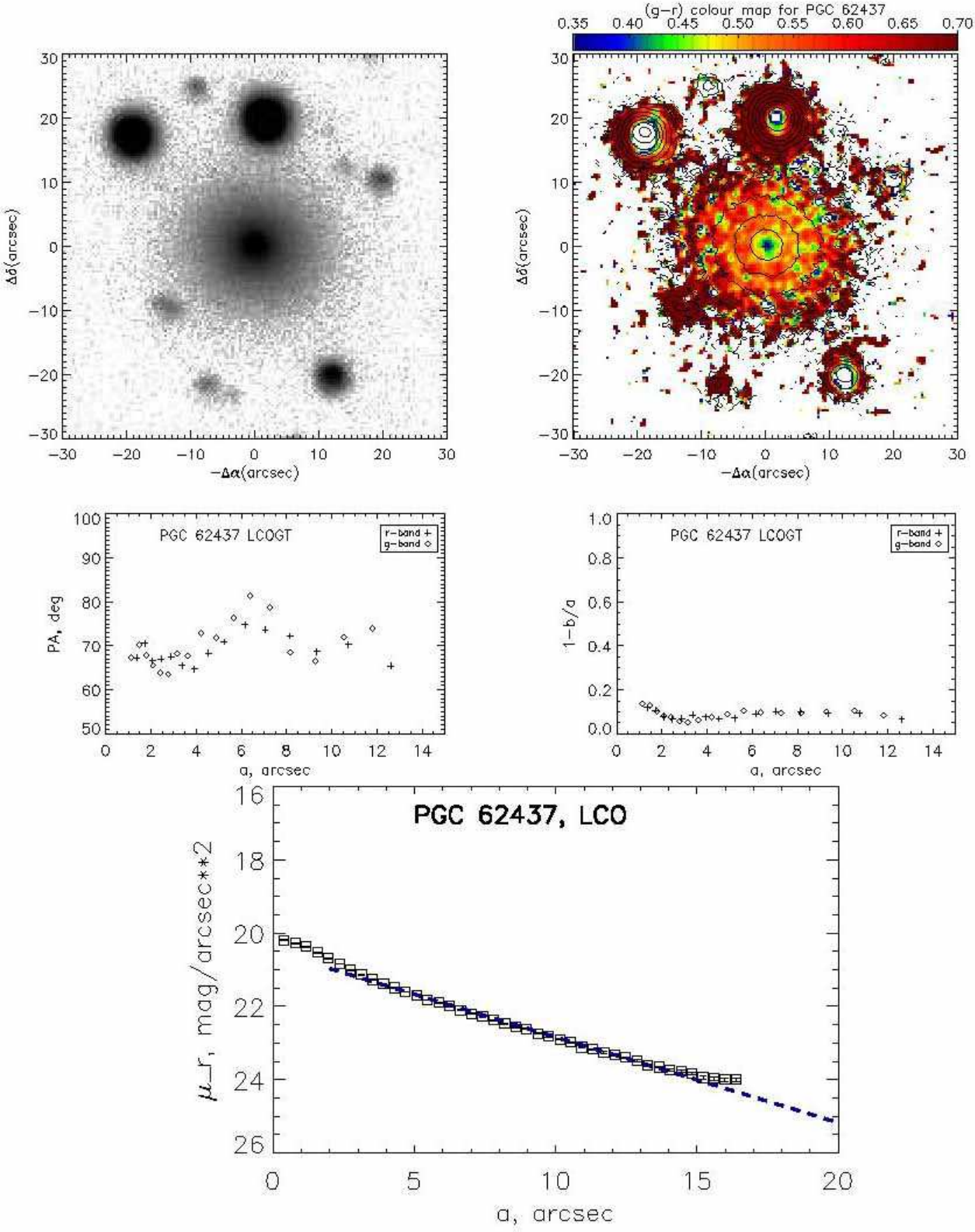
(g−r) colour map for PGC 62437
0.35 0.40 0.45 0.50 0.55 0.60 0.65 0.70
Δδ(arcsec)
−Δα(arcsec)
PGC 62437 LCOGT
r−band +
g−band ◇
PA, deg
a, arcsec
1−b/a
PGC 62437, LCO
μ_r, mag/arcsec**2